Electron and photon energy calibration with the ATLAS detector using 2015-2016 LHC proton-proton collision data

ATLAS Collaboration; Newman, Paul

DOI:
10.1088/1748-0221/14/03/P03017

Document Version
Publisher's PDF, also known as Version of record

Citation for published version (Harvard):
ATLAS Collaboration & Newman, P 2019, 'Electron and photon energy calibration with the ATLAS detector using 2015-2016 LHC proton-proton collision data', *Journal of Instrumentation*, vol. 14, no. 3, P03017. https://doi.org/10.1088/1748-0221/14/03/P03017

Journal of Instrumentation

Electron and photon energy calibration with the ATLAS detector using 2015–2016 LHC proton-proton collision data

Published by IOP Publishing for Sissa Medialab

Received: *December 11, 2018*
Accepted: *March 4, 2019*
Published: *March 18, 2019*

Electron and photon energy calibration with the ATLAS detector using 2015–2016 LHC proton-proton collision data

The ATLAS collaboration

E-mail: atlas.publications@cern.ch

Abstract: This paper presents the electron and photon energy calibration obtained with the ATLAS detector using about 36 fb^{-1} of LHC proton-proton collision data recorded at $\sqrt{s}$ = 13 TeV in 2015 and 2016. The different calibration steps applied to the data and the optimization of the reconstruction of electron and photon energies are discussed. The absolute energy scale is set using a large sample of Z boson decays into electron-positron pairs. The systematic uncertainty in the energy scale calibration varies between 0.03% to 0.2% in most of the detector acceptance for electrons with transverse momentum close to 45 GeV. For electrons with transverse momentum of 10 GeV the typical uncertainty is 0.3% to 0.8% and it varies between 0.25% and 1% for photons with transverse momentum around 60 GeV. Validations of the energy calibration with $J/\psi \to e^+e^-$ decays and radiative Z boson decays are also presented.

Keywords: Calorimeter methods; Pattern recognition, cluster finding, calibration and fitting methods; Performance of High Energy Physics Detectors

ArXiv ePrint: 1812.03848

https://doi.org/10.1088/1748-0221/14/03/P03017

Contents

2019 JINST 14 P03017

1 Introduction

A precise calibration of the energy measurement of electrons and photons is required for many analyses performed at the CERN Large Hadron Collider (LHC), among which the studies of the Higgs boson in the two-photon and four-lepton decay channels and precise studies of W and Z boson production and properties. This paper presents the calibration of the energy measurement of electrons and photons achieved with the ATLAS detector using 36 fb^{-1} of LHC proton−proton collision data collected in 2015 and 2016 at $\sqrt{s} = 13$ TeV.

The calibration scheme comprises a simulation-based optimization of the energy resolution for electrons and photons, corrections accounting for differences between data and simulation, the adjustment of the absolute energy scale using Z boson decays into e^+e^- pairs, and the validation of the energy scale universality using J/ψ decays decays into e^+e^- pairs and radiative Z boson decays. This strategy closely follows the procedure used for the final energy calibration applied to the data collected in 2011 and 2012 (Run 1) [1], with updates to reflect the changes in data-taking and detector conditions.

This paper is organized as follows. Section 2 briefly describes the ATLAS detector and the reconstruction of electron and photon candidates. Section 3 introduces the calibration procedure and the changes relative to the Run 1 calibration. Section 4 gives a list of the different data and simulated event samples used in these studies. Section 5 explains how the simulated event samples are used to optimize the estimate of electron and photon energies, as well as the expected resolutions of the energy measurements. Section 6 describes the different corrections applied to the data. Section 7 discusses the extraction of the overall energy scale and resolution corrections between data and simulation from $Z \to ee$ decays. Section 8 describes the different systematic uncertainties affecting the energy scale and resolution. Finally section 9 presents the cross-checks performed using independent data samples.

2 ATLAS detector, electron and photon reconstruction

2.1 The ATLAS detector

The ATLAS experiment [2] at the LHC is a multipurpose particle detector with a forward−backward symmetric cylindrical geometry and a near 4π coverage in solid angle.[1]

[1] ATLAS uses a right-handed coordinate system with its origin at the nominal interaction point (IP) in the centre of the detector and the z-axis along the beam pipe. The x-axis points from the IP to the centre of the LHC ring, and the

It consists of an inner tracking detector surrounded by a thin superconducting solenoid, electromagnetic and hadronic calorimeters, and a muon spectrometer incorporating three large superconducting toroidal magnets with eight coils each. The inner-detector system (ID) is immersed in a 2 T axial magnetic field and provides charged-particle tracking in the range $|\eta| < 2.5$.

The high-granularity silicon pixel detector covers the vertex region and typically provides four measurements per track. It is followed by the silicon microstrip tracker, which usually provides four two-dimensional measurement points per track. These silicon detectors are complemented by the transition radiation tracker, which enables radially extended track reconstruction up to $|\eta| = 2.0$. The transition radiation tracker also provides electron identification information based on the fraction of hits (typically 30 in total) above a higher energy-deposit threshold corresponding to transition radiation.

The electromagnetic (EM) calorimeter is a lead/liquid-argon (LAr) sampling calorimeter with an accordion geometry. It is divided into a barrel section (EMB), covering the pseudorapidity region $|\eta| < 1.475$ and two endcap sections (EMEC), covering $1.375 < |\eta| < 3.2$. For $|\eta| < 2.5$, the EM calorimeter is divided into three layers in depth. Each layer is segmented in η–ϕ projective readout cells. The first layer is finely segmented in the η direction for the regions $0 < |\eta| < 1.4$ and $1.5 < |\eta| < 2.4$ with a cell size in $\Delta\eta \times \Delta\phi$ varying from 0.003×0.1 in the barrel region to 0.006×0.1 in the region $|\eta| > 2.0$. The fine segmentation in the η direction provides event-by-event discrimination between single-photon or single-electron showers and overlapping showers produced in the decays of neutral hadrons. The first layer's thickness varies between 3 and 5 radiation lengths, depending on η. The second layer collects most of the energy deposited in the calorimeter by electron and photon showers. Its thickness is between 17 and 20 radiation lengths and the cell size is 0.025×0.025 in $\Delta\eta \times \Delta\phi$. A third layer with cell size of 0.050×0.025 and thickness of 2 to 10 radiation lengths is used to correct for the leakage beyond the EM calorimeter. A high-voltage system generates an electric field of about 1 kV/mm between the lead absorbers and copper electrodes located at the middle of the liquid-argon gaps. It induces ionization electrons to drift in the gap. In the region $|\eta| < 1.8$, a thin presampler layer, located in front of the accordion calorimeter, is used to correct for energy loss upstream of the calorimeter. It consists of an active liquid-argon layer with a thickness of 1.1 cm (0.5 cm) in the barrel (endcap) with a cell size of 0.025×0.1 in $\Delta\eta \times \Delta\phi$.

In the transition region between the EMB and the EMEC, $1.37 < |\eta| < 1.52$, a large amount of material is located in front of the first calorimeter layer, ranging from 5 to almost 10 radiation lengths. This section is instrumented with scintillators located between the barrel and endcap cryostats, and extending up to $|\eta| = 1.6$.

Hadronic calorimetry is provided by the steel/scintillator-tile calorimeter, divided into three barrel structures within $|\eta| < 1.7$ and two copper/LAr hadronic endcap calorimeters. The solid angle coverage is completed in the region $3.2 < |\eta| < 4.9$ with forward copper/LAr and tungsten/LAr calorimeter modules optimized for electromagnetic and hadronic measurements respectively.

The muon spectrometer comprises separate trigger and high-precision tracking chambers measuring the deflection of muons in a magnetic field generated by superconducting air-core toroid

y-axis points upward. Cylindrical coordinates (r, ϕ) are used in the transverse plane, ϕ being the azimuthal angle around the z-axis. The pseudorapidity is defined in terms of the polar angle θ as $\eta = -\ln\tan(\theta/2)$. The transverse energy is defined as $E_{\mathrm{T}} = E \sin\theta$.

2019 JINST 14 P03017

magnets. The field integral ranges between 2.0 and 6.0 T m across most of the detector. A set of precision chambers covers the region $|\eta| < 2.7$ with three layers of monitored drift tubes, complemented by cathode-strip chambers in the forward region, where the background is highest. The muon trigger system covers the range $|\eta| < 2.4$ with resistive-plate chambers in the barrel and thin-gap chambers in the endcap regions.

A two-level trigger system is used to select interesting events [3]. The first-level trigger is implemented in hardware and uses a subset of detector information to reduce the event rate to a design value of at most 100 kHz. This is followed by a software-based high-level trigger which reduces the event rate to about 1000 Hz.

2.2 EM calorimeter cell energy estimate

The deposit of energy in the liquid-argon gap induces an electric current proportional to the deposited energy. For a uniform energy deposit in the gap, the signal has a triangular shape as a function of time with a length corresponding to the maximum drift time of the ionization electrons, typically 450 ns. This signal is amplified and shaped by a bipolar filter in the front-end readout boards [4] to reduce the effect of out-of-time energy deposits from collisions in the following or previous bunch crossings. To accommodate the required dynamic range, three different gains (high, medium and low) are used. The shaped and amplified signals are sampled at 40 MHz and, for each first-level trigger, digitized by a 12-bit analogue-to-digital (ADC) converter. The medium gain for the sample corresponding to the maximum expected amplitude is digitized first to choose the most suited gain. Four time samples for the selected gain are then digitized and sent to the off-detector electronics via optical fibres. The position of the maximum of the signal is in the third sample for an energy deposit produced in the same bunch crossing as the triggered event.

From the digitized time samples (s_i), the total energy deposited in a calorimeter cell can be estimated as

$$E = F_{\mu\mathrm{A}\to\mathrm{MeV}} \times F_{\mathrm{ADC}\to\mu\mathrm{A}} \times \Sigma_{i=1}^{4} a_i (s_i - p). \tag{2.1}$$

- p is the readout electronics pedestal. It is measured for each gain in dedicated electronics calibration runs [4].

- a_i are optimal filtering coefficients [5] used to estimate the amplitude of the pulse. They are derived from the predicted pulse shape and the noise correlation functions between time samples so as to minimize the total noise arising from the electronics and the fluctuations of energy deposits from additional interactions in the same bunch crossing as the triggered event or in neighbouring crossings.

- $F_{\mathrm{ADC}\to\mu\mathrm{A}}$ is the conversion factor from ADC counts to input current. It is determined from dedicated electronics calibration runs and takes into account the difference in the response between the injected current from the pulser in calibration runs and the ionization current created by energy deposited in the gap [6].

- $F_{\mu\mathrm{A}\to\mathrm{MeV}}$ converts the ionization current to the total deposited energy in one cell. It is determined from test-beam studies [6].

2019 JINST 14 P03017

2.3 Electron and photon reconstruction and identification

The reconstruction of electrons and photons in the region $|\eta| < 2.47$ starts from clusters of energy deposits in the EM calorimeter [7]. Clusters matched to a reconstructed ID track, consistent with originating from an electron produced in the beam interaction region, are classified as electrons. Clusters without matching tracks are classified as unconverted photons. Converted photon candidates are defined as clusters matched to a track consistent with originating from a photon conversion in the material of the ID or matched to a two-track vertex consistent with the photon conversion hypothesis [8]. The definition of converted photon candidate includes requirements on the number of hits in the innermost pixel detector layer and on the fraction of high-threshold hits in the transition radiation tracker. The energy of the electron or photon is estimated using an area corresponding to 3×7 (5×5) second-layer cells in the barrel (endcap) region.

Photon identification is based primarily on shower shapes in the calorimeter. Two levels of selection, Loose and Tight, are defined [8]. The Tight identification efficiency ranges from 50% to 95% for photons of E_{T} between 10 and 100 GeV. To further reduce the background from jets, isolation selection criteria are used. They are based on topological clusters of energy deposits in the calorimeter [9] and on reconstructed tracks in a direction close to that of the photon candidate, as described in ref. [8].

Electrons are identified using a likelihood-based method combining information from the EM calorimeter and the ID. Different identification levels, Loose, Medium and Tight are defined [10], with typical efficiencies for electrons of E_{T} around 40 GeV of 92%, 85% and 75% respectively. Electrons are required to be isolated using both calorimeter-based and track-based isolation variables. More details are given in ref. [10].

3 Overview of the calibration procedure

The energy calibration discussed in this paper covers the region $|\eta| < 2.47$, which corresponds to the acceptance of the ID and the highly segmented EM calorimeter.

The different steps performed in the procedure to calibrate the energy response of electrons and photons from the energy of a cluster of cells in the EM calorimeter are the following:

- The estimation of the energy of the electron or photon from the energy deposits in the calorimeter: the properties of the shower development are used to optimize the energy resolution and to minimize the impact of material in front of the calorimeter. The multivariate regression algorithm used for this estimation is trained on samples of simulated events. The same algorithm is applied to data and simulation. This step relies on an accurate description of the material in front of the calorimeter in the simulation.

- The adjustment of the relative energy scales of the different layers of the EM calorimeter: this adjustment is based on studies of muon energy deposits and electron showers. It is applied as a correction to the data before the estimation of the energy of the electron or photon. This step is required for the correct extrapolation of the energy calibration to the full energy range of electrons and photons.

2019 JINST 14 P03017

- The correction for residual local non-uniformities in the calorimeter response affecting the data: this includes geometric effects at the boundaries between calorimeter modules and improvements of the corrections for non-nominal HV settings in some regions of the calorimeter. This is studied using the ratio of the measured calorimeter energy to the track momentum for electrons and positrons from Z boson decays.

- The adjustment of the overall energy scale in the data: this is done using a large sample of Z boson decays to electron-positron pairs. At the same time, a correction to account for the difference in energy resolution between data and simulation is derived, and applied to the simulation. These correction factors are assumed to be universal for electrons and photons.

- Checks of the results comparing data and simulation with independent samples: $J/\psi \to ee$ decays probe the energy response for low-energy electrons. Radiative Z boson decays are used to check the energy response for photons.

Compared with the Run 1 calibration [1], the main differences are:

- The data were collected with 25 ns spacing between the proton bunches instead of 50 ns. In addition the number of readout samples was reduced from five to four. This reduction was required in order to increase the maximum first-level trigger rate. The optimal filtering coefficients for the cell energy estimate (see section 2.2) were derived to minimize the total noise for a pile-up of 25 interactions per bunch crossing with 25 ns spacing between bunches, using four readout samples. For the Run 1 dataset, the noise minimization was performed for 20 interactions per bunch crossing with 50 ns spacing, using five readout samples. These changes can affect the energy scale of the different layers of the calorimeter.

- The data were collected with a higher number of pile-up interactions. This significantly impacts the measurements of muon-induced energy deposits in the calorimeter.

- The material in front of the calorimeter is mostly the same, with the exception of the addition of a new innermost pixel detector layer together with a thinner beam pipe and changes in the layout of the services of the pixel detector.

- In the data reconstruction, the calorimeter area used to collect the energy of unconverted photons was changed in order to be same size as for electrons and converted photons. This simplifies the estimate of the impact on the energy calibration of uncertainties in the conversion reconstruction efficiency. The corresponding increase of the cluster size for unconverted photons implies an increase in the noise which has a limited impact on the energy resolution: for E_{T} >20 (50) GeV, the energy resolution for unconverted photons is degraded by less than 10 (5)%.

4 Data and simulation samples

4.1 Data samples

The results presented in this article are based on proton−proton collision data at $\sqrt{s} = 13$ TeV, recorded in 2015 and 2016 with the ATLAS detector. During the period relevant to this paper,

2019 JINST 14 P03017

the LHC circulated 6.5 TeV proton beams with a 25 ns bunch spacing. The peak instantaneous luminosity was $1.37 \cdot 10^{34}$ cm^{-2}s^{-1}. Only data collected while all the detector components were operational are used. The integrated luminosity of this dataset is 36.1 fb^{-1}. The mean number of proton−proton interactions per bunch crossing is 23.5.

To select $Z \to ee$ events, a trigger requiring two electrons is used. For the 2015 (2016) dataset, the transverse energy (E_{T}) threshold applied at the first-level trigger is 10 (15) GeV. It is 12 (17) GeV at the high-level trigger, which uses an energy calibration scheme close to the one applied in the offline reconstruction. At the high-level trigger, the electrons are required to fulfil the Loose (Very Loose) likelihood-based identification criteria for 2015 (2016) data.

To select $J/\psi \to ee$ events, three dielectron triggers with different thresholds are used. At the first-level trigger, E_{T} thresholds of either 3, 7 or 12 GeV were applied for the candidate with highest E_{T}, and a 3 GeV threshold was applied on the second candidate. At least one electron was required to fulfil the Tight identification criteria at the high-level trigger with E_{T} larger than 5, 9 and 14 GeV depending on the trigger. The second electron was only required to have E_{T} above 4 GeV. The integrated luminosity collected with these prescaled triggers varies from 4 pb^{-1} to 640 pb^{-1} depending on the trigger threshold used. The total luminosity collected is 710 pb^{-1}.

To select $Z \to \mu\mu$ events, two main triggers are used. The first one requires two muons with transverse momentum (p_{T}) above 14 (10) GeV at the high-level (first-level) trigger. The second one requires one muon with p_{T} above 26 (20) GeV with isolation criteria applied at the high-level trigger.

For the samples of radiative Z boson decays ($ee\gamma$ and $\mu\mu\gamma$), the same triggers as for the $Z \to ee$ and $Z \to \mu\mu$ samples are used.

To select a sample of inclusive photons, a single-photon trigger is used, with an E_{T} threshold of 22 GeV at the first-level trigger and the Loose photon identification criteria with E_{T} larger than 140 GeV applied at the high-level trigger.

4.2 Simulation samples

Monte Carlo (MC) samples of $Z \to ee$ and $Z \to \mu\mu$ decays were simulated at next-to-leading order (NLO) in QCD using POWHEG-BOX v2 [11] interfaced to the PYTHIA8 [12] version 8.186 parton shower model. The CT10 [13] parton distribution function (PDF) set was used in the matrix element. The AZNLO set of tuned parameters [14] was used, with PDF set CTEQ6L1 [15], for the modelling of non-perturbative effects. The EvtGen 1.2.0 program [16] was used to model b- and c-hadron decays. Photos++ 3.52 [17] was used for QED emissions from electroweak vertices and charged leptons.

Samples of $Z \to ee\gamma$ and $Z \to \mu\mu\gamma$ events with transverse momentum of the photon above 10 GeV were generated with SHERPA version 2.1.1 [18] using QCD leading-order (LO) matrix elements with up to three additional partons in the final state. The CT10 PDF set was used in conjunction with the dedicated parton shower tuning developed by the SHERPA authors.

Both non-prompt (originating from b-hadron decays) and prompt (not originating from b-hadron decays) $J/\psi \to ee$ samples were generated using PYTHIA8. The A14 set of tuned parameters [19] was used together with the CTEQ6L1 PDF set. The EvtGen program was used to model the b- and c-hadron decays. Three different samples were produced with different selections on the transverse momenta of the electrons produced in the J/ψ decay.

2019 JINST 14 P03017

Samples of inclusive photon production were generated using PYTHIA8. The PYTHIA8 simulation of the signal includes LO photon-plus-jet events from the hard subprocesses $qg \to q\gamma$ and $qq \to g\gamma$ and photon bremsstrahlung in LO QCD dijet events (called the "bremsstrahlung component"). The bremsstrahlung component was modelled by final-state QED radiation arising from calculations of all $2 \to 2$ QCD processes. The A14 set of tuned parameters was used together with the NNPDF23LO PDF set [20].

Backgrounds affecting the $Z \to ee$ sample were generated with POWHEG-BOX v2 interfaced to PYTHIA8 for the $Z \to \tau\tau$ process, with SHERPA version 2.2.1 for the vector-boson pair-production processes and with SHERPA version 2.1.1 for top-quark pair production in the dilepton final state.

For the optimization of the MC-based response calibration, samples of 40 million single electrons and single photons were simulated. Their transverse momentum distribution covers the range from 1 GeV to 3 TeV.

The generated events were processed through the full ATLAS detector simulation [21] based on GEANT4 [22]. The MC events were simulated with additional interactions in the same or neighbouring bunch crossings to match the pile-up conditions during LHC operations and were weighted to reproduce the distribution of the average number of interactions per bunch crossing in data. The overlaid proton−proton collisions were generated with the soft QCD processes of PYTHIA8 version 8.186 using the A2 set of tuned parameters [23] and the MSTW2008LO PDF set [24].

The detector description used in the GEANT4 simulation was improved using data collected in Run 1 [1]. Compared with this improved description, the changes for the results presented in this paper are: the addition of the new innermost pixel layer and the new beam pipe in Run 2 [25–27], the modification of the pixel detector services at small radius [28] and a re-tuning in the simulation of the amount of material in the transition region between the barrel and endcap calorimeter cryostats to agree better with the measurement performed with Run 1 data. The amount of material in front of the presampler detector is about 1.8 radiation lengths at small values of $|\eta|$, reaching ≈ 4 radiation lengths at the end of the EMB acceptance and up to 6 radiation lengths close to $|\eta| = 1.7$. The amount of material located between the presampler and the first layer of the calorimeter is typically 0.5 to 1.5 radiation lengths except in the transition region between the EMB and EMEC, where it is larger. For $|\eta| > 1.8$, the total amount of material in front of the calorimeter is typically 3 radiation lengths. The simulation models the details of the readout electronics response following the same ingredients as described in eq. (2.1).

For studies of systematic uncertainties related to the detector description in the simulation, samples with additional passive material in front of the EM calorimeter were simulated. The samples vary by the location of the additional material: in the inner-detector volume, in the first pixel detector layer, in the services of the pixel detector at small radius, in the regions close to the calorimeter cryostats, between the presampler and the electromagnetic calorimeter or in the transition region between the barrel and endcap calorimeters.

4.3 Event selection

Table 1 lists the kinematic selections applied to the different samples and the number of events recorded in 2015 and 2016. The average electron transverse energy is around 40–50 GeV in the

2019 JINST 14 P03017

Table 1. Summary of the kinematic selections applied to the main samples used in the calibration studies and number of events fulfilling all the requirements described in the text in the 2015–2016 dataset, except for the $Z \to \ell\ell\gamma$ and inclusive photon samples, which use only data collected in 2016. The symbol ℓ denotes an electron or a muon.

Process	Selections	N(events)
$Z \to ee$	$E_{\mathrm{T}}^{e} > 27$ GeV, $\lvert\eta^{e}\rvert < 2.47$	17.3 M
	$m_{\mathrm{ee}} > 50$ GeV	
$Z \to \mu\mu$	$p_{\mathrm{T}}^{\mu} > 27$ GeV, $\lvert\eta^{\mu}\rvert < 2.5$	29.4 M
	$80 < m_{\mu\mu} < 105$ GeV	
$J/\psi \to ee$	$E_{\mathrm{T}}^{e} > 5$ GeV, $\lvert\eta^{e}\rvert < 2.4$, $2.1 < m_{ee} < 4.1$ GeV	60 k
$Z \to \ell\ell\gamma$	$E_{\mathrm{T}}^{e} > 18$ GeV, $\lvert\eta^{e}\rvert < 1.37$ or $1.52 < \lvert\eta^{e}\rvert < 2.47$,	27 k ($ee\gamma$)
	$p_{\mathrm{T}}^{\mu} > 15$ GeV, $\lvert\eta^{\mu}\rvert < 2.7$,	50 k ($\mu\mu\gamma$)
	$E_{\mathrm{T}}^{\gamma} > 15$ GeV, $\lvert\eta^{\gamma}\rvert < 1.37$ or $1.52 < \lvert\eta^{\gamma}\rvert < 2.37$	
	$\Delta R(\ell,\gamma) > 0.4$	
	$40 < m_{\ell\ell} < 80$ GeV	
Inclusive photons	$E_{\mathrm{T}}^{\gamma} > 147$ GeV, $\lvert\eta^{\gamma}\rvert < 1.37$ or $1.52 < \lvert\eta^{\gamma}\rvert < 2.37$	3.6 M

$Z \to ee$ sample and 10 GeV in the $J/\psi \to ee$ sample. For photons, the average transverse energy is about 25 GeV in the $Z \to ee\gamma$ and $Z \to \mu\mu\gamma$ samples.

To select $Z \to ee$ candidates, both electrons are required to satisfy the Medium selection of the likelihood discriminant and to fulfil the Loose isolation criteria, based on both ID- and calorimeter-related variables [10]. In the inclusive photon selection, the photons are required to fulfil the Tight identification selection and to be isolated, using the Tight criterion based only on calorimetric variables. To select muons in the $Z \to \mu\mu$ sample, the Medium muon identification working point [29] is used.

To select $J/\psi \to ee$ candidates, both electrons are required to fulfil the Tight identification and the Loose isolation criteria.

For the $Z \to ee\gamma$ sample ($Z \to \mu\mu\gamma$), the electrons (muons) are required to satisfy the Loose (Medium) identification level while the photon candidate is required to fulfil the Tight identification and the Loose isolation criteria [8]. The dilepton invariant mass is restricted to the range 40–80 GeV to enhance the sample in radiative Z decays. The photon candidate is required to be significantly separated from any charged-lepton candidate, $\Delta R(\ell,\gamma) > 0.4$, with $\Delta R = \sqrt{(\Delta\phi)^2 + (\Delta\eta)^2}$.

5 Electron and photon energy estimate and expected resolution from the simulation

5.1 Algorithm for estimating the energy of electrons and photons

The energy of electrons and photons is computed from the energy of the reconstructed cluster, applying a correction for the energy lost in the material upstream of the calorimeter, for the energy deposited in the cells neighbouring the cluster in η and ϕ, and the energy lost beyond the LAr calorimeter. A single correction for all of these effects is computed using multivariate regression

2019 JINST 14 P03017

algorithms tuned on samples of simulated single particles without pile-up, separately for electrons, converted photons and unconverted photons. The training of the algorithm, based on Boosted Decision Trees, is done in intervals of $|\eta|$ and of transverse energy. An updated version of the method described in ref. [1] is implemented. The set of input variables is refined and the procedure is extended to the whole EM calorimeter up to $|\eta| = 2.5$, including the transition region between the barrel and the endcap.

The variables considered in the regression algorithm are: the energy deposited in the calorimeter, the energy deposited in the presampler, the ratio of the energies deposited in the first and second layers (E_1/E_2) of the EM calorimeter, the η impact point of the shower in the calorimeter, and the distances in η and in ϕ between the impact point of the shower and the centre of the closest cell in the second calorimeter layer. The impact point of the shower is computed from the energy-weighted barycentre of the positions of the cells in the cluster. For converted photon candidates, the estimated radius of the photon conversion in the transverse plane as well as the properties of the tracks associated with the conversion are added. These variables are identical to those used in the Run 1 version except that E_1/E_2 is used instead of the longitudinal shower depth. The ratio E_1/E_2 is strongly correlated with the longitudinal shower depth but it has been studied in more detail, comparing data with simulations as described in section 6.1.

In the transition region between the barrel and endcap calorimeters, $1.4 < |\eta| < 1.6$, the amount of material traversed by the particles before reaching the first active layer of the calorimeter is large and the energy resolution is degraded. To mitigate this effect, information from the E_4 scintillators [2] installed in the transition region is used. The E_4 scintillators are part of the intermediate tile calorimeter (ITC). The ITC is located in the gap region, between the long barrel and the extended barrels of the tile calorimeter and it was designed to correct for the energy lost in the passive material that fills the gap region. Electrons and photons in the gap region deposit energy in the barrel and the endcap of the EM calorimeter, as well as in the E_4 scintillators. In this region, the energy deposited in the E_4 cells (each of size $\Delta\eta \times \Delta\phi = 0.1 \times 0.1$) and the difference between the cluster position and the centre of the E_4 cell are added to the set of input variables for the regression algorithm. Due to this additional information the energy resolution is improved as shown in figure 1 for simulated electrons generated with transverse energy between 50 GeV and 100 GeV. In this range, the improvement is largest for electrons (around 20%), while it is smaller for unconverted photons (5%). Such behaviour is expected, as the degradation of the energy resolution due to inactive material in front of the calorimeter is much higher for electrons.

5.2 Energy resolution in the simulation

The energy resolution after application of the regression algorithm in the MC samples is illustrated in figure 2, using simulated single-particle samples. The resolution is defined as the interquartile range of $E_{\text{calib}}/E_{\text{gen}}$, i.e. the interval excluding the first and last quartiles of the $E_{\text{calib}}/E_{\text{gen}}$ distribution in each bin, divided by 1.35, to convert to the equivalent standard deviation of a Gaussian distribution. The quantity E_{gen} is the true energy of the generated particle and E_{calib} is the reconstructed energy after applying the regression algorithm.

For unconverted photons, the energy resolution in these MC samples, which do not have any simulated pile-up, closely follows the expected sampling term of the calorimeter ($\approx 10\%/\sqrt{E/\text{GeV}}$ in the barrel and $\approx 15\%/\sqrt{E/\text{GeV}}$ in the endcap). For electrons and converted photons, the degraded

2019 JINST 14 P03017

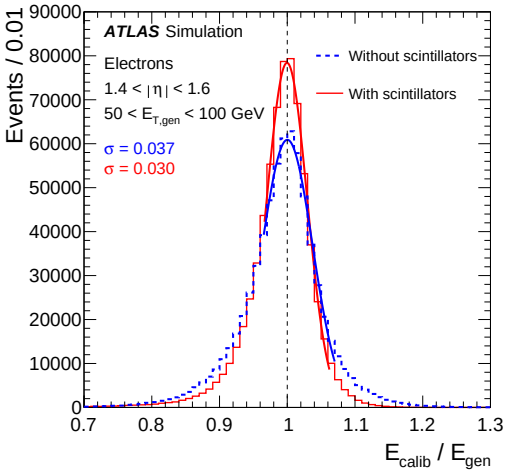

Figure 1. Distributions of the calibrated energy, E_{calib}, divided by the generated energy, E_{gen}, for electrons with $1.4 < |\eta| < 1.6$ and $50 < E_{\text{T,gen}} < 100$ GeV. The dashed (solid) histogram shows the results based on the energy calibration without (with) the scintillator information. The curves represent Gaussian fits to the cores of the distributions.

energy resolution at low energies reflects the presence of significant tails induced by interactions with the material upstream of the calorimeter. This degradation is largest in the regions with the largest amount of material upstream of the calorimeter, i.e. for $1.2 < |\eta| < 1.8$.

6 Corrections applied to data

In this section, the corrections applied to the data to account for residual differences between data and simulation are discussed. They include the intercalibration of the different calorimeter layers, corrections for energy shifts induced by pile-up and corrections to improve the uniformity of the energy response. Since the absolute energy scale is set with $Z \rightarrow ee$ decays, only the relative calibration of the energy scales of the first two layers and the presampler is needed. Given the small fraction of the energy deposited in the third layer of the calorimeter, no dedicated corrections for its intercalibration are applied.

6.1 Intercalibration of the first and second calorimeter layers

Muon energy deposits, which are insensitive to the amount of passive material in front of the EM calorimeter, are used to study the relative calibration of the first and second calorimeter layers. This relative calibration is derived by comparing the energy deposits in data with simulation predictions. The deposited muon energy, expressed on the same cell-level energy scale as described by eq. (2.1), is about 30 to 60 MeV depending on η in the first layer and 240 to 300 MeV in the second layer. The signal-to-noise ratio varies from about 2 to 0.5 (4 to 3) as a function of $|\eta|$ for the first (second) layer. A significant contribution to the noise, especially in the first layer of the endcap calorimeter, is due to fluctuations in the pile-up energy deposit.

The analysis uses muons from $Z \rightarrow \mu\mu$ decays, requiring $p_{\text{T}}^{\mu} > 27$ GeV. The calorimeter cells crossed by the muon tracks are determined by extrapolating the track to each layer of the calorimeter,

2019 JINST 14 P03017

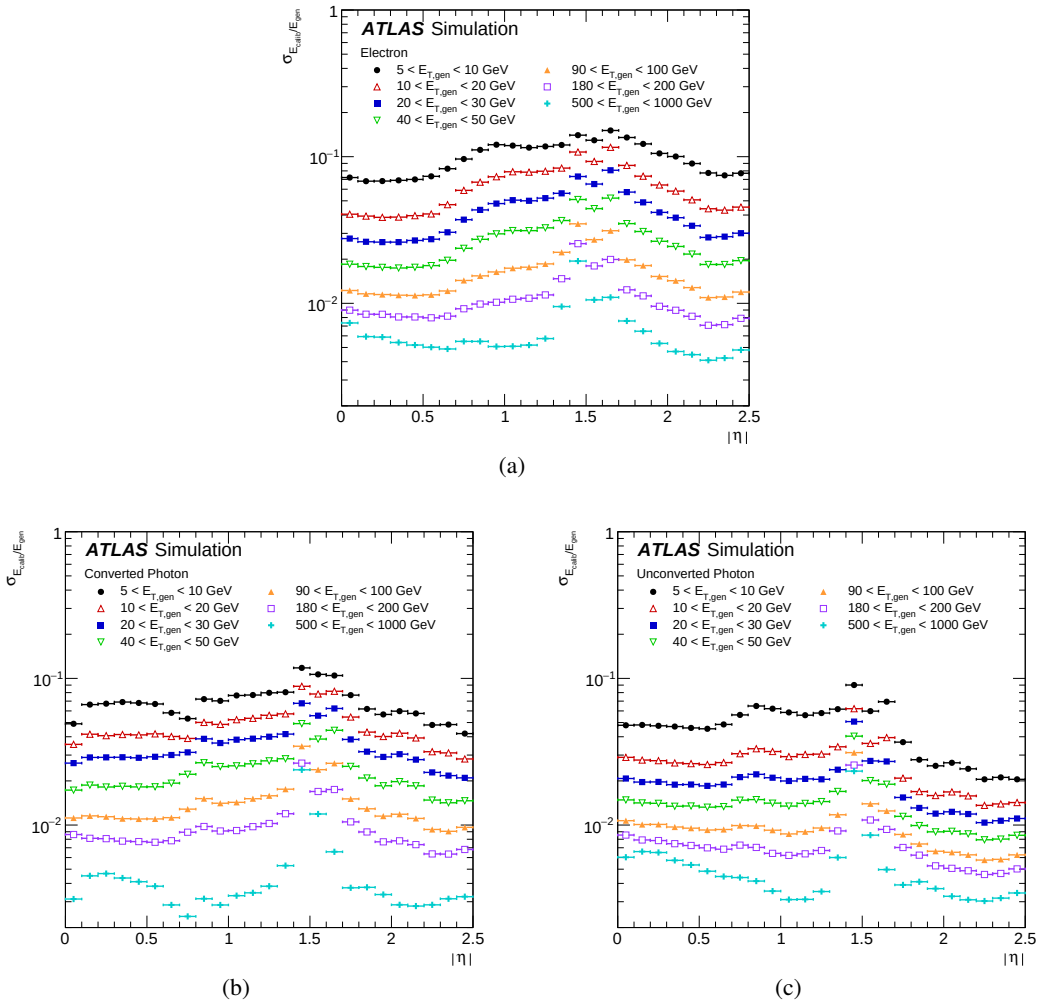

Figure 2. Energy resolution, $\sigma_{E_{\text{calib}}/E_{\text{gen}}}$, estimated from the interquartile range of $E_{\text{calib}}/E_{\text{gen}}$ as a function of $|\eta|$ for (a) electrons, (b) converted photons and (c) unconverted photons, for different E_{T} ranges.

taking into account the geometry of the calorimeter, the misalignment between the inner detector and the calorimeter (up to a few millimetres) and the magnetic field encountered by the muon along its path.

In the first layer, where the cell size in the η direction is small, the muon signal is estimated by summing the energies measured in three adjacent cells along η centred around the cell crossed by the extrapolated muon trajectory. Using three cells instead of only one gives a measurement that is less sensitive to the detailed modelling of the cross-talk between neighbouring cells and to the exact geometry of the calorimeter. In the second layer, due to the accordion geometry, the energy is most often shared between two adjacent cells along ϕ and the signal is estimated from the sum of the energies in the cell crossed by the extrapolated muon trajectory and in the neighbouring cell in ϕ with higher energy.

The observed muon energy distribution in each layer can be described by the convolution of a Landau distribution, representing the energy deposit, and a noise distribution. The most probable

2019 JINST 14 P03017

value (MPV) of the deposited muon energy is extracted using a fit of the convolution function to the observed muon energy distribution ("fit method"). Alternatively, the deposited energy can be estimated using a truncated-mean approach, where the mean is computed over a restricted window to minimize the sensitivity to the tails of the distribution ("truncated-mean method"). The same procedure is applied to data and MC samples and the relative calibration of the two layers is computed as $\alpha_{1/2} = (\langle E_1 \rangle^{\text{data}} / \langle E_1 \rangle^{\text{MC}}) / (\langle E_2 \rangle^{\text{data}} / \langle E_2 \rangle^{\text{MC}})$ with $\langle E_1 \rangle$ ($\langle E_2 \rangle$) denoting the MPV in the first (second) layer. The relative calibration of the two layers is computed as a function of $|\eta|$, since within the uncertainties all measured values are consistent between positive and negative η values.

In the fit method, the noise distribution is determined from data and MC samples separately to avoid a dependency on a possible pile-up noise mismodelling in the simulation. Events triggered on random LHC proton bunch crossings, with a trigger rate proportional to the instantaneous luminosity ("zero-bias events"), are used to estimate the noise distribution in data. The noise distribution is determined in intervals of $|\eta|$ and of $\langle \mu \rangle$, where $\langle \mu \rangle$ is the average number of pile-up interactions per bunch crossing. Figure 3 shows examples of the muon energy deposits in data and MC samples. It also shows the Landau distribution, the noise distribution and their convolution.

In the truncated-mean method, different choices for the window are investigated: ranges of ±2 and ±1.5 times the RMS of the distribution around the initial mean computed in a wide range, or the smallest range containing 90% of the energy distribution. The average of the results obtained with these choices is used as the estimate of $\alpha_{1/2}$.

To further reduce residual pile-up dependencies of the extracted MPV values, for both the fit and truncated-mean methods the analysis is performed as a function of the average number of interactions per bunch crossing. The result is extrapolated to a zero pile-up value to measure the intrinsic energy scale of each calorimeter layer for a pure signal. This extrapolation is performed using a first-order polynomial fit, which is found to describe data and MC results well. The fit is performed in the range from 12 to 30 interactions per bunch crossing to avoid low-statistics bins with a large range of the number of interactions per bunch crossing. The method is validated by comparing the MC extrapolated results with the ones obtained in a MC sample without any pile-up. The final result is given by the average of the two signal extraction methods, fit and truncated mean.

Figure 4 shows examples of the fitted MPV of the deposited muon energy as a function of the number of interactions per bunch crossing. The accurate noise modelling, performed separately for data and simulation, allows the extraction of the MPV of the muon energy deposit with only a small dependence with pile-up. The small slope of the fitted line limits the impact of the extrapolation from the average amount of pile-up in data to the zero pile-up point to the percent level.

The following effects are investigated to estimate the uncertainty in the $\alpha_{1/2}$ value measured with muons from the average of the results of the fit and truncated mean methods:

- Accuracy of the method to measure the genuine muon energy loss at zero pile-up: the uncertainty is taken from the difference between the result from the pile-up extrapolation in the MC sample with pile-up and the value observed in a MC sample without pile-up. It is typically 0.2% to 0.5% depending on $|\eta|$, up to 1.5% in some $|\eta|$ intervals in the endcap.

- Modelling of the energy loss outside the cells used for the measurement: only three (two) cells are used in the first (second) layer to minimize the noise. For muon trajectories close to

2019 JINST 14 P03017

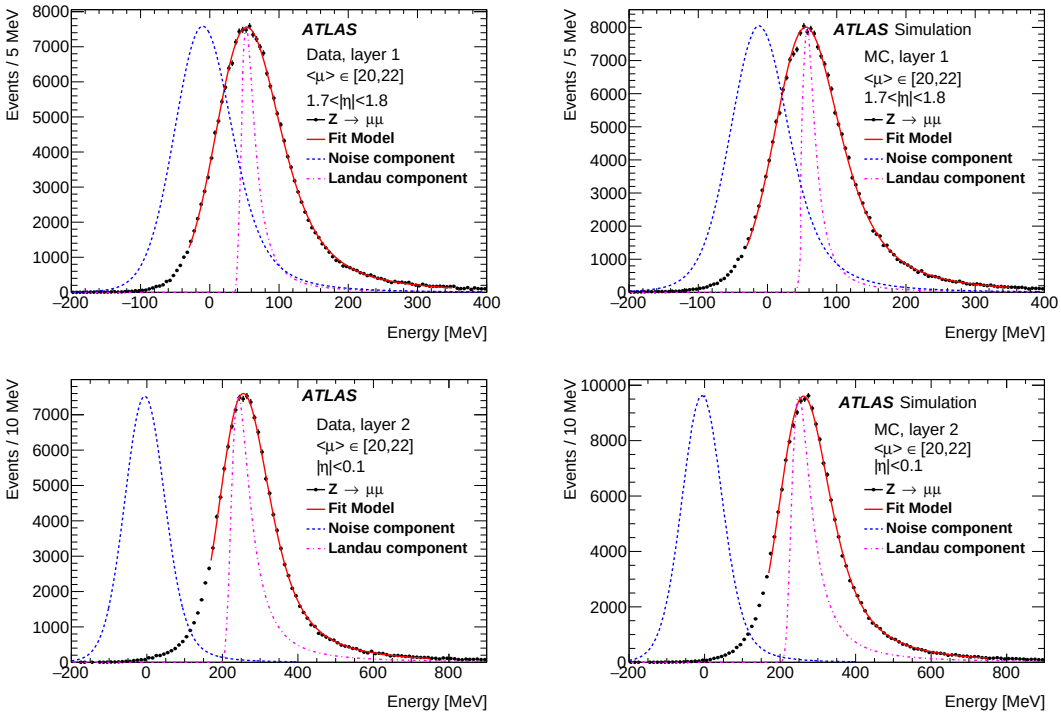

Figure 3. Muon energy distributions for two $|\eta|$ regions in data and simulation for the first and second calorimeter layers. The fit of the muon data to the convolution of the noise distribution and a Landau function is shown together with the individual components: the noise distribution and the Landau function. The distributions are shown for an average number of interactions per bunch crossing, $\langle\mu\rangle$, in the range from 20 to 22.

the boundaries in ϕ (η) between the first (second) layer cells a significant fraction of the muon energy deposit can be outside the used cells. To assess the uncertainty from the modelling of these effects in the simulation, the analysis is repeated using only muons crossing the centre of the first (second) layer within 0.04 (0.008) in the ϕ (η) direction and the change induced by these requirements is taken as the uncertainty. The uncertainty varies from 0.5% to 1%.

- Choice of the cell in ϕ for the second layer: the analysis is repeated using as the second cell in layer two the neighbour closer to the extrapolated muon trajectory instead of the neighbour with the higher energy. The difference between the results of these two choices, typically 0.2%, is taken as the uncertainty.

- For the truncated-mean method, the results obtained with the different ranges for the truncated-mean computation are compared. The maximum deviation of these results from their average is taken as the uncertainty. The change in the result when varying the upper energy limit used to compute the initial mean is also taken into account in the uncertainty. The resulting uncertainty is 0.5%.

- Half of the difference between the fit and truncated-mean methods is taken as an uncertainty in the result. This leads to an uncertainty varying from 0.5% to 1% depending on $|\eta|$.

2019 JINST 14 P03017

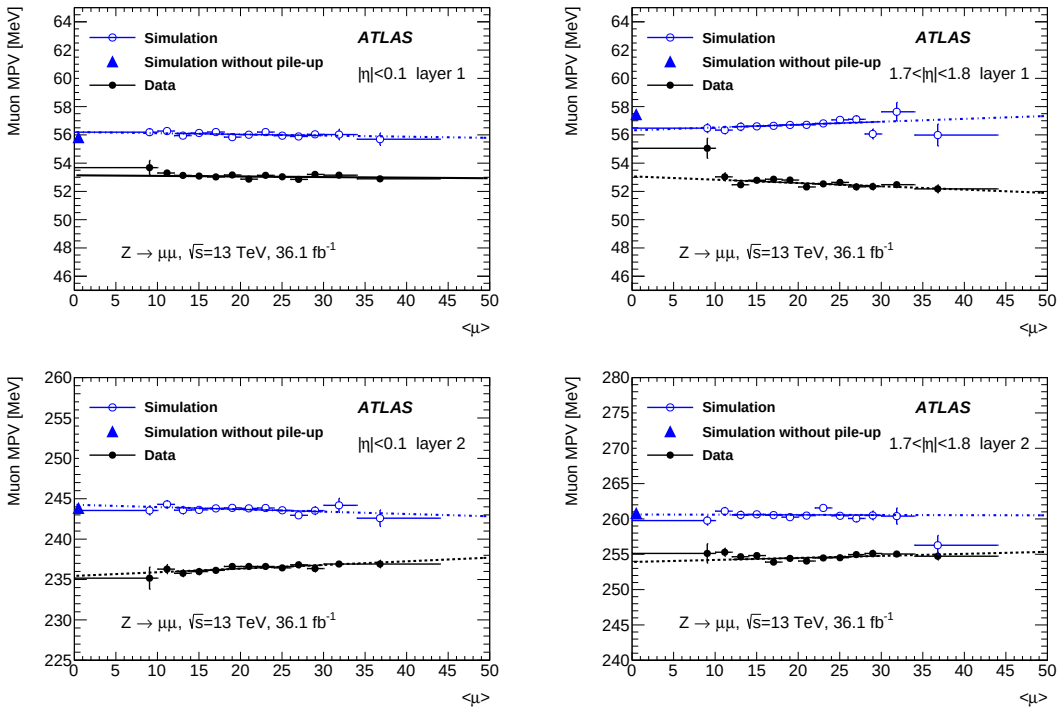

Figure 4. Distribution of the fitted MPV of the muon energy deposit in two $|\eta|$ intervals, for the first and second calorimeter layers, as a function of the average number of pile-up interactions per bunch crossing $\langle\mu\rangle$. The values obtained in data and MC samples are shown. The linear fits which are used to extrapolate the MPV value to zero pile-up are displayed. The solid part of the lines show the range used in the fit while the dashed part of the lines show the extrapolation of the linear fit. The MPV extracted from a MC sample without pile-up is also shown.

Figure 5 shows the results for $\alpha_{1/2}$ and the comparison of the two methods. The average result is shown with its total uncertainty defined as the sum in quadrature of the statistical uncertainty and all the systematic uncertainties described above. The total systematic uncertainty is estimated to be correlated within $|\eta|$ regions corresponding to the intervals 0–0.6, 0.6–1.4, 1.4–1.5, 1.5–2.4 and 2.4–2.5, and uncorrelated between two different intervals. In the last $|\eta|$ range, no measurement with muons is performed, and a large uncertainty of ±20% in the layer calibration is assigned, derived from a comparison between data and simulation of the ratio E_1/E_2 of electron showers. Despite the high level of pile-up in the data, the accuracy of the measurement with muons is typically 0.7% to 1.5% (1.5% to 2.5%) depending on η in the barrel (endcap) calorimeter, for $|\eta| < 2.4$, except in the transition region between the barrel and endcap calorimeters.

The features as a function of $|\eta|$ observed for $\alpha_{1/2}$ are similar to the ones observed in the Run 1 calibration performed with muons [1]. A change in the relative energy scales of the two layers, at a level of less than 1.5%, can be expected from the re-optimization of the pulse reconstruction performed for Run 2 data to minimize the expected pile-up noise. Within their respective uncertainties, the Run 1 result and this result are in agreement with this expectation.

In addition to the systematic uncertainties specific to the measurement of energy deposits from muons in the calorimeter layers, the interpretation of this measurement as an estimate of the relative

2019 JINST 14 P03017

energy scale of the two layers relies on a proper modelling in the simulation of the ionization current induced by muons. This is subject to the following sources of uncertainty: uncertainty in the exact path length traversed by the muons, related to the uncertainty in the geometry of the readout cells; uncertainty in the effect of reduced electric field at the transition between the different calorimeter layers; uncertainty in the modelling of the conversion of deposited energy to ionization current due to variations in the electric field following the accordion structure of the calorimeter, and uncertainty in the cross-talk between different calorimeter cells. These sources of uncertainty affect muon energy deposits and electron/photon showers differently. The values of these uncertainties are exactly the same as estimated in ref. [1]. They induce an uncertainty varying from 1% to 1.5% depending on $|\eta|$ in the relative calibration of the first and second calorimeter layers. Uncertainties related to possible non-linearities of the energy response for the different calorimeter layers are discussed in section 8.5.

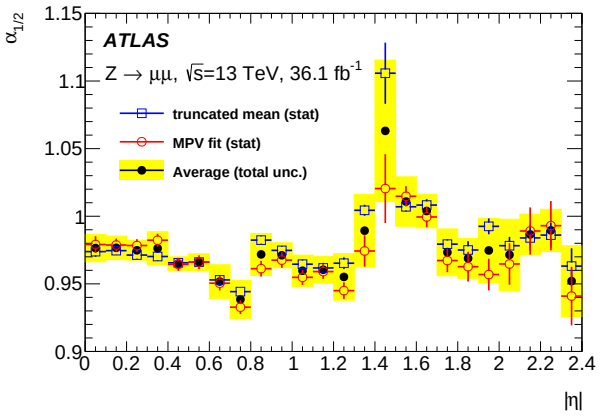

Figure 5. Ratio $\alpha_{1/2} = (\langle E_1 \rangle^{\text{data}} / \langle E_1 \rangle^{\text{MC}}) / (\langle E_2 \rangle^{\text{data}} / \langle E_2 \rangle^{\text{MC}})$ as a function of $|\eta|$, as obtained from the study of the muon energy deposits in the first two layers of the calorimeters. The results from the two methods are shown with their statistical uncertainties. The final average measurement is shown with its total uncertainty including the statistical and systematic uncertainties.

The relative calibration of the first two layers of the calorimeter can also be probed using $Z \to ee$ decays by investigating the variation of the mean of the dielectron invariant mass as a function of the ratio of the energies of the electron or positron candidates in the first two layers. Good agreement with the results obtained with muons is observed except in the $|\eta|$ range 1.2 to 1.8. In this region, the results of the method based on $Z \to ee$ are very sensitive to the interval used to compute the average invariant mass. Better agreement with the muon-based results is seen when a narrow mass range around the Z boson mass is used. This points to differences between data and simulation in the modelling of the tails of the electron energy resolution. The impact of the mass range variation on the energy calibration is studied in section 7. Similar results are found if the ratio of the track momentum measured in the ID to the energy measured in the calorimeter is used instead of the invariant mass to probe the energy calibration.

2019 JINST 14 P03017

6.2 Presampler energy scale

The presampler energy scale α_{PS} is determined from the ratio of the presampler energies in data and simulation. The measured energy in the presampler for electrons from Z boson decays is sensitive to both α_{PS} and the amount of material in front of the presampler. In order to be sensitive only to α_{PS}, the procedure to measure α_{PS} [1] exploits the correlation between the shower development and the amount of material in front of the presampler; more precisely, several simulations with additional passive material upstream of the presampler are considered, and correlation factors between the presampler energy deposit (E_0) and the ratio of the energies deposited in the first two layers ($E_{1/2}$) are extracted. The relative calibration of the first two layers, which is described in section 6.1, is applied. To minimize the impact on $E_{1/2}$ of any mismodelling of the material between the presampler and the calorimeter, an additional correction is applied. This last correction is extracted from a sample of unconverted photons with small energy deposit in the presampler to be insensitive to the material in front of the calorimeter. The presampler energy scale is extracted as

$$\alpha_{\mathrm{PS}} = \frac{E_0^{\mathrm{data}}(\eta)}{E_0^{\mathrm{MC}}(\eta)} \times \frac{1}{1 + A(\eta)\left(\frac{E_{1/2}^{\mathrm{data}}(\eta)}{E_{1/2}^{\mathrm{MC}}(\eta) b_{1/2}(\eta)} - 1\right)}.$$

- $E_0^{\mathrm{data}}(\eta)$ and $E_0^{\mathrm{MC}}(\eta)$ are the average energies deposited in the presampler by the electrons from Z decays in data and simulation.
- $b_{1/2}(\eta)$ is the ratio of $E_{1/2}$ in data and simulation for unconverted photons with small energy deposit in the presampler. It is estimated using photons from radiative Z boson decays at low E_{T} and inclusive photons at high E_{T}. The average value of these two samples is used.
- $E_{1/2}^{\mathrm{data}}(\eta)$ and $E_{1/2}^{\mathrm{MC}}(\eta)$ are the average values of the ratio of the energy deposited in the first layer to the energy deposited in the second layer for electrons from Z decays in data and simulation, respectively. After the correction with $b_{1/2}(\eta)$, this ratio is directly proportional to the amount of material in front of the presampler.
- $A(\eta)$ represents the correlation between the changes in $E_{1/2}$ and E_0 when varying the material in front of the presampler. This correlation is estimated using simulations with different amounts of material (quantity and location in radius) added in front of the presampler. It varies between 2.5 and 1.5 for different values of $|\eta|$.

This procedure is validated using the simulation.

The measurement is performed in intervals of size 0.05 in $|\eta|$, excluding the transition region between the barrel and endcap calorimeters ($1.37 < |\eta| < 1.52$). Within a presampler module of $\Delta\eta$-size 0.2 in the barrel or 0.3 in the endcap, no significant energy scale difference is expected, so the measurements are averaged in $|\eta|$ over each module.

Uncertainties in the measurements of α_{PS} include the statistical uncertainties of the various input quantities in the data and simulation. The residual variations of the measured presampler scale within a presampler module is also taken as an uncertainty, uncorrelated between the different modules. In the last module of the barrel, the $b_{1/2}$ correction exhibits a significant deviation from unity for $|\eta| > 1.3$. The reason of this deviation is not understood. For this last module, an

2019 JINST 14 P03017

uncertainty is obtained by comparing the $b_{1/2}$ correction averaged in the neighbouring lower $|\eta|$ interval with the value observed in this module. Finally, the choice of E_0 interval used in the computation of $b_{1/2}$ is studied. From simulation studies, an upper bound in the range from 0.5 to 1.2 GeV reduces the impact of uncertainties in the material in front of the presampler on $b_{1/2}$. A variation of the result in the data, not expected from simulation, is observed when the upper bound is changed from 0.5 to 1.2 GeV. It is taken as a systematic uncertainty, fully correlated across the whole barrel presampler.

Figure 6 shows the result for α_{PS} as a function of $|\eta|$. The uncertainty in α_{PS} varies between 3% and 1.5% depending on $|\eta|$.

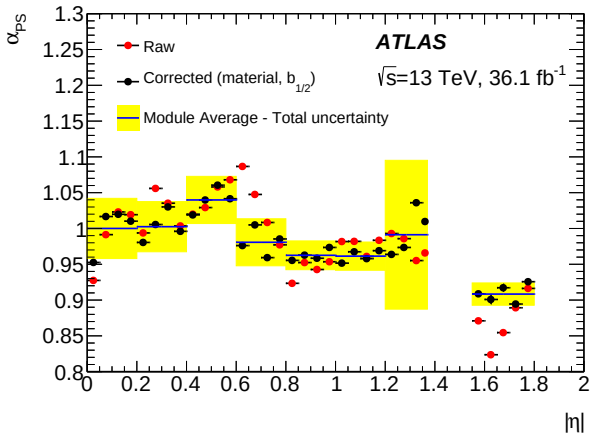

Figure 6. Measurement of the presampler energy scale ratio between data and simulation. The red points show the measurement before the material and $b_{1/2}(\eta)$ corrections. The black points show the measurements after these corrections are applied. The values averaged per presampler module in $|\eta|$ are shown together with the total uncertainties, represented by the shaded areas.

6.3 Pile-up energy shifts

After bipolar shaping, the average energy induced by pile-up interactions should be zero in the ideal situation of bunch trains with an infinite number of bunches and with the same luminosity in each pair of colliding bunches. In practice, bunch-to-bunch luminosity variations and the finite bunch-train length can create significant energy shifts which depend on the position inside the bunch train and on the luminosity. For most of the 2016 data, the bunch trains were made of 2 sub-trains of 48 bunches, with a bunch spacing of 25 ns between the bunches and of 225 ns between the two sub-trains. To mitigate this effect on the estimation of the cell energies, the average expected pile-up energy shift is subtracted cell-by-cell. The average is computed as a function of the bunch position inside the full LHC ring, taking into account the instantaneous luminosity per bunch, the expected pulse shape as a function of the time, the optimal filtering coefficients used to estimate the amplitude of the signal and a normalization factor derived from data with single colliding bunches.

Summing the cell-level contributions over an area equal to the size of an electron or photon cluster, the correction can reach 500 MeV of transverse energy, about 75 ns after the beginning of a bunch train for an average of 20 interactions per bunch crossing. After the correction, residual

2019 JINST 14 P03017

effects up to around 30 MeV are observed in zero-bias events. They arise mostly from inaccuracies in the predicted pulse shape. For instance in the presampler layer, the predicted pulse shape assumes a drift time corresponding to a high-voltage value of 2000 V while in the 2016 data a significantly lower high voltage of 1200 V was applied to reduce sporadic noise in the presampler.

To further reduce the impact of pile-up-induced energy shifts for electromagnetic clusters, an additional correction is applied separately for each calorimeter layer as a function of the average number of interactions per bunch crossing and as a function of η. The parameters of this cluster-level correction are derived from random clusters in zero-bias data.

After this second correction, the residual energy shift from pile-up is less than 10 MeV in transverse energy for the data collected in 2015 and 2016.

6.4 Improvements in the uniformity of the energy response

After all corrections described above are applied to the electron or photon candidates in data separately for each calorimeter layer, the energy is computed using the regression algorithm described in section 5. Corrections for variations in the energy response as a function of the impact point of the shower in the calorimeter affecting only the data are derived and applied to the energy of the electron or photon. Two effects are considered and corrected:

- Energy loss between the barrel calorimeter modules: the barrel calorimeter is made of 16 modules of size 0.4 each in $\Delta\phi$. The gap between absorbers increases slightly at the boundaries between modules, which leads to a reduced energy response. This effect varies as a function of ϕ since gravity causes the gaps to be smaller at the bottom of the calorimeter and larger at the top. A correction of this variation is parameterized using the ratio E/p of the calorimeter energy to the track momentum as a function of ϕ. This correction is $\lessapprox 2\%$. It is very similar to the effect observed with the Run 1 data [1].

- Effect of high-voltage inhomogeneities: in a small number of sectors (of size 0.2×0.2 in $\Delta\eta \times \Delta\phi$) of the calorimeter, the applied high voltage is set to a non-nominal value due to short circuits occurring in specific LAr gaps. The value of the high voltage is used to derive a correction applied in the cell-level calibration. Residual effects can arise for cases where large currents are drawn. In these cases, the correction is not computed accurately. The η–ϕ profiles of E/p in 2015 and 2016 data are used to derive empirical corrections in the regions which are known to be operated at non-nominal HV values. The values of the corrections are typically 1% to 7% and affect 2% of the $|\eta| < 2.5$ calorimeter acceptance. Most of these corrections are similar to the ones computed in ref. [1] with the exception of a few cases where the high-voltage setting was changed between Run 1 and Run 2.

These two corrections are validated by checking that the dielectron invariant mass in $Z \to ee$ events is uniform as a function of ϕ around the η–ϕ regions where these corrections are applied.

7 Data/MC energy scale and resolution measurements with $Z \to ee$ decays

7.1 Description of the methods

The difference in energy scale between data and MC simulation, after all the corrections described in section 6 have been applied to the data, is defined as α_i, where i corresponds to different regions

2019 JINST 14 P03017

in η. Similarly the difference in energy resolution is assumed to be an additional constant term in the energy resolution, c_i, depending on η:

$$E^{\text{data}} = E^{\text{MC}}(1+\alpha_i), \qquad \left(\frac{\sigma_E}{E}\right)^{\text{data}} = \left(\frac{\sigma_E}{E}\right)^{\text{MC}} \oplus c_i,$$

where the symbol $\oplus$ denotes a sum in quadrature.

For samples of $Z \to ee$ decays, with two electrons in regions i and j in η, the difference in average dielectron invariant mass is given at first order by $m_{ij}^{\text{data}} = m_{ij}^{\text{MC}}(1+\alpha_{ij})$ with $\alpha_{ij} = (\alpha_i+\alpha_j)/2$. The difference in mass resolution is given by $(\sigma_m/m)_{ij}^{\text{data}} = (\sigma_m/m)_{ij}^{\text{MC}} \oplus c_{ij}$, with $c_{ij} = (c_i \oplus c_j)/2$.

To extract the values of α_{ij} and c_{ij}, the shapes of the invariant mass distributions in data are compared with histograms of the invariant mass created from the simulation separately for each (i, j) region. In the simulation distributions the mass scale is shifted by α_{ij} and an extra resolution contribution of c_{ij} is applied. The best estimates of α_{ij} and c_{ij} are found by minimizing the χ^2 of the difference between data and simulation templates. The measurements are performed using only (i, j) regions which have at least 10 events and for which the kinematic requirement on the $\Delta\eta$ between the electrons does not significantly bias the Z mass peak position: the minimum invariant mass implied by the $\Delta\eta$ and E_{T} requirements must not exceed 70 GeV for a back-to-back configuration in ϕ. The α_i and c_i parameters are estimated from the α_{ij} and c_{ij} values by a χ^2 minimization of the overconstrained set of equations. The procedure is validated using pseudo-data samples generated from the simulation samples. From these studies, the residual bias of the method in the estimate of α_i and c_i parameters is computed, comparing the extracted values with the values used to generate the pseudo-data samples. This bias, which is assigned as an uncertainty, is typically (0.001–0.01)% for α_i and (0.01–0.03)% for c_i, depending on $|\eta|$.

Another method to derive the values of α_i and c_i is used as a cross-check of the results. In this second method, both the data and MC invariant mass distributions are fitted in each i-j bin by an analytic function. A sum of three Gaussian functions provides accurate modelling of the invariant mass distribution. The parameters describing these functions are fixed to the ones fitted in the simulation sample. When fitting the data, additional parameters corresponding to an overall energy-scale shift and a resolution correction per η region are added. These α_i and c_i parameters are then extracted from a simultaneous fit of all i-j regions. The procedure is optimized and validated using studies based on pseudo-data samples. The residual bias of the method is smaller than 0.01% in the energy scale and 0.1% in c_i, except in the transition region between the barrel and endcap calorimeters, where slightly larger effects are observed.

7.2 Systematic uncertainties

Several sources of uncertainty affecting the comparison of the dielectron invariant mass distribution in $Z \to ee$ events between data and simulation are investigated and their effects on the extraction of α_i and c_i are estimated.

- Accuracy of the method: the residual bias of the main method, estimated using pseudo-data samples, described in section 7.1, is assigned as a systematic uncertainty.

- Method comparison: the difference between the results of the two methods, discussed in section 7.1, is assigned as an uncertainty. For instance, the two methods have a different

2019 JINST 14 P03017

sensitivity to possible mismodelling of non-Gaussian tails in the energy resolution. The difference between the results of the two methods when applied to data can thus be larger than expected from the accuracy of the methods estimated using pseudo-data samples. In addition, for the c_i measurement, different implementations of the extraction of the c_i parameters from the measured c_{ij} values are compared.

- Mass range: the results are sensitive to the mass range used to perform the comparison between data and simulation if the non-Gaussian tails of the energy resolution are not accurately modelled. The mass range is changed from the nominal 80–100 GeV to 87–94.5 GeV; the difference is assigned as a systematic uncertainty.

- The selection used to remove i-j regions with a biased mass distribution is changed by varying the requirement on the minimum invariant mass implied by the $\Delta\eta$ selection in a given i-j region.

- Background with prompt electrons: the small contribution of backgrounds from $Z \to \tau\tau$, diboson pair production and top-quark production, leading to a dielectron final state with both electrons originating from τ-lepton or vector-boson decays, is neglected in the extraction of the parameters α_i and c_i. The procedure is repeated with the contributions from these backgrounds, as estimated from MC simulations, included in the mass template distribution. The differences between the results are assigned as systematic uncertainties in α_i and c_i.

- Electron isolation: the requirement on the electron isolation strongly rejects the backgrounds where at least one electron does not originate from a vector-boson or τ-lepton decay, but from semileptonic heavy-flavour decay, from conversions of photons produced in jets or from hadrons. To estimate the residual effect of these backgrounds on the result, the extraction of α_i and c_i is repeated without the isolation selection and the differences are assigned as systematic uncertainties.

- Electron identification: the selection uses Medium quality electrons. Small correlations between the electron energy response and the quality of the electron identification are expected, since the latter uses as input the lateral shower development in the calorimeter. If these correlations are not properly modelled in the simulation, the data-to-MC energy scale and resolution corrections can depend on the identification requirement. In order to make the corrections applicable to measurements using electron selections that are different from those used in this paper, additional systematic uncertainties are estimated by comparing the results for α_i and c_i obtained using the Tight identification requirement instead of the Medium quality requirement.

- Electron bremsstrahlung probability: electrons can lose a significant fraction of their energy by bremsstrahlung before reaching the calorimeter. To determine to what extent the measured α_i and c_i parameters are intrinsic to the calorimeter response and to what extent they are sensitive to the modelling of energy loss before the calorimeter, a requirement on the fraction of electron bremsstrahlung is applied, using the change in track curvature between the perigee and the last measurement before the calorimeter. The difference in α_i and c_i values obtained with or without this additional requirement applied is assigned as an uncertainty.

2019 JINST 14 P03017

Table 2. Ranges of systematic uncertainty in α_i and c_i for different η ranges.

	Uncertainty in α_i $\times 10^3$			Uncertainty in c_i $\times 10^3$		
$\lvert\eta\rvert$ range	0–1.2	1.2–1.8	1.8–2.4	0–1.2	1.2–1.8	1.8–2.4
Uncertainty source						
Method accuracy	(0.01–0.04)	(0.04–0.10)	(0.02–0.08)	(0.1–0.7)	(0.2–0.4)	(0.1–0.2)
Method comparison	(0.1–0.3)	(0.3–1.2)	(0.1–0.4)	(0.1–0.5)	(0.7–2.0)	(0.2–0.5)
Mass range	(0.1–0.5)	(0.2–4.0)	(0.2–1.0)	(0.2–0.8)	(1.0–3.5)	1.0
Region selection	(0.02–0.08)	(0.02–0.2)	(0.02–0.2)	(0–0.1)	0.1	(0.2–1.0)
Bkg. with prompt electrons	(0–0.05)	(0–0.1)	(0–0.5)	(0.1–0.4)	0.2	(0.1–0.2)
Electron isolation requirement	(0–0.02)	(0.02–5.0)	(0.02–0.20)	(0.1–0.9)	(0.1–1.5)	(0.5–1.5)
Electron identification criteria	(0–0.30)	(0.20–2.0)	(0.20–0.70)	(0–0.5)	0.3	0.0
Electron bremsstrahlung removal	(0–0.30)	(0.05–0.7)	(0.20–1.0)	(0.2–0.3)	(0.1–0.8)	(0.2–1.0)
Electron efficiency corrections	0.10	(0.1–5.0)	(0.10–0.20)	(0–0.3)	(0.1–3.0)	(0.1–0.2)
Total uncertainty	(0.2–0.7)	(0.5–10)	(0.6–2.0)	(0.3–1.2)	(1.0–6.0)	(2.0–3.0)

- Electron reconstruction, trigger, identification and isolation efficiencies: the MC simulation is corrected for the difference in efficiencies between data and simulation [10]. These corrections, which depend on E_{T} and η, can slightly change the shape of the invariant mass distribution predicted by the MC simulation. The corrections are varied within their uncertainties and the resulting uncertainty in α_i and c_i is estimated.

All the listed uncertainties are computed separately in each η interval. The typical values in different η ranges are given in table 2. The table shows a wide range of uncertainties for the interval $1.2 < |\eta| < 1.8$. Inside this interval, the uncertainties are largest for the region around $|\eta| = 1.5$. For $|\eta| > 2.4$, near the end of the acceptance, the uncertainties are significantly larger than for the other regions.

The total systematic uncertainty in α_i and c_i is computed adding in quadrature all the effects described above. This procedure may lead to slightly pessimistic uncertainties because some of the variations discussed above can double-count the same underlying source of uncertainty and also because the results must remain valid in a variety of final states and with different event selections. The systematic uncertainty in α_i varies from $\approx 0.03\%$ in the central part of the barrel calorimeter, to $\approx 0.1\%$ in most of the endcap calorimeter and reaches a few per mille in the transition region between the barrel and endcap calorimeters. The uncertainty in c_i is typically 0.1% in most of the barrel calorimeter, 0.3% in the endcap and as large as 0.6% in the transition region. The statistical uncertainty from the size of the $Z \to ee$ sample in the 2016 dataset is significantly smaller than the systematic uncertainty.

Uncertainties from the modelling of the Z boson production and decay, including the modelling of final-state QED radiation from the charged leptons, were investigated in ref. [1] and found to be negligible compared with the total uncertainty quoted above.

7.3 Results

The extraction of the energy scale correction is performed in 68 intervals in η. These intervals cover a range of 0.1 in the barrel calorimeter and are usually a bit smaller in the endcap calorimeter. The

2019 JINST 14 P03017

resolution corrections c_i are computed in 24 intervals. In each of these η regions, c_i corresponds to the effective additional constant term for the data after the fine-grained η-dependent energy scale corrections are applied.

Figure 7 shows the results for α_i and c_i from the 2015 and 2016 datasets. The energy scale correction factors are derived separately for the 2015 and 2016 datasets to take into account the difference in instantaneous luminosity between the two samples which is detailed in section 7.4. As the resolution corrections are consistent between the two years, they are derived from the combined dataset, after the energy scale correction has been applied.

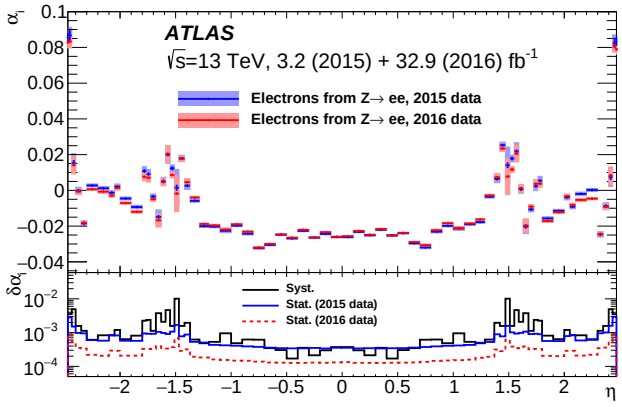

(a)

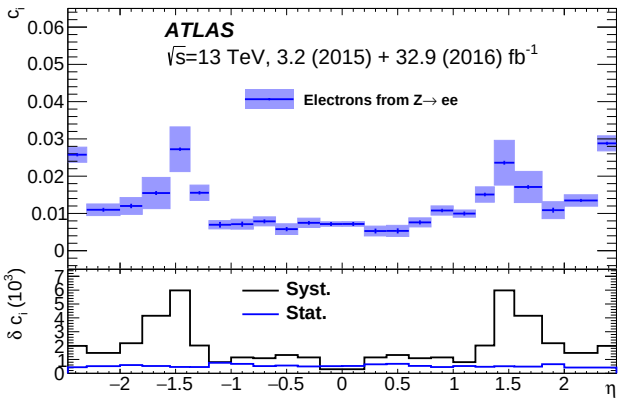

(b)

Figure 7. Results of the data-to-MC calibration from $Z \to ee$ events for (a) the energy scale corrections (α_i) and (b) the energy resolution corrections (c_i) as a function of η. The systematic and statistical uncertainties are shown separately in the bottom panels.

The additional constant term of the energy resolution present in the data is typically less than 1% in most of the barrel calorimeter. It is between 1% and 2% in the endcap, with slightly larger values in the transition region between the barrel and endcap calorimeters and in the outer $|\eta|$ range of the endcap.

No parameterization of the α_i as a function of ϕ is performed. The calorimeter uniformity in ϕ is typically at the 0.5–1% level and the residual variations of the energy response with ϕ

2019 JINST 14 P03017

contribute at this level to the additional constant term. These variations are a bit larger in the endcap calorimeter because of the larger variation of the calorimeter gaps under the influence of gravity as a function of ϕ.

Figure 8 shows a comparison of the invariant mass distribution for $Z \to ee$ candidates between data and simulation after the energy scale correction has been applied to the data and the simulation corrected for the difference in energy resolution between data and simulation. No background contamination is taken into account in this comparison. The non-($Z \to ee$) background is smaller than $\approx 1\%$ over the full shown mass range. The uncertainties in the ratio of the data and simulation distributions are computed varying the α_i and c_i correction factors within their uncertainties. These uncertainties are estimated as discussed in section 7.2 and take into account changes in the selections applied to $Z \to ee$ candidates and variations in the mass window used to extract the calibration. The decrease in the ratio near a mass of 96 GeV is most likely related to imperfect modelling of the tails of the energy resolution by the simulation, which affects the extraction of the energy scale and resolution correction factors. This variation is covered by the estimated uncertainties in the correction factors. Within these uncertainties, the data and simulation are in fair agreement.

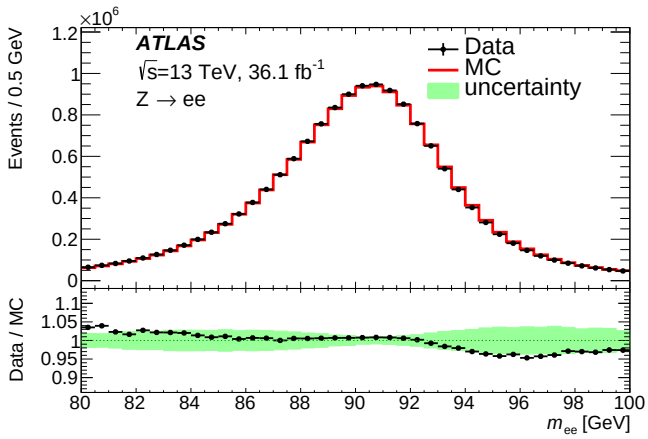

Figure 8. Comparison of the invariant mass distribution of the two electrons in the selected $Z \to ee$ candidates, after the calibration and resolution corrections are applied. The total number of events in the simulation is normalized to the data. The ratio is shown in the bottom plot. The uncertainty band of the bottom plot represents to the impact of the uncertainties in the calibration and resolution correction factors.

7.4 Stability of the energy scale, comparison of the 2015 and 2016 data

Figure 9 shows a comparison of the energy scale corrections extracted from the 2015 and 2016 data. Small differences up to a few per mille are observed, mostly in the endcap calorimeter. These effects can qualitatively be explained by the difference in instantaneous luminosity between the two years: the average instantaneous luminosity is around $0.3 \times 10^{34}\,\mathrm{cm}^{-2}\mathrm{s}^{-1}$ in 2015 and $10^{34}\,\mathrm{cm}^{-2}\mathrm{s}^{-1}$ in 2016. The following effects are expected to create small variations of the calorimeter response as a function of the luminosity:

- The large amount of deposited energy increases the temperature of the calorimeter, creating a small drop in the energy response of about –2%/K [30]. The LAr temperature is measured

2019 JINST 14 P03017

with probes inside the cryostat at the inner and outer radius of the endcap entrance face. The measured temperature increase is 0.07 K at the inner radius ($|\eta| = 2.65$) when collisions occur at high luminosity and 0.02 K at the outer radius ($|\eta| = 1.4$). The effect on the energy response is estimated assuming a linear temperature variation as a function of η in the endcap. In addition, there is a small change in the LAr temperature of the different cryostats in the absence of collisions between 2015 and 2016.

- The large amount of deposited energy in the liquid-argon gap creates a current in the HV lines. The current I induced on the HV line is equal to the total ionization current, from the drift of electrons and ions, which is created by the steady flux of deposited energy in the calorimeter. Since there is a significant resistance, R, between the power supply where the voltage is set to a constant value and the LAr gap, the voltage effectively applied to the gap is reduced by $R \times I$. The pattern of resistances across the LAr electrodes [31] is quite complex, but the dominant contribution to the resistance is due to the filter-box resistance in the high-voltage feedthrough [32]. The HV drop can thus be estimated from the current drawn by the power supply and the value of the filter-box resistance, which is 100 kΩ for the EM calorimeter ($|\eta| < 2.5$). The change in HV induces a change in the calorimeter response because the drift velocity of ionization electrons varies approximately with the power 0.3 of the electric field in the gap [33–35] and the amplitude of the shaped calorimeter signal is proportional to the drift velocity.

The predictions for the energy scale difference are included in figure 9. The changes observed in the data in the endcap are qualitatively reproduced although the difference seen in the data is somewhat smaller than expected for the highest $|\eta|$ values.

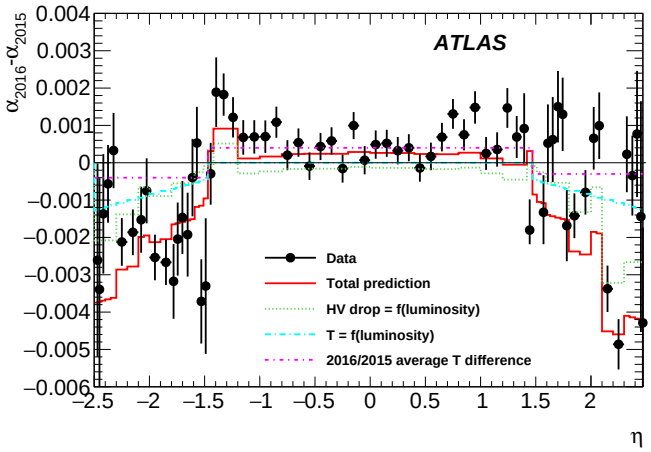

Figure 9. Comparison between the energy scale corrections derived from $Z \to ee$ events in 2015 and 2016 as a function of η. The difference of the energy scales measured in the data are compared with predictions taking into account the luminosity-induced high-voltage reduction and LAr temperature changes as well as the small overall difference in LAr temperature between 2015 and 2016.

Figure 10(a) shows the variation of the reconstructed peak position of the dielectron mass distribution as a function of the average number of interactions per bunch crossing for the data collected in 2016. When integrated over the full $|\eta|$ range, the variation of the energy scale with

2019 JINST 14 P03017

the number of interactions per bunch crossing is well below the 0.1% level in the data. No effect is visible in the simulation either. Figure 10(b) shows the stability of the energy scale as a function of time, probed with $Z \to ee$ events. The stability is significantly better than 0.1%.

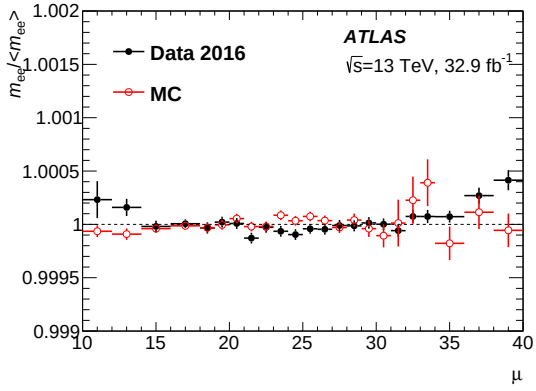

(a)

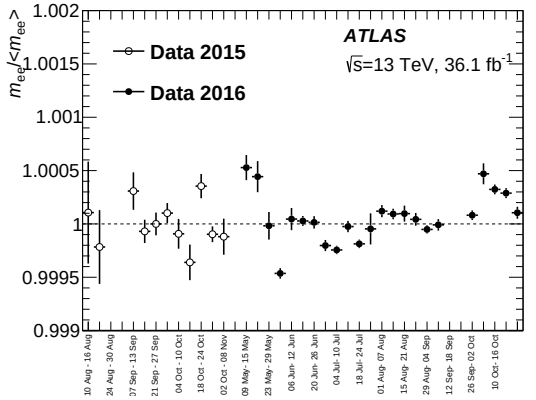

(b)

Figure 10. Relative variation of the peak position of the reconstructed dielectron mass distribution in $Z \to ee$ events (a) as a function of the average number of interactions per bunch crossing for the 2016 data and (b) as a function of time over the full 2015 and 2016 data-taking periods.

8 Systematic uncertainties in the energy scale and resolution

Several systematic uncertainties impact the measurement of the energy of electrons or photons (converted or unconverted) in a way that depends on their transverse energy and pseudorapidity. After the Z-based calibration, which fixes the energy scale and its uncertainty for electrons with transverse energy close to the average of those produced in Z decays, the relative uncertainty for any given electron or photon with transverse energy E_{T} and pseudorapidity η can be written as:

$$\delta E_i^{e,\gamma}(E_{\mathrm{T}}, \eta) = \Delta E_i^{e,\gamma}(E_{\mathrm{T}}, \eta) - \Delta E_i^{e}\left(\left\langle E_{\mathrm{T}}^{e(Z\to ee)}\right\rangle, \eta\right),$$

where $\Delta E_i^{e,\gamma}(E_{\mathrm{T}}, \eta)$ is, for a given uncertainty variation i, its relative impact on the energy as a function of η and E_{T} before the application of the Z-based calibration and $\left\langle E_{\mathrm{T}}^{e(Z\to ee)}\right\rangle \approx$ 40 GeV

2019 JINST 14 P03017

is the average transverse energy for electrons produced in Z boson decays. The Z-based calibration absorbs the effect for electrons with $E_{\mathrm{T}} = \left\langle E_{\mathrm{T}}^{e(Z\to ee)} \right\rangle$ and leaves the residual uncertainty $\delta E_i^{e,\gamma}(E_{\mathrm{T}}, \eta)$.

For a given uncertainty variation i, $\delta E_i^{e,\gamma}(E_{\mathrm{T}}, \eta)$ can change sign as a function of E_{T}. This is often the case for electrons where $\delta E_i^{e,\gamma}\left(\left\langle E_{\mathrm{T}}^{e(Z\to ee)} \right\rangle, \eta\right)$ is zero. In addition, for most of the considered uncertainty variations, their impact on photon energy is computed separately for reconstructed converted and unconverted photons. The converted photons have a shower development more similar to that of electrons and therefore usually smaller energy scale systematic uncertainties than unconverted photons. The different uncertainties affecting the energy scale of electrons and photons are described in this section.

8.1 Uncertainties related to pile-up

After correction, the energy shift induced by pile-up is estimated to be less than ±10 MeV in transverse energy (see section 6.3). The energy scale uncertainty after the Z-based calibration is thus $\delta E_i^{e,\gamma}(E_{\mathrm{T}}, \eta) = 10\,\mathrm{MeV}/E_{\mathrm{T}} - 10\,\mathrm{MeV}/\left\langle E_{\mathrm{T}}^{e(Z\to ee)} \right\rangle$. For electrons or photons with $E_{\mathrm{T}} = 10$ GeV, the uncertainty is $\approx 0.075\%$ and it is $\approx 0.02\%$ for $E_{\mathrm{T}} > 100$ GeV.

8.2 Impact of the layer calibration uncertainties

The uncertainties in the calibration of the first two layers of the calorimeter and of the presampler are discussed in sections 6.1 and 6.2. The impact of these uncertainties depends on the reconstructed particle energy since the fraction of energy observed in the presampler and in the different calorimeter layers is a function of the energy and of the particle type. Typically, the fraction of energy deposited in the presampler and in the first layer increases when the energy decreases and these fractions are higher for electrons and converted photons than for unconverted photons. The effect of the uncertainties in the layer calibration is propagated to the energy measurement using parameterizations of these fractions as a function of E_{T} and η. In the low-$|\eta|$ region of the barrel calorimeter, the impact of the uncertainties affecting the calibration of the different calorimeter layers and of the presampler is for instance $\approx \pm 0.2\%$ on the electron energy scale in the range $10 < E_{\mathrm{T}} < 200$ GeV.

Since only a small energy fraction is deposited in the third layer of the EM calorimeter, uncertainties in the relative calibration of this layer have a negligible impact on the total calibration uncertainty.

8.3 Impact of the E_4 scintillator calibration

In the region $1.4 < |\eta| < 1.6$, the signals of the E_4 scintillators are used as input to the energy measurement, as discussed in section 5. The accuracy of the calibration of the energy deposited in these scintillators varies from 4% to 6% depending on $|\eta|$. These uncertainties are based on the comparison of the energy deposited in E_4 between data and simulation for electrons from $Z \to ee$ events and the monitoring accuracy of the time-dependence of the reconstructed signal of the scintillator. The impact on the total electron energy is found to be typically 0.3 times the uncertainty in the E_4 scintillator calibration, where the factor 0.3 reflects the typical weight of the E_4 cell information in the calibration regression algorithm.

2019 JINST 14 P03017

8.4 Uncertainties due to the material in front of the calorimeter

The material in front of the calorimeter was studied in ref. [1] using data collected in 2012. The impact of the material on the energy response depends on the radial location of the material. Different uncertainty variations are thus considered for material in different regions in front of the calorimeter.

- Material inside the active area of the ID. From measurements performed during the detector construction [2], the material integral is known with a ±5% accuracy in four independent $|\eta|$ regions. In addition, uncertainties in the description of the material in the new innermost pixel layer and in the modified layout of the pixel detector services at low radius are added for the 2015–2016 data. These uncertainties (expressed in units of radiation lengths) range from 0.01 or less for $|\eta| < 1.5$ to 0.05 at $|\eta| = 2.0$ and 0.2 at $|\eta| = 2.3$. These uncertainties include the impact of missing some detector components in the description of the new innermost pixel layer and uncertainties in the description of the modified services for the detector description used in this paper, which corresponds to the *original* geometry model described in ref. [28].

- Material between the end of the active area of the ID and the presampler (or the calorimeter for $|\eta| > 1.8$) and material between the presampler and the calorimeter (for $|\eta| < 1.8$). The uncertainties in the amount of material in these regions are the same as the ones derived from the Run 1 studies, since the detector layout is unchanged. The amount of material in these regions was constrained by the longitudinal development of electron- and photon-induced showers in Run 1 data. The uncertainties include the longitudinal shower shape modelling uncertainties after calibration of the presampler and the first two calorimeter layers, in addition to the uncertainties in the GEANT4 simulation. The latter is estimated by varying the associated GEANT4 options to test refinements in the theoretical description of bremsstrahlung and photon conversion cross sections, as well as alternative electron multiple-scattering models. The total uncertainty in the amount of material between the end of the active ID area and the presampler is typically 0.03 to 0.1 radiation lengths for $|\eta| < 1.4$, up to 0.7 radiation lengths at $|\eta| = 1.5$ and 0.1 to 0.3 radiation lengths for $1.5 < |\eta| < 1.8$. The uncertainty in the amount of material between the presampler and the first calorimeter layer is typically 0.04 to 0.1 radiation lengths in the full range $|\eta| < 1.8$. Finally, the uncertainty in the material in front of the calorimeter for the region $1.8 < |\eta| < 2.5$ is about 0.1 to 0.15 radiation lengths.

In the low-$|\eta|$ region of the barrel calorimeter, the total uncertainties related to the description of material in front of the calorimeter give an uncertainty in the energy scale of ±0.3% for E_{T} =10 GeV electrons. This uncertainty increases to ±0.5% at $|\eta| = 2.3$.

8.5 Non-linearity of the cell energy measurement

Non-linearity in the cell energy measurement induces a dependence of the energy response on the energy of the particle. The linearity of the readout electronics is better than 0.1% [4] in each of the three gains used to digitize the calorimeter signals in the ranges where they are used to collect data. However, the relative calibration of the different readout gains is less well known. To study the accuracy of this relative calibration, data recorded under special conditions in 2015 and 2017

2019 JINST 14 P03017

are used, corresponding to an integrated luminosity of 12 pb^{-1} in 2015 and 160 pb^{-1} in 2017. For these data, the threshold to switch from high gain (HG) to medium gain (MG) readout for the cells in the second layer was significantly lowered, by a factor 5. With this special configuration, almost all electrons from Z boson decays have at least the highest-energy cell in layer two recorded in the MG readout. In the standard configuration, the HG readout is almost always used, at least in the barrel, where the transition between the two gains is typically at an energy of ≈ 25 GeV for the cells in the second layer at low $|\eta|$.

The reconstructed dielectron invariant mass distribution in these data is compared with the one in data recorded with the standard gain transition configuration taken around the same time. To properly calibrate the ADC-to-current conversion function for low numbers of ADC counts in the MG range in the special configuration, a non-linear ADC-to-current conversion is used, derived from dedicated pulser calibration runs. Uncertainties at the 0.05% level in this conversion can arise from non-linearity of the calibration system for this situation.

Figure 11 shows the measured values of the energy scale difference between the two datasets, α_{G}, as a function of $|\eta|$. If the HG and MG are perfectly intercalibrated, α_{G} will be zero. A small but significant difference is observed, especially in the region $0.8 < |\eta| < 1.37$. Further investigations did not reveal any significant energy dependence or further η dependence of this effect. The observed difference is assigned as a systematic uncertainty. This uncertainty is assumed to be a scale factor between the calibration of the two gains, independent of the cell energy.

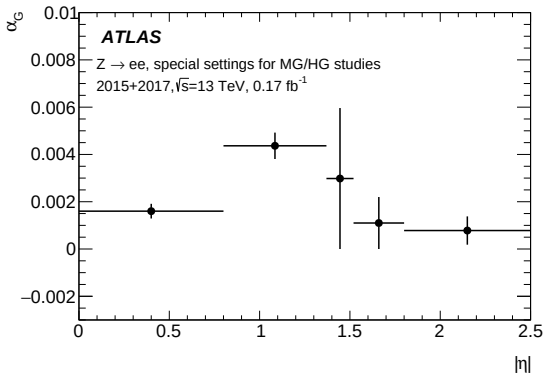

Figure 11. Difference of energy scales, α_{G}, extracted from $Z \to ee$ events, as a function of $|\eta|$ between data recorded with the standard thresholds for the transition between HG and MG in the readout of the layer-two cells and data with lowered thresholds. Only statistical uncertainties are shown.

From this measurement, the impact of the gain intercalibration uncertainty for data taken under standard conditions can be written as a function of the particle type and of E_{T} and η as follows:

$$\frac{\Delta E}{E} = \alpha_{\text{G}}(\eta) \cdot \frac{1}{\delta_Z(\eta)} \cdot \delta_{\text{G}}^{e,\gamma}(\eta, E_{\text{T}})$$

where:

- $\alpha_{\text{G}}(\eta)$ is the measured energy scale difference as a function of η from $Z \to ee$ decays, comparing the data recorded with lower gain threshold with data recorded in standard conditions.
- $\delta_Z(\eta)$ quantifies the fractional change in energy for electrons from Z boson decays between the data with lower and standard thresholds for a given change in the energy recorded in MG

2019 JINST 14 P03017

in the second layer. This sensitivity factor is about 0.3 to 0.4 in the barrel calorimeter and about 0.2 to 0.25 in the endcap calorimeter. It takes into account the fact that only a fraction of the electron energy is recorded in MG layer-two cells in the data with special settings and that in the data with normal settings some layer-two cells can be read out in MG, especially in the endcap where the electron energies are larger.

- $\delta_{\mathrm{G}}^{e,\gamma}(\eta, E_{\mathrm{T}})$ quantifies, for a given particle, the fractional change in the total energy for a given change in the energy recorded in MG in the second layer, when the standard settings of the gain threshold are used. It is estimated using simulated single-particle samples. It is close to 0 up to $E_{\mathrm{T}} \approx 40$ to 60 GeV, depending on η and on the particle type, and then rises to reach an asymptotic value of about 0.8 for E_{T} above a few hundred GeV, reflecting the fraction of electron energy measured with second-layer cells read out in MG.

The calibration uncertainty for the low-gain readout is assumed to be the same as for the MG. The low-gain readout is used in the second layer for electrons or photons with transverse energy above 350 to 500 GeV (100 to 300 GeV) depending on η in the barrel (endcap). Studies of a small sample of high transverse momentum Z boson decays, where some of the electrons are recorded in low gain, do not indicate any significantly larger effect.

The uncertainty in the total energy is typically 0.05% to 0.1% depending on η for photons of $E_{\mathrm{T}} = 60$ GeV. It reaches 0.2% to 1% for very high energy electrons and photons.

The uncertainty in the MG-to-HG relative calibration in the first layer has a much smaller effect than the one in the second layer, except in the endcap for $1.8 < |\eta| < 2.3$. In this region, the relative calibration of the two gains in the first layer was found to be sensitive to the pile-up-dependent optimization of the optimal filtering coefficients with an uncertainty rising from 1% to 5%. In this region, the highest-energy cell in the first layer of most high-E_{T} electromagnetic showers is recorded in MG. The application of the muon-based layer calibration to electrons or photons therefore leads to an uncertainty in the energy scale for electrons or photons, which reaches about 0.8% for unconverted photons with $|\eta| > 2.0$.

In the studies reported in ref. [1], the gain calibration uncertainty was investigated by splitting the sample of Z boson decays recorded in standard conditions according to the gain used to measure the highest-energy cell in the second layer. The uncertainty estimated in this way combined the effect of the genuine intercalibration of the different readout gains with systematic effects related to the modelling of lateral shower shapes. The latter impacts a selection based on the gain of the highest-energy cell since showers with narrow lateral shape are more likely to have a second-layer cell with high energy deposit and thus are more likely to have this cell recorded in MG. For the results presented in this paper, the two uncertainties are separated with the relative gain calibration discussed above and with a separate investigation of the impact of the modelling of lateral shower shape on the energy response, reported in section 8.6.

8.6 Modelling of the lateral shower shape

Any energy-dependent mismodelling of the energy response as a function of the lateral shower shape can create differences between data and simulation in the energy response relative to the energy response for electrons at $E_{\mathrm{T}} = 40$ GeV, the average value of E_{T} for electrons from Z boson decays.

2019 JINST 14 P03017

Two effects are investigated to derive uncertainties related to the modelling of the lateral shower shape:

- The variation of the electron energy response as a function of the shower width in the η direction is studied using Z boson decays. The measured differences between data and simulation are used to derive uncertainties in the energy response for electrons and photons of any transverse energy.

- To take into account possible differences between electron and photon showers related to the different interaction probabilities with the material in front of the calorimeter, the lateral energy leakage in the calorimeter outside the area of the cluster is studied directly in data and simulation. From the differences between data and simulation, an uncertainty in the photon energy calibration is derived.

To characterize the lateral shower shape in the η direction, the measurement of the shower width using first-layer cells (ω_{stot}) is used. The variable ω_{stot} is defined as the RMS of the energy distribution as a function of η using all first-layer cells included in the cluster. The energy response as a function of the lateral shower shape is investigated by examining the reconstructed Z mass as a function of ω_{stot}, separately for data and simulation. This is illustrated in figure 12. In most of the detector, the difference between data and simulation is small albeit not zero. However, in the region around $|\eta| = 1.7$ a large difference between data and simulation is observed. This area is where the material in front of the calorimeter is the largest. Changes in the amount of material in the simulation do not, however, reproduce the effect observed in data. In addition, an overall difference in lateral shower shape, as observed in refs. [36] and [37], can also induce a difference in the energy response, even if the dependence of the energy response on the shower width is the same in data and simulation. A systematic uncertainty in the energy response from the dependence of the energy response on the shower width is thus estimated.

This uncertainty, taking into account the calibration performed with $Z \to ee$ events, can be estimated as

$$\begin{aligned}\frac{\Delta E}{E}(E_{\text{T}}, \eta) = & A \times \left[\left\langle \omega^{e,\gamma}_{\text{stot}}(\text{data}, E_{\text{T}}, \eta) \right\rangle - \left\langle \omega^{e}_{\text{stot}} \left(\text{data}, \left\langle E_{\text{T}}^{e(Z\to ee)} \right\rangle, \eta \right) \right\rangle \right] \\ & - B \times \left[\left\langle \omega^{e,\gamma}_{\text{stot}}(\text{MC}, E_{\text{T}}, \eta) \right\rangle - \left\langle \omega^{e}_{\text{stot}} \left(\text{MC}, \left\langle E_{\text{T}}^{e(Z\to ee)} \right\rangle, \eta \right) \right\rangle \right],\end{aligned}$$

where A (B) is the slope of the energy response as a function of ω_{stot} in data (MC simulation) in a given η bin. This slope is extracted from the variation of the dielectron mass as a function of ω_{stot} in $Z \to ee$ events. The variation of ω_{stot} as a function of E_{T} and η for electrons and photons is parameterized from the $Z \to ee$ and inclusive photon samples separately for data and MC simulation. Simulated single-particle MC samples are used to extrapolate the behaviour to the highest energies.

The resulting energy scale uncertainty is significantly smaller than 0.1% in most of the detector acceptance except in the region with $|\eta|$ between 1.52 and 1.82 where it is up to 1% for electrons with $E_{\text{T}} > 500$ GeV, up to 1.5% for unconverted photons with $E_{\text{T}} > 400$ GeV and around 0.5% for converted photons.

The lateral energy leakage in the calorimeter is estimated as the difference between the energy collected in an area corresponding to 7×11 second-layer cells and the energy collected in the

2019 JINST 14 P03017

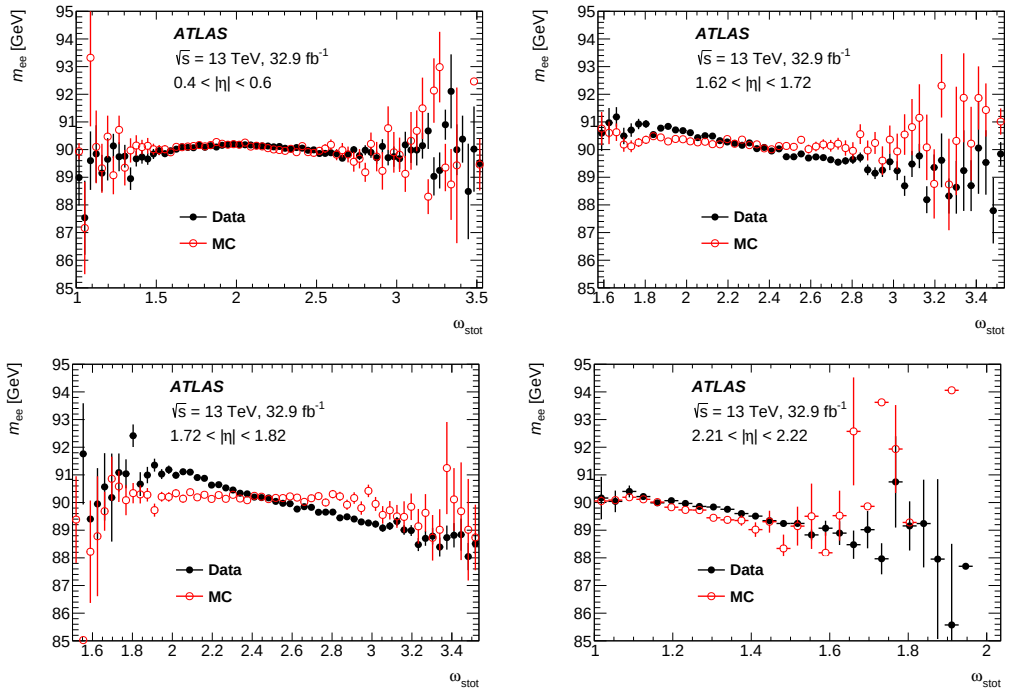

Figure 12. The mean of the dielectron mass for Z candidates (m_{ee}), in data and simulation, as a function of the lateral shower width (ω_{stot}) for different regions in $|\eta|$.

cluster size, which is 3×7 (5×5) second-layer cells in the barrel (endcap) calorimeter. The leakage measured for photons from radiative Z boson decays is compared with the leakage measured for electrons from Z decays. This is done separately for converted and unconverted photons in wide $|\eta|$ regions and for transverse energies below and above 25 GeV.

The energy measured in 7×11 layer-two cells is corrected for the pile-up-induced energy shifts, in the same way as for the cluster energy (see section 6.3). Figure 13 shows the distribution of the energy leakage for electrons and unconverted photons with $E_{\text{T}} > 25$ GeV in the $|\eta|$ range 0 to 0.8. The average leakage is larger in the data than in the simulation, which is consistent with a wider lateral shower shape in data. The differences between data and simulation are, within statistical uncertainties, mostly consistent between electrons and photons. To quantify the effect, the double difference of lateral leakage between electrons and photons and between data and simulation is investigated. The largest deviations of the double difference from zero are observed for converted photons with $|\eta| < 0.8$, with a value of $(0.25\pm0.10_{\text{stat}})\%$ and for unconverted photons across the full η range where an average value of around -0.1% is observed. The impact of the photon conversion reconstruction and the classification between converted and unconverted photon categories is estimated by applying the procedure discussed in section 8.7. The measured double differences are taken as additional systematic uncertainties in the photon energy calibration. If the double difference is consistent with zero within its statistical uncertainty, the statistical uncertainty is taken instead as an estimate of the systematic uncertainty.

2019 JINST 14 P03017

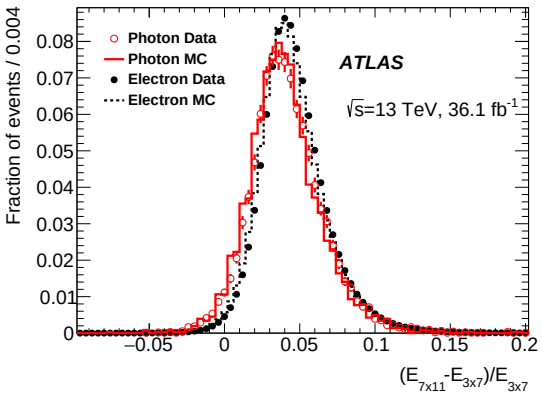

Figure 13. Distributions of the lateral leakage in data and simulation for electron and unconverted photon candidates with $E_{\mathrm{T}} > 25$ GeV and $|\eta| < 0.8$. Photons from $Z \to \ell\ell\gamma$ decays are compared with electrons from $Z \to ee$.

8.7 Modelling of the photon reconstruction classification

The energy estimating algorithm (section 5.1) is trained separately for reconstructed converted and unconverted photons. Misclassifications in conversion category arise from inefficiencies in the conversion-finding algorithm and from fake classification of genuine unconverted photons as converted photons by matching the cluster to pile-up-induced track(s). For conversions occurring at a radius smaller than 800 mm from the beam line, the typical reconstruction efficiency, as estimated by the simulation, is 65% to 85% depending on η. The fake rate, i.e. the fraction of genuine unconverted photons reconstructed as converted photon candidates, is typically 1% to 4% depending on η for the pile-up conditions of the 2015 and 2016 datasets. The efficiency and fake rate are smaller for $|\eta| > 2.0$ where the absence of transition radiation tracker coverage does not allow reconstruction of photon conversions occurring at large radius.

If the misclassification rate is different between data and simulation, a bias in the photon energy scale is induced. The efficiency and fake rate are studied using a sample of radiative Z boson decays, $Z \to \mu\mu\gamma$ [8]. The longitudinal shower shape of the photon candidates is used to provide a statistical discrimination between genuine converted and unconverted photons and to estimate the efficiencies and fake rate in both data and simulation. The ratio of the efficiencies of the conversion finding algorithm in data and simulation is typically around 0.9. The ratio of fake rates is between 1 and 1.7 depending on η. The impact on the photon energy measurement is estimated by reweighting the MC events with the data-to-MC ratio of efficiencies and fake rates. The uncertainty is taken as the difference between this reweighted MC sample and the original MC sample. This is done separately for the efficiency and the fake rate, which are treated as independent uncertainty sources. A change of the conversion-finding efficiency mostly affects the energy scale of the reconstructed unconverted photon candidates while a change in the fake rate mostly affects the sample of reconstructed converted photon candidates. For photons with $E_{\mathrm{T}} = 60$ GeV, the uncertainty in the energy scale is about 0.04% (0.2% to 0.02%) in the barrel (endcap) for reconstructed unconverted photon candidates and about 0.05% (0.005%) in the barrel (endcap) for reconstructed converted photon candidates.

2019 JINST 14 P03017

Table 3. List of the different independent systematic uncertainties affecting the energy calibration and their divisions in $|\eta|$ regions between which the uncertainties are not correlated. Uncertainties with one $|\eta|$ region are fully correlated across the full η acceptance.

Uncertainty source		Number of $\|\eta\|$ regions
$Z \to ee$ calibration	Statistical uncertainty	1
	Systematic uncertainty	1
Cell energy non-linearity	Medium Gain/High Gain layer 2	1
	Medium Gain/High Gain layer 1	1
	Pile-up shift	1
Layer 1/Layer 2 calibration	$\alpha_{1/2}$ μ measurement	5
	$\alpha_{1/2}$ $\mu \to e$ extrapolation	2
Presampler calibration	Module spread	8
	Uncertainty for last EMB module	1
	$b_{1/2}$ correction	1
Barrel-endcap gap scintillator ($1.4 < \|\eta\| < 1.6$)	Scintillator calibration	3
ID material	Run 1 detector construction	4
	Run 2 inner most pixel layer description	1
	Pixel services description	1
Material presampler (PS) to calorimeter	Run 1 measurement with unconv. photon	9
($\|\eta\| < 1.8$)	Simulation of long. shower shape unconv. photon	2
Material ID to presampler	Run 1 measurement with electrons	9
($\|\eta\| < 1.8$)	Simulation of long. shower shape electrons	2
Material ID to calorimeter	Run 1 measurement with electrons	3
($\|\eta\| > 1.8$)	Simulation of long. shower shape electrons	1
All material ID to calorimeter	Variations of GEANT4 physics list	1
Lateral shower shape modelling	Dependence on shower η width	1
	Lateral leakage for unconv. photons	1
	Lateral leakage for conv. photons	1
Conversion reconstruction	Conversion efficiency	1
	Conversion fake rate	1
	Radius dependence of conversion reconstruction	1

8.8 Summary of systematic uncertainties in the energy scale

The systematic uncertainties are described by a set of 64 independent uncertainty variations. A given systematic uncertainty can be described by multiple variations for different regions in $|\eta|$. The list of these uncertainties is given in table 3. For simplification, only one uncertainty variation is assigned to the statistical accuracy of the $Z \to ee$ calibration since this uncertainty is always negligible compared with the other uncertainties.

Figure 14 illustrates the impact of the main systematic uncertainties affecting the energy scale of electrons, unconverted photons and converted photons at $|\eta| = 0.3$ as a function of the transverse energy. For a given uncertainty variation, the effect on the energy can be positive or negative with a possible change of sign near the average E_{T} of electrons from Z decays. This is illustrated in this figure by showing the signed uncertainty, i.e. the impact of a one-sided variation of the systematic

2019 JINST 14 P03017

uncertainties. The opposite-sign variation will give a systematic impact with the opposite sign. Keeping track of the relative sign across E_{T} and η of the impact of each uncertainty source is important for properly computing the total uncertainty for a sample covering a range of E_{T} and η values. At given values of both E_{T} and η, the total systematic uncertainty is given by the sum in quadrature of the uncertainties related to each of the independent uncertainty sources.

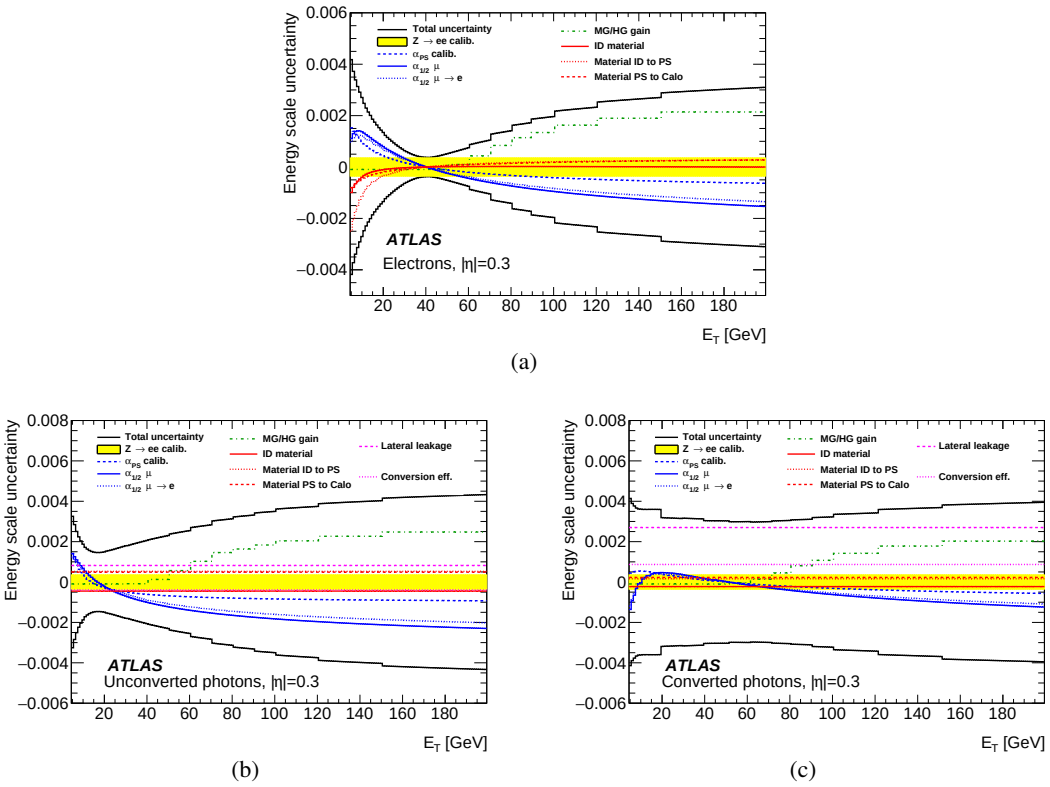

(a)

(b)

(c)

Figure 14. Fractional energy scale calibration uncertainty for (a) electrons, (b) unconverted photons and (c) converted photons, as a function of E_{T} for $|\eta| = 0.3$. The total uncertainty is shown as well as the main contributions, which are represented by the signed impact of a one-sided variation of the corresponding uncertainty. Only a one-sided variation for each uncertainty is shown for clarity.

Figure 15 summarizes the total uncertainty in the energy scale as a function of η for electrons and photons for given values of transverse energy. Uncertainties for converted and unconverted photons are shown separately.

To illustrate the η-dependence of the different uncertainties, table 4 gives the photon energy scale systematic uncertainties for $E_{\mathrm{T}} = 60$ GeV in wide η regions corresponding to either the barrel or the endcap acceptance. A uniform η distribution of the photons is assumed. The typical photon energy scale uncertainty is 0.2% to 0.3% averaged over the barrel and 0.45% to 0.8% in the endcap. For this value of E_{T}, the uncertainties from the relative calibration of the different layers is significantly smaller for converted photons than for unconverted photons as they have a longitudinal shower development closer to that of $E_{\mathrm{T}} = 40$ GeV electrons. The cell energy non-linearity uncertainty is higher for unconverted photons as they have a higher probability to use medium-gain readout in the second layer, given that they deposit a higher energy fraction in the

2019 JINST 14 P03017

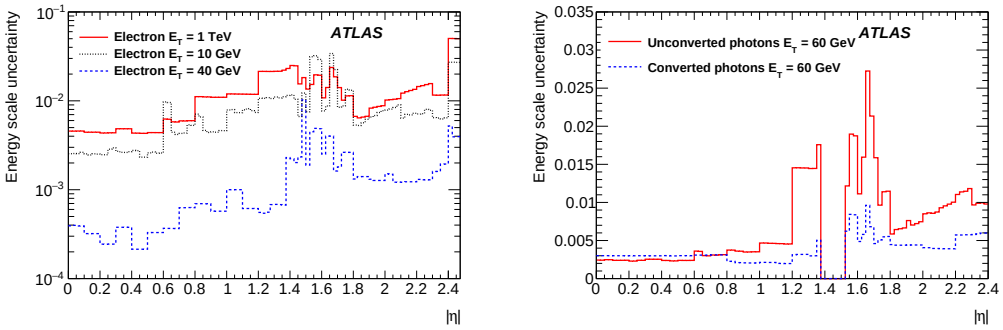

Figure 15. Total fractional systematic uncertainty in the energy scale as a function of $|\eta|$ for (a) electrons of E_{T} = 10 GeV, 40 GeV and 1 TeV and (b) photons of E_{T} = 60 GeV.

Table 4. Photon energy scale fractional systematic uncertainty for a sample with uniform η distribution at E_{T} = 60 GeV, with the contributions of the different types of uncertainties.

Systematic category	Photon energy scale uncertainty $\times 10^3$			
	$\lvert\eta\rvert < 1.37$		$1.52 < \lvert\eta\rvert < 2.37$	
	Unconverted	Converted	Unconverted	Converted
$Z \to ee$ calib.	0.45	0.45	1.41	1.41
Cell energy non-linearity	0.88	0.10	3.89	0.38
Layer (presampler, E1/E2, scintillator) calibration	2.34	0.29	3.04	0.60
ID material	0.96	0.82	3.71	3.89
Other material	1.66	0.26	3.19	1.02
Conversion reconstruction	0.40	0.99	0.76	0.97
Lateral shower shape modelling	1.03	1.95	3.20	0.85
Total	3.37	2.41	7.81	4.50

second calorimeter layer. The total uncertainties are only partially correlated between converted and unconverted photons.

8.9 Energy resolution uncertainties

The different contributions to the energy resolution are: the shower and sampling fluctuations in the calorimeter, the fluctuations in energy loss upstream of the calorimeter, the effect of electronics and pile-up noise and the impact of residual non-uniformities affecting the measurement of the energy in the data. The total contributions of the effects of shower and sampling fluctuations, energy loss before the calorimeter and electronics noise are given in section 5. The intrinsic energy resolution, defined as the expected resolution in the absence of upstream material and with uniform response, is derived from the energy resolution in the simulation of genuine unconverted photons. A 10% relative uncertainty is assumed for this intrinsic energy resolution, based on test-beam studies [38]. The impact of uncertainties in the detector material upstream of the calorimeter on the energy resolution is derived from simulations with additional material as described in section 8.4. The uncertainty in the electronics and pile-up noise modelling is derived from a comparison of data

2019 JINST 14 P03017

and simulation for a sample of zero-bias events introduced in section 6.1. The noise is typically 350–400 MeV expressed in transverse energy. The noise uncertainty is defined as the difference in quadrature between the noise in data and simulation and is found to be 100 MeV in terms of transverse energy. Finally, the energy resolution's constant term is derived from the data-to-simulation comparison of the energy resolution for electrons from $Z \to ee$ decays, as described in section 7.

A formalism similar to that for the energy scale uncertainty can be used to describe the resolution uncertainties. If $\Delta\sigma_i^{e,\gamma}(E_{\mathrm{T}}, \eta)$ is the uncertainty in the relative energy resolution for a given particle from a given uncertainty variation i, the residual uncertainty after the adjustment of the resolution based on the Z decays can be written as

$$\delta\Sigma_i^{e,\gamma}(E_{\mathrm{T}}, \eta) = \Delta\Sigma_i^{e,\gamma}(E_{\mathrm{T}}, \eta) - \Delta\Sigma_i\left(\left\langle E_{\mathrm{T}}^{e(Z\to ee)}\right\rangle, \eta\right),$$

where Σ denotes the square of the relative energy resolution σ.

The uncertainty in the energy resolution comparison between data and simulation for $Z \to ee$ decays is described by an additional uncertainty in the constant term of the energy resolution.

Figure 16 shows the energy resolution, its total uncertainty and the different contributions to the total relative uncertainty in the resolution as a function of transverse energy for electrons and unconverted photons at two different η values. The uncertainty $\Delta\Sigma_i^{e,\gamma}(E_{\mathrm{T}}, \eta)$ due to the material in front of the calorimeter is estimated as the change of the core Gaussian component of the energy resolution in simulated single-particle samples with different amounts of material in front of the calorimeter. The term $\Delta\Sigma_i\left(\left\langle E_{\mathrm{T}}^{e(Z\to ee)}\right\rangle, \eta\right)$ is computed from simulated $Z \to ee$ samples. Energy resolution corrections are derived by comparing samples simulated with additional material with the nominal geometry simulation, following the same procedure as used for the data and discussed in section 7.

For electrons or photons in the transverse energy range 30–60 GeV, the energy resolution is known to a precision of the order of 5% to 10%. For high-energy electrons or photons, where the resolution is better, the relative uncertainty in the energy resolution reaches 20% to 50%. Compared with the results reported in ref. [1], the main change is the smaller uncertainty in the constant term of the energy resolution extracted from the $Z \to ee$ samples. This uncertainty reduction is mainly due to an improvement of the validation step performed on pseudo-data as discussed in section 7.1 and from better agreement between the two methods considered.

9 Cross-checks with $J/\psi \to ee$ and $Z \to \ell\ell\gamma$ decays

9.1 $J/\psi \to ee$ decays

The energy scale of low-energy electrons (average transverse energy around 10 GeV) is probed using $J/\psi \to ee$ events. The known mass of the J/ψ resonance provides a completely independent check of the energy calibration for low-energy electrons. The full calibration procedure discussed in the previous sections, including the energy scale derived from $Z \to ee$ events, is applied. The difference between data and simulation for $J/\psi \to ee$ events is then quantified using residual energy scale differences, $\Delta\alpha$, extracted from the peak positions of the reconstructed invariant mass. The formalism is very similar to the one used for the $Z \to ee$ data-to-simulation energy scale corrections,

2019 JINST 14 P03017

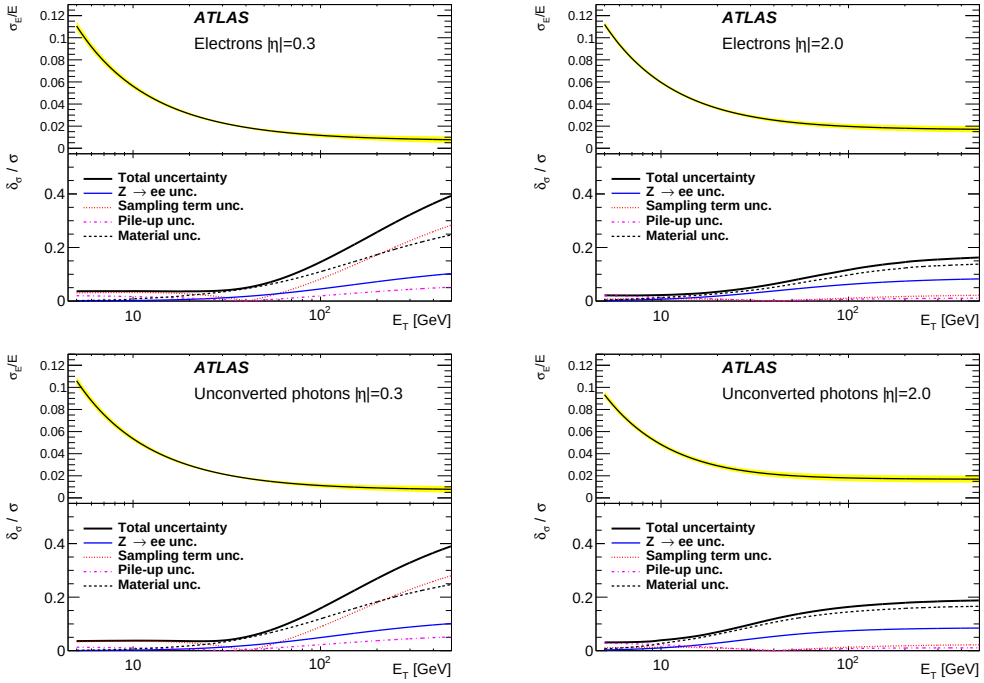

Figure 16. Relative energy resolution, σ_E/E, as a function of E_{T} for electrons and unconverted photons at $|\eta| = 0.3$ and $|\eta| = 2.0$. The yellow band in the top panels shows the total uncertainty in the resolution. The breakdown of the relative uncertainty in the energy resolution, δ_σ/σ is shown in the bottom panels.

but fewer $|\eta|$ regions are defined, given the smaller size of the collected $J/\psi \to ee$ sample. If the energy calibration is correct, $\Delta\alpha$ should be consistent with zero within the combined uncertainties of the $J/\psi \to ee$ measurement and the systematic uncertainty of the energy calibration. The event selection and data and MC samples are introduced in section 4.

To compare data and simulation, the relative fraction of J/ψ produced in b-hadron decays compared to promptly produced J/ψ is determined, since the electrons from J/ψ produced in b-hadron decays are less isolated. This fraction is extracted from a fit to the proper decay-time distribution, following the procedure discussed in ref. [39]. The fraction of prompt J/ψ is found to be between 68% and 83% depending on the E_{T} requirement imposed on the electron with highest E_{T}, with uncertainties between 3% and 14%.

To extract the energy scale differences between data and simulation from J/ψ events, a procedure similar to the simultaneous fit used for $Z \to ee$ events, described in section 7.1, is applied. The significant contributions from the continuum background and the $\psi(2S)$ resonance have to be taken into account. The typical signal-to-background ratio integrated over the 2.6–3.4 GeV mass range, which contains most of the signal, is around 10 to 1.

The dielectron invariant mass distribution in the range 2.1 to 4.1 GeV is described by the following function:

$$f(m_{ee}) = f^{\mathrm{DSCB}}_{J/\psi}(m_{ee}) + f^{\mathrm{DSCB}}_{\psi(2S)}(m_{ee}) + f^{\mathrm{bkg}}(m_{ee}) \tag{9.1}$$

with the J/ψ and $\psi(2S)$ mass distributions described by a double-sided Crystal Ball function (f^{DSCB}) and the background mass distribution (f^{bkg}) described by a second-order Chebyshev polynomial.

2019 JINST 14 P03017

Since in the simulation the continuum background is not considered, the last term is used only when fitting data.

The parameters describing the $\psi(2S)$ mass distribution are related to the ones describing the J/ψ mass distribution by a scaling factor equal to the ratio of the masses of these two resonances. All the parameters but the m_{ee} peak position are fixed to the DSCB parameters extracted from the MC samples. This free parameter is expressed as a function of $\Delta\alpha$. The $\Delta\alpha$ factors are extracted from a simultaneous fit of the different i-j data regions in η. The normalizations of the J/ψ, $\psi(2S)$ and background yields as well as the parameters describing the background shape are also free in the fit.

The systematic uncertainties affecting the extraction of $\Delta\alpha$ include the uncertainties in the shape of the signal mass distribution (choice of DSCB function and parameters of the DSCB functions), in the modelling of the background mass distribution, in the results of the proper-time fit and in the modelling of the η distribution of the electrons in the simulation. These systematic uncertainties are significantly smaller than the statistical uncertainties.

Figure 17 shows the extracted $\Delta\alpha$ values with their uncertainties as a function of η. They are compared with the systematic uncertainty of the calibration procedure for electrons with the E_{T} distribution of those observed in the J/ψ sample. No measurement is reported in the transition region between the barrel and endcap calorimeters due to the limited measurement accuracy in this region. The uncertainty in the calibration for low-E_{T} electrons arises mostly from uncertainties in the amount of material in front of the calorimeter and in the relative calibration of the different calorimeter layers. Good agreement is observed between the residual energy scale differences and the calibration described in this paper. This agreement confirms that the method to extract the nominal scales and the estimate of the systematic uncertainties are valid over a wide range of electron energies.

The width of the reconstructed $J/\psi \rightarrow ee$ mass distribution can also be used to probe the energy resolution for low-energy electrons. The observed width in the data is consistent with the predicted resolution within its uncertainties.

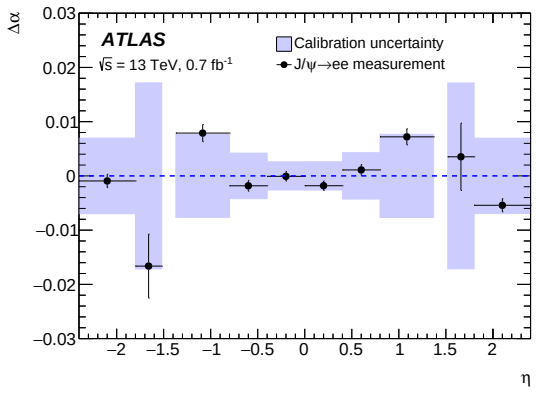

Figure 17. Residual energy scale differences, $\Delta\alpha$, between data and simulation extracted from $J/\psi \rightarrow ee$ events as a function of η. The points show the measurement with its total uncertainty. The band shows the uncertainty of the energy calibration for the energy range of the $J/\psi \rightarrow ee$ decays.

2019 JINST 14 P03017

9.2 $Z \to \ell\ell\gamma$ decays

The energy scale correction of photons is assumed to be the same as the one extracted from $Z \to ee$ decays, as described in section 7, within the uncertainties described in section 8. The radiative decays of the Z boson can be used to check the energy scale of photons, in the low-energy region in particular. Converted and unconverted photons are studied separately. The electron and muon channels are treated independently and then combined. All the corrections previously described are applied to electrons and photons, and residual energy scale factors for photons are derived by comparing the data with simulations. The samples of simulated events and the selection are described in section 4.

The residual photon energy scale difference is parameterized as an additional correction to the photon energy $\Delta\alpha$, similarly to the J/ψ study. The mass distribution of the $\ell\ell\gamma$ system in the simulation is modified by applying $\Delta\alpha$ to the photon energy and the value of $\Delta\alpha$ that minimizes the χ^2 comparison between the data and the simulation is computed. A second method based on an analytic function adjusted to the simulation to describe the shape of the mass distribution is also investigated. The two methods give consistent results.

The measurement is limited by the statistical accuracy. The considered systematic uncertainties are from the lepton energy scale and the background contamination, and they are negligible compared with the statistical uncertainty.

Figure 18 shows the measured $\Delta\alpha$ as a function of E_{T}, separately for converted and unconverted photons. The value of $\Delta\alpha$ is consistent with zero within the uncertainties in the measurement and in the photon energy scale.

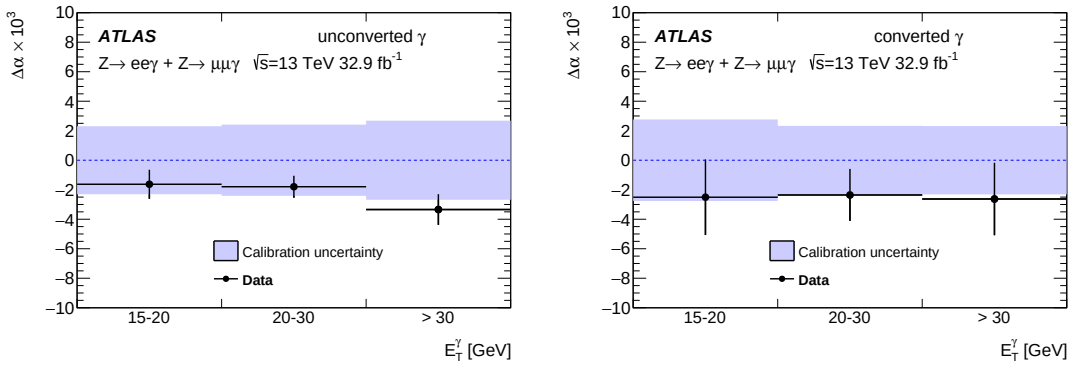

(a) (b)

Figure 18. Residual energy scale factor, $\Delta\alpha$, for (a) unconverted and (b) converted photons with their uncertainties. The points show the measurement with its total uncertainty. The superimposed band represents the full energy calibration uncertainty for photons from $Z \to \ell\ell\gamma$ decays.

10 Summary

The calibration of the energy measurement of electrons and photons collected with the ATLAS detector during 2015 and 2016 using about 36 fb^{-1} of LHC proton−proton collisions at $\sqrt{s} = 13$ TeV is presented. The estimate of the energy is optimized in simulation using variables related to the

2019 JINST 14 P03017

shower development in the calorimeter and the properties of the photon conversions. In the transition region between the barrel and endcap calorimeters, the energy resolution is improved using information provided by gap scintillators.

To achieve good linearity of the energy response, an accurate intercalibration of the different longitudinal layers of the calorimeter is required. The intercalibration of the first two layers of the calorimeter is derived from a study of muon energy deposits. Despite the moderate signal-to-noise ratio for muon energy deposits at the luminosity where the data are collected, an accuracy of 0.7% to 2.5% is achieved for this measurement. The calibration of the presampler layer is derived from a detailed study of electron and photon showers, with an accuracy varying between 1.5% and 3%. The impact of pile-up on the energy measurement is investigated and small effects are corrected.

The overall calorimeter energy scale is set from a large sample of $Z \to ee$ events, comparing the invariant mass distribution in data and simulation. Differences between data and simulation for the energy resolution are derived and energy scale corrections are extracted. The accuracy of the energy scale measurement varies from 0.03% to 0.2% depending on $|\eta|$. The constant term of the energy resolution in the data is less than 1% in the barrel calorimeter and typically 1–2% in the endcap calorimeter.

The calorimeter energy scale is found to be stable with time and with changes in luminosity, with effects of up to few per mille observed in the endcap calorimeter and less than one per mille in the barrel calorimeter.

Uncertainties in the amount and location of material in front of the calorimeter are mostly the same as in the Run 1 studies. The impact of the detector components that were changed before data taking started in 2015 is investigated and small additional uncertainties in the energy response are derived.

Uncertainties in the linearity of the measurement of the energy deposited in each calorimeter readout cell are estimated using data collected with special settings in 2015 and 2017 and found to be at the few per mille level for most of the calorimeter acceptance.

From these measurements, the energy calibration and its total uncertainty are derived for electrons and photons at all energies. The systematic uncertainty in the energy scale calibration is about 0.03% to 0.2% in most of the detector acceptance ($|\eta| < 2.5$) for electrons with transverse momentum close to 45 GeV. For electrons with transverse momentum of 10 GeV the typical uncertainty is 0.3% to 0.8% and it is about 0.25% to 1% for photons with transverse momentum around 60 GeV. This energy calibration was used for the Higgs boson mass measurement performed by the ATLAS Collaboration using the two-photon and four-lepton decay channels with data collected in 2015 and 2016 [40].

The accuracy of this calibration is probed with low-energy electrons from $J/\psi \to ee$ events and with photons from radiative Z boson decays and good agreement is found.

Acknowledgments

We thank CERN for the very successful operation of the LHC, as well as the support staff from our institutions without whom ATLAS could not be operated efficiently.

We acknowledge the support of ANPCyT, Argentina; YerPhI, Armenia; ARC, Australia; BMWFW and FWF, Austria; ANAS, Azerbaijan; SSTC, Belarus; CNPq and FAPESP, Brazil;

2019 JINST 14 P03017

NSERC, NRC and CFI, Canada; CERN; CONICYT, Chile; CAS, MOST and NSFC, China; COLCIENCIAS, Colombia; MSMT CR, MPO CR and VSC CR, Czech Republic; DNRF and DNSRC, Denmark; IN2P3-CNRS, CEA-DRF/IRFU, France; SRNSFG, Georgia; BMBF, HGF, and MPG, Germany; GSRT, Greece; RGC, Hong Kong SAR, China; ISF and Benoziyo Center, Israel; INFN, Italy; MEXT and JSPS, Japan; CNRST, Morocco; NWO, Netherlands; RCN, Norway; MNiSW and NCN, Poland; FCT, Portugal; MNE/IFA, Romania; MES of Russia and NRC KI, Russian Federation; JINR; MESTD, Serbia; MSSR, Slovakia; ARRS and MIZŠ, Slovenia; DST/NRF, South Africa; MINECO, Spain; SRC and Wallenberg Foundation, Sweden; SERI, SNSF and Cantons of Bern and Geneva, Switzerland; MOST, Taiwan; TAEK, Turkey; STFC, United Kingdom; DOE and NSF, United States of America. In addition, individual groups and members have received support from BCKDF, CANARIE, CRC and Compute Canada, Canada; COST, ERC, ERDF, Horizon 2020, and Marie Skłodowska-Curie Actions, European Union; Investissements d' Avenir Labex and Idex, ANR, France; DFG and AvH Foundation, Germany; Herakleitos, Thales and Aristeia programmes co-financed by EU-ESF and the Greek NSRF, Greece; BSF-NSF and GIF, Israel; CERCA Programme Generalitat de Catalunya, Spain; The Royal Society and Leverhulme Trust, United Kingdom.

The crucial computing support from all WLCG partners is acknowledged gratefully, in particular from CERN, the ATLAS Tier-1 facilities at TRIUMF (Canada), NDGF (Denmark, Norway, Sweden), CC-IN2P3 (France), KIT/GridKA (Germany), INFN-CNAF (Italy), NL-T1 (Netherlands), PIC (Spain), ASGC (Taiwan), RAL (U.K.) and BNL (U.S.A.), the Tier-2 facilities worldwide and large non-WLCG resource providers. Major contributors of computing resources are listed in ref. [41].

References

[1] ATLAS collaboration, *Electron and photon energy calibration with the ATLAS detector using LHC Run 1 data*, *Eur. Phys. J.* **C 74** (2014) 3071 [arXiv:1407.5063].

[2] ATLAS collaboration, *The ATLAS experiment at the CERN Large Hadron Collider*, 2008 *JINST* **3** S08003.

[3] ATLAS collaboration, *Performance of the ATLAS Trigger System in 2015*, *Eur. Phys. J.* **C 77** (2017) 317 [arXiv:1611.09661].

[4] H. Abreu et al., *Performance of the electronic readout of the ATLAS liquid argon calorimeters*, 2010 *JINST* **5** P09003.

[5] W.E. Cleland and E.G. Stern, *Signal processing considerations for liquid ionization calorimeters in a high rate environment*, *Nucl. Instrum. Meth.* **A 338** (1994) 467.

[6] M. Aharrouche et al., *Response uniformity of the ATLAS liquid argon electromagnetic calorimeter*, *Nucl. Instrum. Meth.* **A 582** (2007) 429 [arXiv:0709.1094].

[7] W. Lampl et al., *Calorimeter clustering algorithms: description and performance*, ATL-LARG-PUB-2008-002 (2008).

[8] ATLAS collaboration, *Measurement of the photon identification efficiencies with the ATLAS detector using LHC Run 2 data collected in 2015 and 2016*, arXiv:1810.05087.

2019 JINST 14 P03017

[9] ATLAS collaboration, *Topological cell clustering in the ATLAS calorimeters and its performance in LHC Run 1*, *Eur. Phys. J.* **C 77** (2017) 490 [arXiv:1603.02934].

[10] ATLAS collaboration, *Electron reconstruction and identification in the ATLAS experiment using the 2015 and 2016 LHC proton-proton collision data at* $\sqrt{s} = 13$ *TeV*, arXiv:1902.04655.

[11] S. Alioli, P. Nason, C. Oleari and E. Re, *NLO vector-boson production matched with shower in POWHEG*, *JHEP* **07** (2008) 060 [arXiv:0805.4802].

[12] T. Sjöstrand, S. Mrenna and P.Z. Skands, *A brief introduction to PYTHIA 8.1*, *Comput. Phys. Commun.* **178** (2008) 852 [arXiv:0710.3820].

[13] H.-L. Lai et al., *New parton distributions for collider physics*, *Phys. Rev.* **D 82** (2010) 074024 [arXiv:1007.2241].

[14] ATLAS collaboration, *Measurement of the* Z/γ^* *boson transverse momentum distribution in pp collisions at* $\sqrt{s} = 7$ *TeV with the ATLAS detector*, *JHEP* **09** (2014) 145 [arXiv:1406.3660].

[15] J. Pumplin et al., *New generation of parton distributions with uncertainties from global QCD analysis*, *JHEP* **07** (2002) 012 [hep-ph/0201195].

[16] D.J. Lange, *The EvtGen particle decay simulation package*, *Nucl. Instrum. Meth.* **A 462** (2001) 152.

[17] N. Davidson, T. Przedzinski and Z. Was, *PHOTOS interface in C++: technical and physics documentation*, *Comput. Phys. Commun.* **199** (2016) 86 [arXiv:1011.0937].

[18] T. Gleisberg et al., *Event generation with SHERPA 1.1*, *JHEP* **02** (2009) 007 [arXiv:0811.4622].

[19] ATLAS collaboration, *ATLAS Run 1 PYTHIA8 tunes*, ATL-PHYS-PUB-2014-021 (2014).

[20] R.D. Ball et al., *Parton distributions with LHC data*, *Nucl. Phys.* **B 867** (2013) 244 [arXiv:1207.1303].

[21] ATLAS collaboration, *The ATLAS simulation infrastructure*, *Eur. Phys. J.* **C 70** (2010) 823 [arXiv:1005.4568].

[22] GEANT4 collaboration, *GEANT4: a simulation toolkit*, *Nucl. Instrum. Meth.* **A 506** (2003) 250.

[23] ATLAS collaboration, *Summary of ATLAS PYTHIA 8 tunes*, ATL-PHYS-PUB-2012-003 (2012).

[24] A.D. Martin, W.J. Stirling, R.S. Thorne and G. Watt, *Parton distributions for the LHC*, *Eur. Phys. J.* **C 63** (2009) 189 [arXiv:0901.0002].

[25] ATLAS collaboration, *ATLAS insertable b-layer technical design report*, ATLAS-TDR-19 (2010).

[26] ATLAS collaboration, *ATLAS insertable b-layer technical design report addendum*, ATLAS-TDR-ADD-1 (2012).

[27] B. Abbott et al., *Production and integration of the ATLAS insertable B-layer*, 2018 *JINST* **13** T05008 [arXiv:1803.00844].

[28] ATLAS collaboration, *Study of the material of the ATLAS inner detector for Run 2 of the LHC*, 2017 *JINST* **12** P12009 [arXiv:1707.02826].

[29] ATLAS collaboration, *Muon reconstruction performance of the ATLAS detector in proton-proton collision data at* $\sqrt{s} = 13$ *TeV*, *Eur. Phys. J.* **C 76** (2016) 292 [arXiv:1603.05598].

[30] C. de La Taille and L. Serin, *Temperature dependance of the ATLAS electromagnetic calorimeter signal. Preliminary drift time measurement*, ATL-LARG-95-029 (1995).

[31] B. Aubert et al., *Development and construction of large size signal electrodes for the ATLAS electromagnetic calorimeter*, *Nucl. Instrum. Meth.* **A 539** (2005) 558.

2019 JINST 14 P03017

[32] B. Botchev et al., *The high voltage feedthroughs for the ATLAS Liquid Argon Calorimeters*, 2007 *JINST* **2** T10002 [arXiv:0709.0744].

[33] L.S. Miller, S. Howe and W.E. Spear, *Charge transport in solid and liquid Ar, Kr and Xe*, *Phys. Rev.* **166** (1968) 871.

[34] K. Yoshino, U. Sowada and W.F. Schmidt, *Effect of molecular solutes on the electron drift velocity in liquid Ar, Kr and Xe*, *Phys. Rev.* **A 14** (1976) 438.

[35] ATLAS collaboration, *Drift time measurement in the ATLAS liquid argon electromagnetic calorimeter using cosmic muons*, *Eur. Phys. J.* **C 70** (2010) 755 [arXiv:1002.4189].

[36] ATLAS collaboration, *Measurement of the photon identification efficiencies with the ATLAS detector using LHC Run-1 data*, *Eur. Phys. J.* **C 76** (2016) 666 [arXiv:1606.01813].

[37] ATLAS collaboration, *Electron efficiency measurements with the ATLAS detector using 2012 LHC proton-proton collision data*, *Eur. Phys. J.* **C 77** (2017) 195 [arXiv:1612.01456].

[38] M. Aharrouche et al., *Energy linearity and resolution of the ATLAS electromagnetic barrel calorimeter in an electron test-beam*, *Nucl. Instrum. Meth.* **A 568** (2006) 601 [physics/0608012].

[39] ATLAS collaboration, *Measurement of the differential cross-sections of inclusive, prompt and non-prompt J/ψ production in proton-proton collisions at $\sqrt{s} = 7$ TeV*, *Nucl. Phys.* **B 850** (2011) 387 [arXiv:1104.3038].

[40] ATLAS collaboration, *Measurement of the Higgs boson mass in the $H \to ZZ^* \to 4\ell$ and $H \to \gamma\gamma$ channels with $\sqrt{s} = 13$ TeV pp collisions using the ATLAS detector*, *Phys. Lett.* **B 784** (2018) 345 [arXiv:1806.00242].

[41] ATLAS collaboration, *ATLAS computing acknowledgements*, ATL-GEN-PUB-2016-002 (2016).

2019 JINST 14 P03017

The ATLAS collaboration

M. Aaboud[34d], G. Aad[99], B. Abbott[125], D.C. Abbott[100], O. Abdinov[13,*], B. Abeloos[129], D.K. Abhayasinghe[91], S.H. Abidi[164], O.S. AbouZeid[39], N.L. Abraham[153], H. Abramowicz[158], H. Abreu[157], Y. Abulaiti[6], B.S. Acharya[64a,64b,p], S. Adachi[160], L. Adam[97], L. Adamczyk[81a], L. Adamek[164], J. Adelman[119], M. Adersberger[112], A. Adiguzel[12c,ai], T. Adye[141], A.A. Affolder[143], Y. Afik[157], C. Agheorghiesei[27c], J.A. Aguilar-Saavedra[137f,137a,ah], F. Ahmadov[77,af], G. Aielli[71a,71b], S. Akatsuka[83], T.P.A. Åkesson[94], E. Akilli[52], A.V. Akimov[108], G.L. Alberghi[23b,23a], J. Albert[173], P. Albicocco[49], M.J. Alconada Verzini[86], S. Alderweireldt[117], M. Aleksa[35], I.N. Aleksandrov[77], C. Alexa[27b], D. Alexandre[19], T. Alexopoulos[10], M. Alhroob[125], B. Ali[139], G. Alimonti[66a], J. Alison[36], S.P. Alkire[145], C. Allaire[129], B.M.M. Allbrooke[153], B.W. Allen[128], P.P. Allport[21], A. Aloisio[67a,67b], A. Alonso[39], F. Alonso[86], C. Alpigiani[145], A.A. Alshehri[55], M.I. Alstaty[99], B. Alvarez Gonzalez[35], D. Álvarez Piqueras[171], M.G. Alviggi[67a,67b], B.T. Amadio[18], Y. Amaral Coutinho[78b], A. Ambler[101], L. Ambroz[132], C. Amelung[26], D. Amidei[103], S.P. Amor Dos Santos[137a,137c], S. Amoroso[44], C.S. Amrouche[52], F. An[76], C. Anastopoulos[146], L.S. Ancu[52], N. Andari[142], T. Andeen[11], C.F. Anders[59b], J.K. Anders[20], K.J. Anderson[36], A. Andreazza[66a,66b], V. Andrei[59a], C.R. Anelli[173], S. Angelidakis[37], I. Angelozzi[118], A. Angerami[38], A.V. Anisenkov[120b,120a], A. Annovi[69a], C. Antel[59a], M.T. Anthony[146], M. Antonelli[49], D.J.A. Antrim[168], F. Anulli[70a], M. Aoki[79], J.A. Aparisi Pozo[171], L. Aperio Bella[35], G. Arabidze[104], J.P. Araque[137a], V. Araujo Ferraz[78b], R. Araujo Pereira[78b], A.T.H. Arce[47], R.E. Ardell[91], F.A. Arduh[86], J-F. Arguin[107], S. Argyropoulos[75], J.-H. Arling[44], A.J. Armbruster[35], L.J. Armitage[90], A. Armstrong[168], O. Arnaez[164], H. Arnold[118], M. Arratia[31], O. Arslan[24], A. Artamonov[109,*], G. Artoni[132], S. Artz[97], S. Asai[160], N. Asbah[57], E.M. Asimakopoulou[169], L. Asquith[153], K. Assamagan[29], R. Astalos[28a], R.J. Atkin[32a], M. Atkinson[170], N.B. Atlay[148], H. Atmani[129], K. Augsten[139], G. Avolio[35], R. Avramidou[58a], M.K. Ayoub[15a], A.M. Azoulay[165b], G. Azuelos[107,av], A.E. Baas[59a], M.J. Baca[21], H. Bachacou[142], K. Bachas[65a,65b], M. Backes[132], P. Bagnaia[70a,70b], M. Bahmani[82], H. Bahrasemani[149], A.J. Bailey[171], V.R. Bailey[170], J.T. Baines[141], M. Bajic[39], C. Bakalis[10], O.K. Baker[180], P.J. Bakker[118], D. Bakshi Gupta[8], S. Balaji[154], E.M. Baldin[120b,120a], P. Balek[177], F. Balli[142], W.K. Balunas[134], J. Balz[97], E. Banas[82], A. Bandyopadhyay[24], S. Banerjee[178,l], A.A.E. Bannoura[179], L. Barak[158], W.M. Barbe[37], E.L. Barberio[102], D. Barberis[53b,53a], M. Barbero[99], T. Barillari[113], M-S. Barisits[35], J. Barkeloo[128], T. Barklow[150], R. Barnea[157], S.L. Barnes[58c], B.M. Barnett[141], R.M. Barnett[18], Z. Barnovska-Blenessy[58a], A. Baroncelli[72a], G. Barone[29], A.J. Barr[132], L. Barranco Navarro[171], F. Barreiro[96], J. Barreiro Guimarães da Costa[15a], R. Bartoldus[150], A.E. Barton[87], P. Bartos[28a], A. Basalaev[135], A. Bassalat[129], R.L. Bates[55], S.J. Batista[164], S. Batlamous[34e], J.R. Batley[31], M. Battaglia[143], M. Bauce[70a,70b], F. Bauer[142], K.T. Bauer[168], H.S. Bawa[150], J.B. Beacham[123], T. Beau[133], P.H. Beauchemin[167], P. Bechtle[24], H.C. Beck[51], H.P. Beck[20,s], K. Becker[50], M. Becker[97], C. Becot[44], A. Beddall[12d], A.J. Beddall[12a], V.A. Bednyakov[77], M. Bedognetti[118], C.P. Bee[152], T.A. Beermann[74], M. Begalli[78b], M. Begel[29], A. Behera[152], J.K. Behr[44], F. Beisiegel[24], A.S. Bell[92], G. Bella[158], L. Bellagamba[23b], A. Bellerive[33], M. Bellomo[157], P. Bellos[9], K. Belotskiy[110], N.L. Belyaev[110], O. Benary[158,*], D. Benchekroun[34a], M. Bender[112], N. Benekos[10], Y. Benhammou[158], E. Benhar Noccioli[180], J. Benitez[75], D.P. Benjamin[6], M. Benoit[52], J.R. Bensinger[26], S. Bentvelsen[118], L. Beresford[132], M. Beretta[49], D. Berge[44], E. Bergeaas Kuutmann[169], N. Berger[5], B. Bergmann[139], L.J. Bergsten[26], J. Beringer[18], S. Berlendis[7], N.R. Bernard[100], G. Bernardi[133], C. Bernius[150], F.U. Bernlochner[24], T. Berry[91], P. Berta[97], C. Bertella[15a], G. Bertoli[43a,43b], I.A. Bertram[87], G.J. Besjes[39], O. Bessidskaia Bylund[179], M. Bessner[44], N. Besson[142], A. Bethani[98], S. Bethke[113], A. Betti[24], A.J. Bevan[90], J. Beyer[113], R. Bi[136], R.M. Bianchi[136], O. Biebel[112], D. Biedermann[19], R. Bielski[35], K. Bierwagen[97], N.V. Biesuz[69a,69b], M. Biglietti[72a], T.R.V. Billoud[107], M. Bindi[51], A. Bingul[12d], C. Bini[70a,70b], S. Biondi[23b,23a], M. Birman[177], T. Bisanz[51], J.P. Biswal[158], C. Bittrich[46], D.M. Bjergaard[47], J.E. Black[150], K.M. Black[25], T. Blazek[28a], I. Bloch[44], C. Blocker[26], A. Blue[55], U. Blumenschein[90], Dr. Blunier[144a], G.J. Bobbink[118], V.S. Bobrovnikov[120b,120a], S.S. Bocchetta[94], A. Bocci[47], D. Boerner[179], D. Bogavac[112],

2019 JINST 14 P03017

A.G. Bogdanchikov[120b,120a], C. Bohm[43a], V. Boisvert[91], P. Bokan[51,169], T. Bold[81a], A.S. Boldyrev[111], A.E. Bolz[59b], M. Bomben[133], M. Bona[90], J.S. Bonilla[128], M. Boonekamp[142], H.M. Borecka-Bielska[88], A. Borisov[121], G. Borissov[87], J. Bortfeldt[35], D. Bortoletto[132], V. Bortolotto[71a,71b], D. Boscherini[23b], M. Bosman[14], J.D. Bossio Sola[30], K. Bouaouda[34a], J. Boudreau[136], E.V. Bouhova-Thacker[87], D. Boumediene[37], C. Bourdarios[129], S.K. Boutle[55], A. Boveia[123], J. Boyd[35], D. Boye[32b], I.R. Boyko[77], A.J. Bozson[91], J. Bracinik[21], N. Brahimi[99], A. Brandt[8], G. Brandt[179], O. Brandt[59a], F. Braren[44], U. Bratzler[161], B. Brau[100], J.E. Brau[128], W.D. Breaden Madden[55], K. Brendlinger[44], L. Brenner[44], R. Brenner[169], S. Bressler[177], B. Brickwedde[97], D.L. Briglin[21], D. Britton[55], D. Britzger[113], I. Brock[24], R. Brock[104], G. Brooijmans[38], T. Brooks[91], W.K. Brooks[144b], E. Brost[119], J.H Broughton[21], P.A. Bruckman de Renstrom[82], D. Bruncko[28b], A. Bruni[23b], G. Bruni[23b], L.S. Bruni[118], S. Bruno[71a,71b], B.H. Brunt[31], M. Bruschi[23b], N. Bruscino[136], P. Bryant[36], L. Bryngemark[94], T. Buanes[17], Q. Buat[35], P. Buchholz[148], A.G. Buckley[55], I.A. Budagov[77], M.K. Bugge[131], F. Bührer[50], O. Bulekov[110], D. Bullock[8], T.J. Burch[119], S. Burdin[88], C.D. Burgard[118], A.M. Burger[5], B. Burghgrave[119], K. Burka[82], S. Burke[141], I. Burmeister[45], J.T.P. Burr[132], V. Büscher[97], E. Buschmann[51], P. Bussey[55], J.M. Butler[25], C.M. Buttar[55], J.M. Butterworth[92], P. Butti[35], W. Buttinger[35], A. Buzatu[155], A.R. Buzykaev[120b,120a], G. Cabras[23b,23a], S. Cabrera Urbán[171], D. Caforio[139], H. Cai[170], V.M.M. Cairo[2], O. Cakir[4a], N. Calace[35], P. Calafiura[18], A. Calandri[99], G. Calderini[133], P. Calfayan[63], G. Callea[55], L.P. Caloba[78b], S. Calvente Lopez[96], D. Calvet[37], S. Calvet[37], T.P. Calvet[152], M. Calvetti[69a,69b], R. Camacho Toro[133], S. Camarda[35], D. Camarero Munoz[96], P. Camarri[71a,71b], D. Cameron[131], R. Caminal Armadans[100], C. Camincher[35], S. Campana[35], M. Campanelli[92], A. Camplani[39], A. Campoverde[148], V. Canale[67a,67b], M. Cano Bret[58c], J. Cantero[126], T. Cao[158], Y. Cao[170], M.D.M. Capeans Garrido[35], I. Caprini[27b], M. Caprini[27b], M. Capua[40b,40a], R.M. Carbone[38], R. Cardarelli[71a], F.C. Cardillo[146], I. Carli[140], T. Carli[35], G. Carlino[67a], B.T. Carlson[136], L. Carminati[66a,66b], R.M.D. Carney[43a,43b], S. Caron[117], E. Carquin[144b], S. Carrá[66a,66b], J.W.S. Carter[164], D. Casadei[32b], M.P. Casado[14,g], A.F. Casha[164], D.W. Casper[168], R. Castelijn[118], F.L. Castillo[171], V. Castillo Gimenez[171], N.F. Castro[137a,137e], A. Catinaccio[35], J.R. Catmore[131], A. Cattai[35], J. Caudron[24], V. Cavaliere[29], E. Cavallaro[14], D. Cavalli[66a], M. Cavalli-Sforza[14], V. Cavasinni[69a,69b], E. Celebi[12b], F. Ceradini[72a,72b], L. Cerda Alberich[171], A.S. Cerqueira[78a], A. Cerri[153], L. Cerrito[71a,71b], F. Cerutti[18], A. Cervelli[23b,23a], S.A. Cetin[12b], A. Chafaq[34a], D. Chakraborty[119], S.K. Chan[57], W.S. Chan[118], W.Y. Chan[88], J.D. Chapman[31], B. Chargeishvili[156b], D.G. Charlton[21], C.C. Chau[33], C.A. Chavez Barajas[153], S. Che[123], A. Chegwidden[104], S. Chekanov[6], S.V. Chekulaev[165a], G.A. Chelkov[77,au], M.A. Chelstowska[35], B. Chen[76], C. Chen[58a], C.H. Chen[76], H. Chen[29], J. Chen[58a], J. Chen[38], S. Chen[134], S.J. Chen[15c], X. Chen[15b,at], Y. Chen[80], Y-H. Chen[44], H.C. Cheng[61a], H.J. Cheng[15d], A. Cheplakov[77], E. Cheremushkina[121], R. Cherkaoui El Moursli[34e], E. Cheu[7], K. Cheung[62], T.J.A. Chevalérias[142], L. Chevalier[142], V. Chiarella[49], G. Chiarelli[69a], G. Chiodini[65a], A.S. Chisholm[35,21], A. Chitan[27b], I. Chiu[160], Y.H. Chiu[173], M.V. Chizhov[77], K. Choi[63], A.R. Chomont[129], S. Chouridou[159], Y.S. Chow[118], V. Christodoulou[92], M.C. Chu[61a], J. Chudoba[138], A.J. Chuinard[101], J.J. Chwastowski[82], L. Chytka[127], D. Cinca[45], V. Cindro[89], I.A. Cioară[24], A. Ciocio[18], F. Cirotto[67a,67b], Z.H. Citron[177], M. Citterio[66a], A. Clark[52], M.R. Clark[38], P.J. Clark[48], C. Clement[43a,43b], Y. Coadou[99], M. Cobal[64a,64c], A. Coccaro[53b,53a], J. Cochran[76], H. Cohen[158], A.E.C. Coimbra[177], L. Colasurdo[117], B. Cole[38], A.P. Colijn[118], J. Collot[56], P. Conde Muiño[137a,i], E. Coniavitis[50], S.H. Connell[32b], I.A. Connelly[98], S. Constantinescu[27b], F. Conventi[67a,aw], A.M. Cooper-Sarkar[132], F. Cormier[172], K.J.R. Cormier[164], L.D. Corpe[92], M. Corradi[70a,70b], E.E. Corrigan[94], F. Corriveau[101,ad], A. Cortes-Gonzalez[35], M.J. Costa[171], F. Costanza[5], D. Costanzo[146], G. Cottin[31], G. Cowan[91], J.W. Cowley[31], B.E. Cox[98], J. Crane[98], K. Cranmer[122], S.J. Crawley[55], R.A. Creager[134], G. Cree[33], S. Crépé-Renaudin[56], F. Crescioli[133], M. Cristinziani[24], V. Croft[122], G. Crosetti[40b,40a], A. Cueto[96], T. Cuhadar Donszelmann[146], A.R. Cukierman[150], S. Czekierda[82], P. Czodrowski[35], M.J. Da Cunha Sargedas De Sousa[58b], C. Da Via[98], W. Dabrowski[81a], T. Dado[28a,y], S. Dahbi[34e], T. Dai[103], F. Dallaire[107], C. Dallapiccola[100], M. Dam[39], G. D'amen[23b,23a], J. Damp[97], J.R. Dandoy[134], M.F. Daneri[30], N.P. Dang[178,1], N.D Dann[98], M. Danninger[172],

2019 JINST 14 P03017

V. Dao[35], G. Darbo[53b], S. Darmora[8], O. Dartsi[5], A. Dattagupta[128], T. Daubney[44], S. D'Auria[66a,66b], W. Davey[24], C. David[44], T. Davidek[140], D.R. Davis[47], E. Dawe[102], I. Dawson[146], K. De[8], R. De Asmundis[67a], A. De Benedetti[125], M. De Beurs[118], S. De Castro[23b,23a], S. De Cecco[70a,70b], N. De Groot[117], P. de Jong[118], H. De la Torre[104], F. De Lorenzi[76], A. De Maria[69a,69b], D. De Pedis[70a], A. De Salvo[70a], U. De Sanctis[71a,71b], M. De Santis[71a,71b], A. De Santo[153], K. De Vasconcelos Corga[99], J.B. De Vivie De Regie[129], C. Debenedetti[143], D.V. Dedovich[77], N. Dehghanian[3], M. Del Gaudio[40b,40a], J. Del Peso[96], Y. Delabat Diaz[44], D. Delgove[129], F. Deliot[142], C.M. Delitzsch[7], M. Della Pietra[67a,67b], D. Della Volpe[52], A. Dell'Acqua[35], L. Dell'Asta[25], M. Delmastro[5], C. Delporte[129], P.A. Delsart[56], D.A. DeMarco[164], S. Demers[180], M. Demichev[77], S.P. Denisov[121], D. Denysiuk[118], L. D'Eramo[133], D. Derendarz[82], J.E. Derkaoui[34d], F. Derue[133], P. Dervan[88], K. Desch[24], C. Deterre[44], K. Dette[164], M.R. Devesa[30], P.O. Deviveiros[35], A. Dewhurst[141], S. Dhaliwal[26], F.A. Di Bello[52], A. Di Ciaccio[71a,71b], L. Di Ciaccio[5], W.K. Di Clemente[134], C. Di Donato[67a,67b], A. Di Girolamo[35], G. Di Gregorio[69a,69b], B. Di Micco[72a,72b], R. Di Nardo[100], K.F. Di Petrillo[57], R. Di Sipio[164], D. Di Valentino[33], C. Diaconu[99], M. Diamond[164], F.A. Dias[39], T. Dias Do Vale[137a], M.A. Diaz[144a], J. Dickinson[18], E.B. Diehl[103], J. Dietrich[19], S. Díez Cornell[44], A. Dimitrievska[18], J. Dingfelder[24], F. Dittus[35], F. Djama[99], T. Djobava[156b], J.I. Djuvsland[17], M.A.B. Do Vale[78c], M. Dobre[27b], D. Dodsworth[26], C. Doglioni[94], J. Dolejsi[140], Z. Dolezal[140], M. Donadelli[78d], J. Donini[37], A. D'onofrio[90], M. D'Onofrio[88], J. Dopke[141], A. Doria[67a], M.T. Dova[86], A.T. Doyle[55], E. Drechsler[149], E. Dreyer[149], T. Dreyer[51], Y. Du[58b], F. Dubinin[108], M. Dubovsky[28a], A. Dubreuil[52], E. Duchovni[177], G. Duckeck[112], A. Ducourthial[133], O.A. Ducu[107,x], D. Duda[113], A. Dudarev[35], A.C. Dudder[97], E.M. Duffield[18], L. Duflot[129], M. Dührssen[35], C. Dülsen[179], M. Dumancic[177], A.E. Dumitriu[27b,e], A.K. Duncan[55], M. Dunford[59a], A. Duperrin[99], H. Duran Yildiz[4a], M. Düren[54], A. Durglishvili[156b], D. Duschinger[46], B. Dutta[44], D. Duvnjak[1], M. Dyndal[44], S. Dysch[98], B.S. Dziedzic[82], K.M. Ecker[113], R.C. Edgar[103], T. Eifert[35], G. Eigen[17], K. Einsweiler[18], T. Ekelof[169], M. El Kacimi[34c], R. El Kosseifi[99], V. Ellajosyula[99], M. Ellert[169], F. Ellinghaus[179], A.A. Elliot[90], N. Ellis[35], J. Elmsheuser[29], M. Elsing[35], D. Emeliyanov[141], A. Emerman[38], Y. Enari[160], J.S. Ennis[175], M.B. Epland[47], J. Erdmann[45], A. Ereditato[20], S. Errede[170], M. Escalier[129], C. Escobar[171], O. Estrada Pastor[171], A.I. Etienvre[142], E. Etzion[158], H. Evans[63], A. Ezhilov[135], M. Ezzi[34e], F. Fabbri[55], L. Fabbri[23b,23a], V. Fabiani[117], G. Facini[92], R.M. Faisca Rodrigues Pereira[137a], R.M. Fakhrutdinov[121], S. Falciano[70a], P.J. Falke[5], S. Falke[5], J. Faltova[140], Y. Fang[15a], M. Fanti[66a,66b], A. Farbin[8], A. Farilla[72a], E.M. Farina[68a,68b], T. Farooque[104], S. Farrell[18], S.M. Farrington[175], P. Farthouat[35], F. Fassi[34e], P. Fassnacht[35], D. Fassouliotis[9], M. Faucci Giannelli[48], W.J. Fawcett[31], L. Fayard[129], O.L. Fedin[135,q], W. Fedorko[172], M. Feickert[41], S. Feigl[131], L. Feligioni[99], C. Feng[58b], E.J. Feng[35], M. Feng[47], M.J. Fenton[55], A.B. Fenyuk[121], J. Ferrando[44], A. Ferrari[169], P. Ferrari[118], R. Ferrari[68a], D.E. Ferreira de Lima[59b], A. Ferrer[171], D. Ferrere[52], C. Ferretti[103], F. Fiedler[97], A. Filipčič[89], F. Filthaut[117], K.D. Finelli[25], M.C.N. Fiolhais[137a,137c,a], L. Fiorini[171], C. Fischer[14], W.C. Fisher[104], N. Flaschel[44], I. Fleck[148], P. Fleischmann[103], R.R.M. Fletcher[134], T. Flick[179], B.M. Flierl[112], L.M. Flores[134], L.R. Flores Castillo[61a], F.M. Follega[73a,73b], N. Fomin[17], G.T. Forcolin[73a,73b], A. Formica[142], F.A. Förster[14], A.C. Forti[98], A.G. Foster[21], D. Fournier[129], H. Fox[87], S. Fracchia[146], P. Francavilla[69a,69b], M. Franchini[23b,23a], S. Franchino[59a], D. Francis[35], L. Franconi[143], M. Franklin[57], M. Frate[168], A.N. Fray[90], D. Freeborn[92], B. Freund[107], W.S. Freund[78b], E.M. Freundlich[45], D.C. Frizzell[125], D. Froidevaux[35], J.A. Frost[132], C. Fukunaga[161], E. Fullana Torregrosa[171], E. Fumagalli[53b,53a], T. Fusayasu[114], J. Fuster[171], O. Gabizon[157], A. Gabrielli[23b,23a], A. Gabrielli[18], G.P. Gach[81a], S. Gadatsch[52], P. Gadow[113], G. Gagliardi[53b,53a], L.G. Gagnon[107], C. Galea[27b], B. Galhardo[137a,137c], E.J. Gallas[132], B.J. Gallop[141], P. Gallus[139], G. Galster[39], R. Gamboa Goni[90], K.K. Gan[123], S. Ganguly[177], J. Gao[58a], Y. Gao[88], Y.S. Gao[150,n], C. García[171], J.E. García Navarro[171], J.A. García Pascual[15a], C. Garcia-Argos[50], M. Garcia-Sciveres[18], R.W. Gardner[36], N. Garelli[150], S. Gargiulo[50], V. Garonne[131], K. Gasnikova[44], A. Gaudiello[53b,53a], G. Gaudio[68a], I.L. Gavrilenko[108], A. Gavrilyuk[109], C. Gay[172], G. Gaycken[24], E.N. Gazis[10], C.N.P. Gee[141], J. Geisen[51], M. Geisen[97], M.P. Geisler[59a], C. Gemme[53b], M.H. Genest[56], C. Geng[103], S. Gentile[70a,70b], S. George[91],

2019 JINST 14 P03017

D. Gerbaudo[14], G. Gessner[45], S. Ghasemi[148], M. Ghasemi Bostanabad[173], M. Ghneimat[24], B. Giacobbe[23b], S. Giagu[70a,70b], N. Giangiacomi[23b,23a], P. Giannetti[69a], A. Giannini[67a,67b], S.M. Gibson[91], M. Gignac[143], D. Gillberg[33], G. Gilles[179], D.M. Gingrich[3,av], M.P. Giordani[64a,64c], F.M. Giorgi[23b], P.F. Giraud[142], P. Giromini[57], G. Giugliarelli[64a,64c], D. Giugni[66a], F. Giuli[132], M. Giulini[59b], S. Gkaitatzis[159], I. Gkialas[9,k], E.L. Gkougkousis[14], P. Gkountoumis[10], L.K. Gladilin[111], C. Glasman[96], J. Glatzer[14], P.C.F. Glaysher[44], A. Glazov[44], M. Goblirsch-Kolb[26], J. Godlewski[82], S. Goldfarb[102], T. Golling[52], D. Golubkov[121], A. Gomes[137a,137b], R. Goncalves Gama[51], R. Gonçalo[137a], G. Gonella[50], L. Gonella[21], A. Gongadze[77], F. Gonnella[21], J.L. Gonski[57], S. González de la Hoz[171], S. Gonzalez-Sevilla[52], L. Goossens[35], P.A. Gorbounov[109], H.A. Gordon[29], B. Gorini[35], E. Gorini[65a,65b], A. Gorišek[89], A.T. Goshaw[47], C. Gössling[45], M.I. Gostkin[77], C.A. Gottardo[24], C.R. Goudet[129], D. Goujdami[34c], A.G. Goussiou[145], N. Govender[32b,c], C. Goy[5], E. Gozani[157], I. Grabowska-Bold[81a], P.O.J. Gradin[169], E.C. Graham[88], J. Gramling[168], E. Gramstad[131], S. Grancagnolo[19], V. Gratchev[135], P.M. Gravila[27f], F.G. Gravili[65a,65b], C. Gray[55], H.M. Gray[18], Z.D. Greenwood[93,al], C. Grefe[24], K. Gregersen[94], I.M. Gregor[44], P. Grenier[150], K. Grevtsov[44], N.A. Grieser[125], J. Griffiths[8], A.A. Grillo[143], K. Grimm[150,b], S. Grinstein[14,z], Ph. Gris[37], J.-F. Grivaz[129], S. Groh[97], E. Gross[177], J. Grosse-Knetter[51], G.C. Grossi[93], Z.J. Grout[92], C. Grud[103], A. Grummer[116], L. Guan[103], W. Guan[178], J. Guenther[35], A. Guerguichon[129], F. Guescini[165a], D. Guest[168], R. Gugel[50], B. Gui[123], T. Guillemin[5], S. Guindon[35], U. Gul[55], J. Guo[58c], W. Guo[103], Y. Guo[58a,t], Z. Guo[99], R. Gupta[44], S. Gurbuz[12c], G. Gustavino[125], P. Gutierrez[125], C. Gutschow[92], C. Guyot[142], M.P. Guzik[81a], C. Gwenlan[132], C.B. Gwilliam[88], A. Haas[122], C. Haber[18], H.K. Hadavand[8], N. Haddad[34e], A. Hadef[58a], S. Hageböck[24], M. Hagihara[166], M. Haleem[174], J. Haley[126], G. Halladjian[104], G.D. Hallewell[99], K. Hamacher[179], P. Hamal[127], K. Hamano[173], A. Hamilton[32a], G.N. Hamity[146], K. Han[58a,ak], L. Han[58a], S. Han[15d], K. Hanagaki[79,v], M. Hance[143], D.M. Handl[112], B. Haney[134], R. Hankache[133], P. Hanke[59a], E. Hansen[94], J.B. Hansen[39], J.D. Hansen[39], M.C. Hansen[24], P.H. Hansen[39], K. Hara[166], A.S. Hard[178], T. Harenberg[179], S. Harkusha[105], P.F. Harrison[175], N.M. Hartmann[112], Y. Hasegawa[147], A. Hasib[48], S. Hassani[142], S. Haug[20], R. Hauser[104], L. Hauswald[46], L.B. Havener[38], M. Havranek[139], C.M. Hawkes[21], R.J. Hawkings[35], D. Hayden[104], C. Hayes[152], C.P. Hays[132], J.M. Hays[90], H.S. Hayward[88], S.J. Haywood[141], F. He[58a], M.P. Heath[48], V. Hedberg[94], L. Heelan[8], S. Heer[24], K.K. Heidegger[50], J. Heilman[33], S. Heim[44], T. Heim[18], B. Heinemann[44,aq], J.J. Heinrich[112], L. Heinrich[122], C. Heinz[54], J. Hejbal[138], L. Helary[35], A. Held[172], S. Hellesund[131], C.M. Helling[143], S. Hellman[43a,43b], C. Helsens[35], R.C.W. Henderson[87], Y. Heng[178], S. Henkelmann[172], A.M. Henriques Correia[35], G.H. Herbert[19], H. Herde[26], V. Herget[174], Y. Hernández Jiménez[32c], H. Herr[97], M.G. Herrmann[112], T. Herrmann[46], G. Herten[50], R. Hertenberger[112], L. Hervas[35], T.C. Herwig[134], G.G. Hesketh[92], N.P. Hessey[165a], A. Higashida[160], S. Higashino[79], E. Higón-Rodriguez[171], K. Hildebrand[36], E. Hill[173], J.C. Hill[31], K.K. Hill[29], K.H. Hiller[44], S.J. Hillier[21], M. Hils[46], I. Hinchliffe[18], F. Hinterkeuser[24], M. Hirose[130], D. Hirschbuehl[179], B. Hiti[89], O. Hladik[138], D.R. Hlaluku[32c], X. Hoad[48], J. Hobbs[152], N. Hod[165a], M.C. Hodgkinson[146], A. Hoecker[35], M.R. Hoeferkamp[116], F. Hoenig[112], D. Hohn[50], D. Hohov[129], T.R. Holmes[36], M. Holzbock[112], M. Homann[45], B.H. Hommels[31], S. Honda[166], T. Honda[79], T.M. Hong[136], A. Hönle[113], B.H. Hooberman[170], W.H. Hopkins[128], Y. Horii[115], P. Horn[46], A.J. Horton[149], L.A. Horyn[36], J-Y. Hostachy[56], A. Hostiuc[145], S. Hou[155], A. Hoummada[34a], J. Howarth[98], J. Hoya[86], M. Hrabovsky[127], I. Hristova[19], J. Hrivnac[129], A. Hrynevich[106], T. Hryn'ova[5], P.J. Hsu[62], S.-C. Hsu[145], Q. Hu[29], S. Hu[58c], Y. Huang[15a], Z. Hubacek[139], F. Hubaut[99], M. Huebner[24], F. Huegging[24], T.B. Huffman[132], M. Huhtinen[35], R.F.H. Hunter[33], P. Huo[152], A.M. Hupe[33], N. Huseynov[77,af], J. Huston[104], J. Huth[57], R. Hyneman[103], G. Iacobucci[52], G. Iakovidis[29], I. Ibragimov[148], L. Iconomidou-Fayard[129], Z. Idrissi[34e], P. Iengo[35], R. Ignazzi[39], O. Igonkina[118,ab], R. Iguchi[160], T. Iizawa[52], Y. Ikegami[79], M. Ikeno[79], D. Iliadis[159], N. Ilic[117], F. Iltzsche[46], G. Introzzi[68a,68b], M. Iodice[72a], K. Iordanidou[38], V. Ippolito[70a,70b], M.F. Isacson[169], N. Ishijima[130], M. Ishino[160], M. Ishitsuka[162], W. Islam[126], C. Issever[132], S. Istin[157], F. Ito[166], J.M. Iturbe Ponce[61a], R. Iuppa[73a,73b], A. Ivina[177], H. Iwasaki[79], J.M. Izen[42], V. Izzo[67a], P. Jacka[138], P. Jackson[1], R.M. Jacobs[24], V. Jain[2], G. Jäkel[179], K.B. Jakobi[97], K. Jakobs[50], S. Jakobsen[74], T. Jakoubek[138],

2019 JINST 14 P03017

D.O. Jamin[126], R. Jansky[52], J. Janssen[24], M. Janus[51], P.A. Janus[81a], G. Jarlskog[94], N. Javadov[77,af], T. Javůrek[35], M. Javurkova[50], F. Jeanneau[142], L. Jeanty[18], J. Jejelava[156a,ag], A. Jelinskas[175], P. Jenni[50,d], J. Jeong[44], N. Jeong[44], S. Jézéquel[5], H. Ji[178], J. Jia[152], H. Jiang[76], Y. Jiang[58a], Z. Jiang[150,r], S. Jiggins[50], F.A. Jimenez Morales[37], J. Jimenez Pena[171], S. Jin[15c], A. Jinaru[27b], O. Jinnouchi[162], H. Jivan[32c], P. Johansson[146], K.A. Johns[7], C.A. Johnson[63], K. Jon-And[43a,43b], R.W.L. Jones[87], S.D. Jones[153], S. Jones[7], T.J. Jones[88], J. Jongmanns[59a], P.M. Jorge[137a,137b], J. Jovicevic[165a], X. Ju[18], J.J. Junggeburth[113], A. Juste Rozas[14,z], A. Kaczmarska[82], M. Kado[129], H. Kagan[123], M. Kagan[150], T. Kaji[176], E. Kajomovitz[157], C.W. Kalderon[94], A. Kaluza[97], S. Kama[41], A. Kamenshchikov[121], L. Kanjir[89], Y. Kano[160], V.A. Kantserov[110], J. Kanzaki[79], L.S. Kaplan[178], D. Kar[32c], M.J. Kareem[165b], E. Karentzos[10], S.N. Karpov[77], Z.M. Karpova[77], V. Kartvelishvili[87], A.N. Karyukhin[121], L. Kashif[178], R.D. Kass[123], A. Kastanas[43a,43b], Y. Kataoka[160], C. Kato[58d,58c], J. Katzy[44], K. Kawade[80], K. Kawagoe[85], T. Kawaguchi[115], T. Kawamoto[160], G. Kawamura[51], E.F. Kay[88], V.F. Kazanin[120b,120a], R. Keeler[173], R. Kehoe[41], J.S. Keller[33], E. Kellermann[94], J.J. Kempster[21], J. Kendrick[21], O. Kepka[138], S. Kersten[179], B.P. Kerševan[89], S. Ketabchi Haghighat[164], R.A. Keyes[101], M. Khader[170], F. Khalil-Zada[13], A. Khanov[126], A.G. Kharlamov[120b,120a], T. Kharlamova[120b,120a], E.E. Khoda[172], A. Khodinov[163], T.J. Khoo[52], E. Khramov[77], J. Khubua[156b], S. Kido[80], M. Kiehn[52], C.R. Kilby[91], Y.K. Kim[36], N. Kimura[64a,64c], O.M. Kind[19], B.T. King[88], D. Kirchmeier[46], J. Kirk[141], A.E. Kiryunin[113], T. Kishimoto[160], D. Kisielewska[81a], V. Kitali[44], O. Kivernyk[5], E. Kladiva[28b,*], T. Klapdor-Kleingrothaus[50], M.H. Klein[103], M. Klein[88], U. Klein[88], K. Kleinknecht[97], P. Klimek[119], A. Klimentov[29], T. Klingl[24], T. Klioutchnikova[35], F.F. Klitzner[112], P. Kluit[118], S. Kluth[113], E. Kneringer[74], E.B.F.G. Knoops[99], A. Knue[50], A. Kobayashi[160], D. Kobayashi[85], T. Kobayashi[160], M. Kobel[46], M. Kocian[150], P. Kodys[140], P.T. Koenig[24], T. Koffas[33], E. Koffeman[118], N.M. Köhler[113], T. Koi[150], M. Kolb[59b], I. Koletsou[5], T. Kondo[79], N. Kondrashova[58c], K. Köneke[50], A.C. König[117], T. Kono[79], R. Konoplich[122,an], V. Konstantinides[92], N. Konstantinidis[92], B. Konya[94], R. Kopeliansky[63], S. Koperny[81a], K. Korcyl[82], K. Kordas[159], G. Koren[158], A. Korn[92], I. Korolkov[14], E.V. Korolkova[146], N. Korotkova[111], O. Kortner[113], S. Kortner[113], T. Kosek[140], V.V. Kostyukhin[24], A. Kotwal[47], A. Koulouris[10], A. Kourkoumeli-Charalampidi[68a,68b], C. Kourkoumelis[9], E. Kourlitis[146], V. Kouskoura[29], A.B. Kowalewska[82], R. Kowalewski[173], T.Z. Kowalski[81a], C. Kozakai[160], W. Kozanecki[142], A.S. Kozhin[121], V.A. Kramarenko[111], G. Kramberger[89], D. Krasnopevtsev[58a], M.W. Krasny[133], A. Krasznahorkay[35], D. Krauss[113], J.A. Kremer[81a], J. Kretzschmar[88], P. Krieger[164], K. Krizka[18], K. Kroeninger[45], H. Kroha[113], J. Kroll[138], J. Kroll[134], J. Krstic[16], U. Kruchonak[77], H. Krüger[24], N. Krumnack[76], M.C. Kruse[47], T. Kubota[102], S. Kuday[4b], J.T. Kuechler[179], S. Kuehn[35], A. Kugel[59a], T. Kuhl[44], V. Kukhtin[77], R. Kukla[99], Y. Kulchitsky[105,aj], S. Kuleshov[144b], Y.P. Kulinich[170], M. Kuna[56], T. Kunigo[83], A. Kupco[138], T. Kupfer[45], O. Kuprash[158], H. Kurashige[80], L.L. Kurchaninov[165a], Y.A. Kurochkin[105], A. Kurova[110], M.G. Kurth[15d], E.S. Kuwertz[35], M. Kuze[162], J. Kvita[127], T. Kwan[101], A. La Rosa[113], J.L. La Rosa Navarro[78d], L. La Rotonda[40b,40a], F. La Ruffa[40b,40a], C. Lacasta[171], F. Lacava[70a,70b], J. Lacey[44], D.P.J. Lack[98], H. Lacker[19], D. Lacour[133], E. Ladygin[77], R. Lafaye[5], B. Laforge[133], T. Lagouri[32c], S. Lai[51], S. Lammers[63], W. Lampl[7], E. Lançon[29], U. Landgraf[50], M.P.J. Landon[90], M.C. Lanfermann[52], V.S. Lang[44], J.C. Lange[51], R.J. Langenberg[35], A.J. Lankford[168], F. Lanni[29], K. Lantzsch[24], A. Lanza[68a], A. Lapertosa[53b,53a], S. Laplace[133], J.F. Laporte[142], T. Lari[66a], F. Lasagni Manghi[23b,23a], M. Lassnig[35], T.S. Lau[61a], A. Laudrain[129], M. Lavorgna[67a,67b], M. Lazzaroni[66a,66b], B. Le[102], O. Le Dortz[133], E. Le Guirriec[99], E.P. Le Quilleuc[142], M. LeBlanc[7], T. LeCompte[6], F. Ledroit-Guillon[56], C.A. Lee[29], G.R. Lee[144a], L. Lee[57], S.C. Lee[155], B. Lefebvre[101], M. Lefebvre[173], F. Legger[112], C. Leggett[18], K. Lehmann[149], N. Lehmann[179], G. Lehmann Miotto[35], W.A. Leight[44], A. Leisos[159,w], M.A.L. Leite[78d], R. Leitner[140], D. Lellouch[177], K.J.C. Leney[92], T. Lenz[24], B. Lenzi[35], R. Leone[7], S. Leone[69a], C. Leonidopoulos[48], G. Lerner[153], C. Leroy[107], R. Les[164], A.A.J. Lesage[142], C.G. Lester[31], M. Levchenko[135], J. Levêque[5], D. Levin[103], L.J. Levinson[177], D. Lewis[90], B. Li[15b], B. Li[103], C-Q. Li[58a,am], H. Li[58a], H. Li[58b], L. Li[58c], M. Li[15a], Q. Li[15d], Q.Y. Li[58a], S. Li[58d,58c], X. Li[58c], Y. Li[148], Z. Liang[15a], B. Liberti[71a], A. Liblong[164], K. Lie[61c], S. Liem[118], A. Limosani[154],

2019 JINST 14 P03017

C.Y. Lin[31], K. Lin[104], T.H. Lin[97], R.A. Linck[63], J.H. Lindon[21], B.E. Lindquist[152], A.L. Lionti[52], E. Lipeles[134], A. Lipniacka[17], M. Lisovyi[59b], T.M. Liss[170,as], A. Lister[172], A.M. Litke[143], J.D. Little[8], B. Liu[76], B.L Liu[6], H.B. Liu[29], H. Liu[103], J.B. Liu[58a], J.K.K. Liu[132], K. Liu[133], M. Liu[58a], P. Liu[18], Y. Liu[15a], Y.L. Liu[58a], Y.W. Liu[58a], M. Livan[68a,68b], A. Lleres[56], J. Llorente Merino[15a], S.L. Lloyd[90], C.Y. Lo[61b], F. Lo Sterzo[41], E.M. Lobodzinska[44], P. Loch[7], T. Lohse[19], K. Lohwasser[146], M. Lokajicek[138], J.D. Long[170], R.E. Long[87], L. Longo[65a,65b], K.A. Looper[123], J.A. Lopez[144b], I. Lopez Paz[98], A. Lopez Solis[146], J. Lorenz[112], N. Lorenzo Martinez[5], M. Losada[22], P.J. Lösel[112], A. Lösle[50], X. Lou[44], X. Lou[15a], A. Lounis[129], J. Love[6], P.A. Love[87], J.J. Lozano Bahilo[171], H. Lu[61a], M. Lu[58a], Y.J. Lu[62], H.J. Lubatti[145], C. Luci[70a,70b], A. Lucotte[56], C. Luedtke[50], F. Luehring[63], I. Luise[133], L. Luminari[70a], B. Lund-Jensen[151], M.S. Lutz[100], P.M. Luzi[133], D. Lynn[29], R. Lysak[138], E. Lytken[94], F. Lyu[15a], V. Lyubushkin[77], T. Lyubushkina[77], H. Ma[29], L.L. Ma[58b], Y. Ma[58b], G. Maccarrone[49], A. Macchiolo[113], C.M. Macdonald[146], J. Machado Miguens[134,137b], D. Madaffari[171], R. Madar[37], W.F. Mader[46], N. Madysa[46], J. Maeda[80], K. Maekawa[160], S. Maeland[17], T. Maeno[29], M. Maerker[46], A.S. Maevskiy[111], V. Magerl[50], D.J. Mahon[38], C. Maidantchik[78b], T. Maier[112], A. Maio[137a,137b,137d], O. Majersky[28a], S. Majewski[128], Y. Makida[79], N. Makovec[129], B. Malaescu[133], Pa. Malecki[82], V.P. Maleev[135], F. Malek[56], U. Mallik[75], D. Malon[6], C. Malone[31], S. Maltezos[10], S. Malyukov[35], J. Mamuzic[171], G. Mancini[49], I. Mandić[89], J. Maneira[137a], L. Manhaes de Andrade Filho[78a], J. Manjarres Ramos[46], K.H. Mankinen[94], A. Mann[112], A. Manousos[74], B. Mansoulie[142], S. Manzoni[66a,66b], A. Marantis[159], G. Marceca[30], L. March[52], L. Marchese[132], G. Marchiori[133], M. Marcisovsky[138], C. Marcon[94], C.A. Marin Tobon[35], M. Marjanovic[37], F. Marroquim[78b], Z. Marshall[18], M.U.F Martensson[169], S. Marti-Garcia[171], C.B. Martin[123], T.A. Martin[175], V.J. Martin[48], B. Martin dit Latour[17], M. Martinez[14,z], V.I. Martinez Outschoorn[100], S. Martin-Haugh[141], V.S. Martoiu[27b], A.C. Martyniuk[92], A. Marzin[35], L. Masetti[97], T. Mashimo[160], R. Mashinistov[108], J. Masik[98], A.L. Maslennikov[120b,120a], L.H. Mason[102], L. Massa[71a,71b], P. Massarotti[67a,67b], P. Mastrandrea[152], A. Mastroberardino[40b,40a], T. Masubuchi[160], P. Mättig[24], J. Maurer[27b], B. Maček[89], S.J. Maxfield[88], D.A. Maximov[120b,120a], R. Mazini[155], I. Maznas[159], S.M. Mazza[143], S.P. Mc Kee[103], A. McCarn[41], T.G. McCarthy[113], L.I. McClymont[92], W.P. McCormack[18], E.F. McDonald[102], J.A. Mcfayden[35], G. Mchedlidze[51], M.A. McKay[41], K.D. McLean[173], S.J. McMahon[141], P.C. McNamara[102], C.J. McNicol[175], R.A. McPherson[173,ad], J.E. Mdhluli[32c], Z.A. Meadows[100], S. Meehan[145], T.M. Megy[50], S. Mehlhase[112], A. Mehta[88], T. Meideck[56], B. Meirose[42], D. Melini[171,h], B.R. Mellado Garcia[32c], J.D. Mellenthin[51], M. Melo[28a], F. Meloni[44], A. Melzer[24], S.B. Menary[98], E.D. Mendes Gouveia[137a], L. Meng[88], X.T. Meng[103], S. Menke[113], E. Meoni[40b,40a], S. Mergelmeyer[19], S.A.M. Merkt[136], C. Merlassino[20], P. Mermod[52], L. Merola[67a,67b], C. Meroni[66a], F.S. Merritt[36], A. Messina[70a,70b], J. Metcalfe[6], A.S. Mete[168], C. Meyer[63], J. Meyer[157], J-P. Meyer[142], H. Meyer Zu Theenhausen[59a], F. Miano[153], R.P. Middleton[141], L. Mijović[48], G. Mikenberg[177], M. Mikestikova[138], M. Mikuž[89], M. Milesi[102], A. Milic[164], D.A. Millar[90], D.W. Miller[36], A. Milov[177], D.A. Milstead[43a,43b], R.A. Mina[150,r], A.A. Minaenko[121], M. Miñano Moya[171], I.A. Minashvili[156b], A.I. Mincer[122], B. Mindur[81a], M. Mineev[77], Y. Minegishi[160], Y. Ming[178], L.M. Mir[14], A. Mirto[65a,65b], K.P. Mistry[134], T. Mitani[176], J. Mitrevski[112], V.A. Mitsou[171], M. Mittal[58c], A. Miucci[20], P.S. Miyagawa[146], A. Mizukami[79], J.U. Mjörnmark[94], T. Mkrtchyan[181], M. Mlynarikova[140], T. Moa[43a,43b], K. Mochizuki[107], P. Mogg[50], S. Mohapatra[38], S. Molander[43a,43b], R. Moles-Valls[24], M.C. Mondragon[104], K. Mönig[44], J. Monk[39], E. Monnier[99], A. Montalbano[149], J. Montejo Berlingen[35], F. Monticelli[86], S. Monzani[66a], N. Morange[129], D. Moreno[22], M. Moreno Llácer[35], P. Morettini[53b], M. Morgenstern[118], S. Morgenstern[46], D. Mori[149], M. Morii[57], M. Morinaga[176], V. Morisbak[131], A.K. Morley[35], G. Mornacchi[35], A.P. Morris[92], J.D. Morris[90], L. Morvaj[152], P. Moschovakos[10], M. Mosidze[156b], H.J. Moss[146], J. Moss[150,o], K. Motohashi[162], R. Mount[150], E. Mountricha[35], E.J.W. Moyse[100], S. Muanza[99], F. Mueller[113], J. Mueller[136], R.S.P. Mueller[112], D. Muenstermann[87], G.A. Mullier[94], F.J. Munoz Sanchez[98], P. Murin[28b], W.J. Murray[175,141], A. Murrone[66a,66b], M. Muškinja[89], C. Mwewa[32a], A.G. Myagkov[121,ao], J. Myers[128], M. Myska[139], B.P. Nachman[18], O. Nackenhorst[45], K. Nagai[132], K. Nagano[79], Y. Nagasaka[60], M. Nagel[50],

2019 JINST 14 P03017

E. Nagy[99], A.M. Nairz[35], Y. Nakahama[115], K. Nakamura[79], T. Nakamura[160], I. Nakano[124], H. Nanjo[130], F. Napolitano[59a], R.F. Naranjo Garcia[44], R. Narayan[11], D.I. Narrias Villar[59a], I. Naryshkin[135], T. Naumann[44], G. Navarro[22], R. Nayyar[7], H.A. Neal[103,*], P.Y. Nechaeva[108], T.J. Neep[142], A. Negri[68a,68b], M. Negrini[23b], S. Nektarijevic[117], C. Nellist[51], M.E. Nelson[132], S. Nemecek[138], P. Nemethy[122], M. Nessi[35,f], M.S. Neubauer[170], M. Neumann[179], P.R. Newman[21], T.Y. Ng[61c], Y.S. Ng[19], Y.W.Y. Ng[168], H.D.N. Nguyen[99], T. Nguyen Manh[107], E. Nibigira[37], R.B. Nickerson[132], R. Nicolaidou[142], D.S. Nielsen[39], J. Nielsen[143], N. Nikiforou[11], V. Nikolaenko[121,ao], I. Nikolic-Audit[133], K. Nikolopoulos[21], P. Nilsson[29], H.R. Nindhito[52], Y. Ninomiya[79], A. Nisati[70a], N. Nishu[58c], R. Nisius[113], I. Nitsche[45], T. Nitta[176], T. Nobe[160], Y. Noguchi[83], M. Nomachi[130], I. Nomidis[133], M.A. Nomura[29], T. Nooney[90], M. Nordberg[35], N. Norjoharuddeen[132], T. Novak[89], O. Novgorodova[46], R. Novotny[139], L. Nozka[127], K. Ntekas[168], E. Nurse[92], F. Nuti[102], F.G. Oakham[33,av], H. Oberlack[113], J. Ocariz[133], A. Ochi[80], I. Ochoa[38], J.P. Ochoa-Ricoux[144a], K. O'Connor[26], S. Oda[85], S. Odaka[79], S. Oerdek[51], A. Oh[98], S.H. Oh[47], C.C. Ohm[151], H. Oide[53b,53a], M.L. Ojeda[164], H. Okawa[166], Y. Okazaki[83], Y. Okumura[160], T. Okuyama[79], A. Olariu[27b], L.F. Oleiro Seabra[137a], S.A. Olivares Pino[144a], D. Oliveira Damazio[29], J.L. Oliver[1], M.J.R. Olsson[36], A. Olszewski[82], J. Olszowska[82], D.C. O'Neil[149], A. Onofre[137a,137e], K. Onogi[115], P.U.E. Onyisi[11], H. Oppen[131], M.J. Oreglia[36], G.E. Orellana[86], Y. Oren[158], D. Orestano[72a,72b], E.C. Orgill[98], N. Orlando[61b], A.A. O'Rourke[44], R.S. Orr[164], B. Osculati[53b,53a,*], V. O'Shea[55], R. Ospanov[58a], G. Otero y Garzon[30], H. Otono[85], M. Ouchrif[34d], F. Ould-Saada[131], A. Ouraou[142], Q. Ouyang[15a], M. Owen[55], R.E. Owen[21], V.E. Ozcan[12c], N. Ozturk[8], J. Pacalt[127], H.A. Pacey[31], K. Pachal[149], A. Pacheco Pages[14], L. Pacheco Rodriguez[142], C. Padilla Aranda[14], S. Pagan Griso[18], M. Paganini[180], G. Palacino[63], S. Palazzo[48], S. Palestini[35], M. Palka[81b], D. Pallin[37], I. Panagoulias[10], C.E. Pandini[35], J.G. Panduro Vazquez[91], P. Pani[35], G. Panizzo[64a,64c], L. Paolozzi[52], T.D. Papadopoulou[10], K. Papageorgiou[9,k], A. Paramonov[6], D. Paredes Hernandez[61b], S.R. Paredes Saenz[132], B. Parida[163], T.H. Park[33], A.J. Parker[87], K.A. Parker[44], M.A. Parker[31], F. Parodi[53b,53a], J.A. Parsons[38], U. Parzefall[50], V.R. Pascuzzi[164], J.M.P. Pasner[143], E. Pasqualucci[70a], S. Passaggio[53b], F. Pastore[91], P. Pasuwan[43a,43b], S. Pataraia[97], J.R. Pater[98], A. Pathak[178,l], T. Pauly[35], B. Pearson[113], M. Pedersen[131], L. Pedraza Diaz[117], R. Pedro[137a,137b], S.V. Peleganchuk[120b,120a], O. Penc[138], C. Peng[15d], H. Peng[58a], B.S. Peralva[78a], M.M. Perego[129], A.P. Pereira Peixoto[137a], D.V. Perepelitsa[29], F. Peri[19], L. Perini[66a,66b], H. Pernegger[35], S. Perrella[67a,67b], V.D. Peshekhonov[77,*], K. Peters[44], R.F.Y. Peters[98], B.A. Petersen[35], T.C. Petersen[39], E. Petit[56], A. Petridis[1], C. Petridou[159], P. Petroff[129], M. Petrov[132], F. Petrucci[72a,72b], M. Pettee[180], N.E. Pettersson[100], A. Peyaud[142], R. Pezoa[144b], T. Pham[102], F.H. Phillips[104], P.W. Phillips[141], M.W. Phipps[170], G. Piacquadio[152], E. Pianori[18], A. Picazio[100], R.H. Pickles[98], R. Piegaia[30], J.E. Pilcher[36], A.D. Pilkington[98], M. Pinamonti[71a,71b], J.L. Pinfold[3], M. Pitt[177], L. Pizzimento[71a,71b], M.-A. Pleier[29], V. Pleskot[140], E. Plotnikova[77], D. Pluth[76], P. Podberezko[120b,120a], R. Poettgen[94], R. Poggi[52], L. Poggioli[129], I. Pogrebnyak[104], D. Pohl[24], I. Pokharel[51], G. Polesello[68a], A. Poley[18], A. Policicchio[70a,70b], R. Polifka[35], A. Polini[23b], C.S. Pollard[44], V. Polychronakos[29], D. Ponomarenko[110], L. Pontecorvo[35], G.A. Popeneciu[27d], D.M. Portillo Quintero[133], S. Pospisil[139], K. Potamianos[44], I.N. Potrap[77], C.J. Potter[31], H. Potti[11], T. Poulsen[94], J. Poveda[35], T.D. Powell[146], M.E. Pozo Astigarraga[35], P. Pralavorio[99], S. Prell[76], D. Price[98], M. Primavera[65a], S. Prince[101], M.L. Proffitt[145], N. Proklova[110], K. Prokofiev[61c], F. Prokoshin[144b], S. Protopopescu[29], J. Proudfoot[6], M. Przybycien[81a], A. Puri[170], P. Puzo[129], J. Qian[103], Y. Qin[98], A. Quadt[51], M. Queitsch-Maitland[44], A. Qureshi[1], P. Rados[102], F. Ragusa[66a,66b], G. Rahal[95], J.A. Raine[52], S. Rajagopalan[29], A. Ramirez Morales[90], K. Ran[15a], T. Rashid[129], S. Raspopov[5], M.G. Ratti[66a,66b], D.M. Rauch[44], F. Rauscher[112], S. Rave[97], B. Ravina[146], I. Ravinovich[177], J.H. Rawling[98], M. Raymond[35], A.L. Read[131], N.P. Readioff[56], M. Reale[65a,65b], D.M. Rebuzzi[68a,68b], A. Redelbach[174], G. Redlinger[29], R. Reece[143], R.G. Reed[32c], K. Reeves[42], L. Rehnisch[19], J. Reichert[134], D. Reikher[158], A. Reiss[97], A. Rej[148], C. Rembser[35], H. Ren[15d], M. Rescigno[70a], S. Resconi[66a], E.D. Resseguie[134], S. Rettie[172], E. Reynolds[21], O.L. Rezanova[120b,120a], P. Reznicek[140], E. Ricci[73a,73b], R. Richter[113], S. Richter[44], E. Richter-Was[81b], O. Ricken[24], M. Ridel[133], P. Rieck[113], C.J. Riegel[179], O. Rifki[44], M. Rijssenbeek[152], A. Rimoldi[68a,68b],

2019 JINST 14 P03017

M. Rimoldi[20], L. Rinaldi[23b], G. Ripellino[151], B. Ristić[87], E. Ritsch[35], I. Riu[14], J.C. Rivera Vergara[144a], F. Rizatdinova[126], E. Rizvi[90], C. Rizzi[14], R.T. Roberts[98], S.H. Robertson[101,ad], D. Robinson[31], J.E.M. Robinson[44], A. Robson[55], E. Rocco[97], C. Roda[69a,69b], Y. Rodina[99], S. Rodriguez Bosca[171], A. Rodriguez Perez[14], D. Rodriguez Rodriguez[171], A.M. Rodríguez Vera[165b], S. Roe[35], C.S. Rogan[57], O. Røhne[131], R. Röhrig[113], C.P.A. Roland[63], J. Roloff[57], A. Romaniouk[110], M. Romano[23b,23a], N. Rompotis[88], M. Ronzani[122], L. Roos[133], S. Rosati[70a], K. Rosbach[50], N-A. Rosien[51], B.J. Rosser[134], E. Rossi[44], E. Rossi[72a,72b], E. Rossi[67a,67b], L.P. Rossi[53b], L. Rossini[66a,66b], J.H.N. Rosten[31], R. Rosten[14], M. Rotaru[27b], J. Rothberg[145], D. Rousseau[129], D. Roy[32c], A. Rozanov[99], Y. Rozen[157], X. Ruan[32c], F. Rubbo[150], F. Rühr[50], A. Ruiz-Martinez[171], Z. Rurikova[50], N.A. Rusakovich[77], H.L. Russell[101], J.P. Rutherfoord[7], E.M. Rüttinger[44,m], Y.F. Ryabov[135], M. Rybar[38], G. Rybkin[129], S. Ryu[6], A. Ryzhov[121], G.F. Rzehorz[51], P. Sabatini[51], G. Sabato[118], S. Sacerdoti[129], H.F-W. Sadrozinski[143], R. Sadykov[77], F. Safai Tehrani[70a], P. Saha[119], M. Sahinsoy[59a], A. Sahu[179], M. Saimpert[44], M. Saito[160], T. Saito[160], H. Sakamoto[160], A. Sakharov[122,an], D. Salamani[52], G. Salamanna[72a,72b], J.E. Salazar Loyola[144b], P.H. Sales De Bruin[169], D. Salihagic[113], A. Salnikov[150], J. Salt[171], D. Salvatore[40b,40a], F. Salvatore[153], A. Salvucci[61a,61b,61c], A. Salzburger[35], J. Samarati[35], D. Sammel[50], D. Sampsonidis[159], D. Sampsonidou[159], J. Sánchez[171], A. Sanchez Pineda[64a,64c], H. Sandaker[131], C.O. Sander[44], M. Sandhoff[179], C. Sandoval[22], D.P.C. Sankey[141], M. Sannino[53b,53a], Y. Sano[115], A. Sansoni[49], C. Santoni[37], H. Santos[137a], I. Santoyo Castillo[153], A. Santra[171], A. Sapronov[77], J.G. Saraiva[137a,137d], O. Sasaki[79], K. Sato[166], E. Sauvan[5], P. Savard[164,av], N. Savic[113], R. Sawada[160], C. Sawyer[141], L. Sawyer[93,al], C. Sbarra[23b], A. Sbrizzi[23a], T. Scanlon[92], J. Schaarschmidt[145], P. Schacht[113], B.M. Schachtner[112], D. Schaefer[36], L. Schaefer[134], J. Schaeffer[97], S. Schaepe[35], U. Schäfer[97], A.C. Schaffer[129], D. Schaile[112], R.D. Schamberger[152], N. Scharmberg[98], V.A. Schegelsky[135], D. Scheirich[140], F. Schenck[19], M. Schernau[168], C. Schiavi[53b,53a], S. Schier[143], L.K. Schildgen[24], Z.M. Schillaci[26], E.J. Schioppa[35], M. Schioppa[40b,40a], K.E. Schleicher[50], S. Schlenker[35], K.R. Schmidt-Sommerfeld[113], K. Schmieden[35], C. Schmitt[97], S. Schmitt[44], S. Schmitz[97], J.C. Schmoeckel[44], U. Schnoor[50], L. Schoeffel[142], A. Schoening[59b], E. Schopf[132], M. Schott[97], J.F.P. Schouwenberg[117], J. Schovancova[35], S. Schramm[52], A. Schulte[97], H-C. Schultz-Coulon[59a], M. Schumacher[50], B.A. Schumm[143], Ph. Schune[142], A. Schwartzman[150], T.A. Schwarz[103], Ph. Schwemling[142], R. Schwienhorst[104], A. Sciandra[24], G. Sciolla[26], M. Scornajenghi[40b,40a], F. Scuri[69a], F. Scutti[102], L.M. Scyboz[113], C.D. Sebastiani[70a,70b], P. Seema[19], S.C. Seidel[116], A. Seiden[143], T. Seiss[36], J.M. Seixas[78b], G. Sekhniaidze[67a], K. Sekhon[103], S.J. Sekula[41], N. Semprini-Cesari[23b,23a], S. Sen[47], S. Senkin[37], C. Serfon[131], L. Serin[129], L. Serkin[64a,64b], M. Sessa[58a], H. Severini[125], F. Sforza[167], A. Sfyrla[52], E. Shabalina[51], J.D. Shahinian[143], N.W. Shaikh[43a,43b], D. Shaked Renous[177], L.Y. Shan[15a], R. Shang[170], J.T. Shank[25], M. Shapiro[18], A.S. Sharma[1], A. Sharma[132], P.B. Shatalov[109], K. Shaw[153], S.M. Shaw[98], A. Shcherbakova[135], Y. Shen[125], N. Sherafati[33], A.D. Sherman[25], P. Sherwood[92], L. Shi[155,ar], S. Shimizu[79], C.O. Shimmin[180], Y. Shimogama[176], M. Shimojima[114], I.P.J. Shipsey[132], S. Shirabe[85], M. Shiyakova[77], J. Shlomi[177], A. Shmeleva[108], D. Shoaleh Saadi[107], M.J. Shochet[36], S. Shojaii[102], D.R. Shope[125], S. Shrestha[123], E. Shulga[110], P. Sicho[138], A.M. Sickles[170], P.E. Sidebo[151], E. Sideras Haddad[32c], O. Sidiropoulou[35], A. Sidoti[23b,23a], F. Siegert[46], Dj. Sijacki[16], J. Silva[137a], M. Silva Jr.[178], M.V. Silva Oliveira[78a], S.B. Silverstein[43a], S. Simion[129], E. Simioni[97], M. Simon[97], R. Simoniello[97], P. Sinervo[164], N.B. Sinev[128], M. Sioli[23b,23a], I. Siral[103], S.Yu. Sivoklokov[111], J. Sjölin[43a,43b], P. Skubic[125], M. Slater[21], T. Slavicek[139], M. Slawinska[82], K. Sliwa[167], R. Slovak[140], V. Smakhtin[177], B.H. Smart[5], J. Smiesko[28a], N. Smirnov[110], S.Yu. Smirnov[110], Y. Smirnov[110], L.N. Smirnova[111], O. Smirnova[94], J.W. Smith[51], M. Smizanska[87], K. Smolek[139], A. Smykiewicz[82], A.A. Snesarev[108], I.M. Snyder[128], S. Snyder[29], R. Sobie[173,ad], A.M. Soffa[168], A. Soffer[158], A. Søgaard[48], F. Sohns[51], G. Sokhrannyi[89], C.A. Solans Sanchez[35], M. Solar[139], E.Yu. Soldatov[110], U. Soldevila[171], A.A. Solodkov[121], A. Soloshenko[77], O.V. Solovyanov[121], V. Solovyev[135], P. Sommer[146], H. Son[167], W. Song[141], W.Y. Song[165b], A. Sopczak[139], F. Sopkova[28b], C.L. Sotiropoulou[69a,69b], S. Sottocornola[68a,68b], R. Soualah[64a,64c,j], A.M. Soukharev[120b,120a], D. South[44], S. Spagnolo[65a,65b], M. Spalla[113],

2019 JINST 14 P03017

M. Spangenberg[175], F. Spanò[91], D. Sperlich[19], T.M. Spieker[59a], R. Spighi[23b], G. Spigo[35], L.A. Spiller[102], D.P. Spiteri[55], M. Spousta[140], A. Stabile[66a,66b], R. Stamen[59a], S. Stamm[19], E. Stanecka[82], R.W. Stanek[6], C. Stanescu[72a], B. Stanislaus[132], M.M. Stanitzki[44], B. Stapf[118], S. Stapnes[131], E.A. Starchenko[121], G.H. Stark[143], J. Stark[56], S.H Stark[39], P. Staroba[138], P. Starovoitov[59a], S. Stärz[101], R. Staszewski[82], M. Stegler[44], P. Steinberg[29], B. Stelzer[149], H.J. Stelzer[35], O. Stelzer-Chilton[165a], H. Stenzel[54], T.J. Stevenson[90], G.A. Stewart[35], M.C. Stockton[35], G. Stoicea[27b], P. Stolte[51], S. Stonjek[113], A. Straessner[46], J. Strandberg[151], S. Strandberg[43a,43b], M. Strauss[125], P. Strizenec[28b], R. Ströhmer[174], D.M. Strom[128], R. Stroynowski[41], A. Strubig[48], S.A. Stucci[29], B. Stugu[17], J. Stupak[125], N.A. Styles[44], D. Su[150], J. Su[136], S. Suchek[59a], Y. Sugaya[130], M. Suk[139], V.V. Sulin[108], M.J. Sullivan[88], D.M.S. Sultan[52], S. Sultansoy[4c], T. Sumida[83], S. Sun[103], X. Sun[3], K. Suruliz[153], C.J.E. Suster[154], M.R. Sutton[153], S. Suzuki[79], M. Svatos[138], M. Swiatlowski[36], S.P. Swift[2], A. Sydorenko[97], I. Sykora[28a], M. Sykora[140], T. Sykora[140], D. Ta[97], K. Tackmann[44,aa], J. Taenzer[158], A. Taffard[168], R. Tafirout[165a], E. Tahirovic[90], N. Taiblum[158], H. Takai[29], R. Takashima[84], E.H. Takasugi[113], K. Takeda[80], T. Takeshita[147], Y. Takubo[79], M. Talby[99], A.A. Talyshev[120b,120a], J. Tanaka[160], M. Tanaka[162], R. Tanaka[129], B.B. Tannenwald[123], S. Tapia Araya[144b], S. Tapprogge[97], A. Tarek Abouelfadl Mohamed[133], S. Tarem[157], G. Tarna[27b,e], G.F. Tartarelli[66a], P. Tas[140], M. Tasevsky[138], T. Tashiro[83], E. Tassi[40b,40a], A. Tavares Delgado[137a,137b], Y. Tayalati[34e], A.J. Taylor[48], G.N. Taylor[102], P.T.E. Taylor[102], W. Taylor[165b], A.S. Tee[87], R. Teixeira De Lima[150], P. Teixeira-Dias[91], H. Ten Kate[35], J.J. Teoh[118], S. Terada[79], K. Terashi[160], J. Terron[96], S. Terzo[14], M. Testa[49], R.J. Teuscher[164,ad], S.J. Thais[180], T. Theveneaux-Pelzer[44], F. Thiele[39], D.W. Thomas[91], J.P. Thomas[21], A.S. Thompson[55], P.D. Thompson[21], L.A. Thomsen[180], E. Thomson[134], Y. Tian[38], R.E. Ticse Torres[51], V.O. Tikhomirov[108,ap], Yu.A. Tikhonov[120b,120a], S. Timoshenko[110], P. Tipton[180], S. Tisserant[99], K. Todome[162], S. Todorova-Nova[5], S. Todt[46], J. Tojo[85], S. Tokár[28a], K. Tokushuku[79], E. Tolley[123], K.G. Tomiwa[32c], M. Tomoto[115], L. Tompkins[150,r], K. Toms[116], B. Tong[57], P. Tornambe[50], E. Torrence[128], H. Torres[46], E. Torró Pastor[145], C. Tosciri[132], J. Toth[99,ac], F. Touchard[99], D.R. Tovey[146], C.J. Treado[122], T. Trefzger[174], F. Tresoldi[153], A. Tricoli[29], I.M. Trigger[165a], S. Trincaz-Duvoid[133], W. Trischuk[164], B. Trocmé[56], A. Trofymov[129], C. Troncon[66a], M. Trovatelli[173], F. Trovato[153], L. Truong[32b], M. Trzebinski[82], A. Trzupek[82], F. Tsai[44], J.C-L. Tseng[132], P.V. Tsiareshka[105,aj], A. Tsirigotis[159], N. Tsirintanis[9], V. Tsiskaridze[152], E.G. Tskhadadze[156a], I.I. Tsukerman[109], V. Tsulaia[18], S. Tsuno[79], D. Tsybychev[152,163], Y. Tu[61b], A. Tudorache[27b], V. Tudorache[27b], T.T. Tulbure[27a], A.N. Tuna[57], S. Turchikhin[77], D. Turgeman[177], I. Turk Cakir[4b,u], R. Turra[66a], P.M. Tuts[38], S Tzamarias[159], E. Tzovara[97], G. Ucchielli[45], I. Ueda[79], M. Ughetto[43a,43b], F. Ukegawa[166], G. Unal[35], A. Undrus[29], G. Unel[168], F.C. Ungaro[102], Y. Unno[79], K. Uno[160], J. Urban[28b], P. Urquijo[102], G. Usai[8], J. Usui[79], L. Vacavant[99], V. Vacek[139], B. Vachon[101], K.O.H. Vadla[131], A. Vaidya[92], C. Valderanis[112], E. Valdes Santurio[43a,43b], M. Valente[52], S. Valentinetti[23b,23a], A. Valero[171], L. Valéry[44], R.A. Vallance[21], A. Vallier[5], J.A. Valls Ferrer[171], T.R. Van Daalen[14], H. Van der Graaf[118], P. Van Gemmeren[6], I. Van Vulpen[118], M. Vanadia[71a,71b], W. Vandelli[35], A. Vaniachine[163], P. Vankov[118], R. Vari[70a], E.W. Varnes[7], C. Varni[53b,53a], T. Varol[41], D. Varouchas[129], K.E. Varvell[154], G.A. Vasquez[144b], J.G. Vasquez[180], F. Vazeille[37], D. Vazquez Furelos[14], T. Vazquez Schroeder[35], J. Veatch[51], V. Vecchio[72a,72b], L.M. Veloce[164], F. Veloso[137a,137c], S. Veneziano[70a], A. Ventura[65a,65b], N. Venturi[35], V. Vercesi[68a], M. Verducci[72a,72b], C.M. Vergel Infante[76], C. Vergis[24], W. Verkerke[118], A.T. Vermeulen[118], J.C. Vermeulen[118], M.C. Vetterli[149,av], N. Viaux Maira[144b], M. Vicente Barreto Pinto[52], I. Vichou[170,*], T. Vickey[146], O.E. Vickey Boeriu[146], G.H.A. Viehhauser[132], S. Viel[18], L. Vigani[132], M. Villa[23b,23a], M. Villaplana Perez[66a,66b], E. Vilucchi[49], M.G. Vincter[33], V.B. Vinogradov[77], A. Vishwakarma[44], C. Vittori[23b,23a], I. Vivarelli[153], S. Vlachos[10], M. Vogel[179], P. Vokac[139], G. Volpi[14], S.E. von Buddenbrock[32c], E. Von Toerne[24], V. Vorobel[140], K. Vorobev[110], M. Vos[171], J.H. Vossebeld[88], N. Vranjes[16], M. Vranjes Milosavljevic[16], V. Vrba[139], M. Vreeswijk[118], T. Šfiligoj[89], R. Vuillermet[35], I. Vukotic[36], T. Ženiš[28a], L. Živković[16], P. Wagner[24], W. Wagner[179], J. Wagner-Kuhr[112], H. Wahlberg[86], S. Wahrmund[46], K. Wakamiya[80], V.M. Walbrecht[113], J. Walder[87], R. Walker[112], S.D. Walker[91], W. Walkowiak[148], V. Wallangen[43a,43b], A.M. Wang[57], C. Wang[58b],

2019 JINST 14 P03017

F. Wang[178], H. Wang[18], H. Wang[3], J. Wang[154], J. Wang[59b], P. Wang[41], Q. Wang[125], R.-J. Wang[133], R. Wang[58a], R. Wang[6], S.M. Wang[155], W.T. Wang[58a], W. Wang[15c,ae], W.X. Wang[58a,ae], Y. Wang[58a,am], Z. Wang[58c], C. Wanotayaroj[44], A. Warburton[101], C.P. Ward[31], D.R. Wardrope[92], A. Washbrook[48], P.M. Watkins[21], A.T. Watson[21], M.F. Watson[21], G. Watts[145], S. Watts[98], B.M. Waugh[92], A.F. Webb[11], S. Webb[97], C. Weber[180], M.S. Weber[20], S.A. Weber[33], S.M. Weber[59a], A.R. Weidberg[132], J. Weingarten[45], M. Weirich[97], C. Weiser[50], P.S. Wells[35], T. Wenaus[29], T. Wengler[35], S. Wenig[35], N. Wermes[24], M.D. Werner[76], P. Werner[35], M. Wessels[59a], T.D. Weston[20], K. Whalen[128], N.L. Whallon[145], A.M. Wharton[87], A.S. White[103], A. White[8], M.J. White[1], R. White[144b], D. Whiteson[168], B.W. Whitmore[87], F.J. Wickens[141], W. Wiedenmann[178], M. Wielers[141], C. Wiglesworth[39], L.A.M. Wiik-Fuchs[50], F. Wilk[98], H.G. Wilkens[35], L.J. Wilkins[91], H.H. Williams[134], S. Williams[31], C. Willis[104], S. Willocq[100], J.A. Wilson[21], I. Wingerter-Seez[5], E. Winkels[153], F. Winklmeier[128], O.J. Winston[153], B.T. Winter[50], M. Wittgen[150], M. Wobisch[93], A. Wolf[97], T.M.H. Wolf[118], R. Wolff[99], J. Wollrath[50], M.W. Wolter[82], H. Wolters[137a,137c], V.W.S. Wong[172], N.L. Woods[143], S.D. Worm[21], B.K. Wosiek[82], K.W. Woźniak[82], K. Wraight[55], M. Wu[36], S.L. Wu[178], X. Wu[52], Y. Wu[58a], T.R. Wyatt[98], B.M. Wynne[48], S. Xella[39], Z. Xi[103], L. Xia[175], D. Xu[15a], H. Xu[58a,e], L. Xu[29], T. Xu[142], W. Xu[103], Z. Xu[150], B. Yabsley[154], S. Yacoob[32a], K. Yajima[130], D.P. Yallup[92], D. Yamaguchi[162], Y. Yamaguchi[162], A. Yamamoto[79], T. Yamanaka[160], F. Yamane[80], M. Yamatani[160], T. Yamazaki[160], Y. Yamazaki[80], Z. Yan[25], H.J. Yang[58c,58d], H.T. Yang[18], S. Yang[75], Y. Yang[160], Z. Yang[17], W-M. Yao[18], Y.C. Yap[44], Y. Yasu[79], E. Yatsenko[58c,58d], J. Ye[41], S. Ye[29], I. Yeletskikh[77], E. Yigitbasi[25], E. Yildirim[97], K. Yorita[176], K. Yoshihara[134], C.J.S. Young[35], C. Young[150], J. Yu[8], J. Yu[76], X. Yue[59a], S.P.Y. Yuen[24], B. Zabinski[82], G. Zacharis[10], E. Zaffaroni[52], R. Zaidan[14], A.M. Zaitsev[121,ao], T. Zakareishvili[156b], N. Zakharchuk[33], S. Zambito[57], D. Zanzi[35], D.R. Zaripovas[55], S.V. Zeißner[45], C. Zeitnitz[179], G. Zemaityte[132], J.C. Zeng[170], Q. Zeng[150], O. Zenin[121], D. Zerwas[129], M. Zgubič[132], D.F. Zhang[58b], D. Zhang[103], F. Zhang[178], G. Zhang[58a], G. Zhang[15b], H. Zhang[15c], J. Zhang[6], L. Zhang[15c], L. Zhang[58a], M. Zhang[170], P. Zhang[15c], R. Zhang[58a], R. Zhang[24], X. Zhang[58b], Y. Zhang[15d], Z. Zhang[129], P. Zhao[47], Y. Zhao[58b,129,ak], Z. Zhao[58a], A. Zhemchugov[77], Z. Zheng[103], D. Zhong[170], B. Zhou[103], C. Zhou[178], M.S. Zhou[15d], M. Zhou[152], N. Zhou[58c], Y. Zhou[7], C.G. Zhu[58b], H.L. Zhu[58a], H. Zhu[15a], J. Zhu[103], Y. Zhu[58a], X. Zhuang[15a], K. Zhukov[108], V. Zhulanov[120b,120a], A. Zibell[174], D. Zieminska[63], N.I. Zimine[77], S. Zimmermann[50], Z. Zinonos[113], M. Ziolkowski[148], G. Zobernig[178], A. Zoccoli[23b,23a], K. Zoch[51], T.G. Zorbas[146], R. Zou[36], M. Zur Nedden[19], L. Zwalinski[35]

[1] Department of Physics, University of Adelaide, Adelaide, Australia
[2] Physics Department, SUNY Albany, Albany NY, U.S.A.
[3] Department of Physics, University of Alberta, Edmonton AB, Canada
[4] Department of Physics$^{(a)}$, Ankara University, Ankara, Istanbul Aydin University$^{(b)}$, Istanbul, Division of Physics$^{(c)}$, TOBB University of Economics and Technology, Ankara, Turkey
[5] LAPP, Université Grenoble Alpes, Université Savoie Mont Blanc, CNRS/IN2P3, Annecy, France
[6] High Energy Physics Division, Argonne National Laboratory, Argonne IL, U.S.A.
[7] Department of Physics, University of Arizona, Tucson AZ, U.S.A.
[8] Department of Physics, University of Texas at Arlington, Arlington TX, U.S.A.
[9] Physics Department, National and Kapodistrian University of Athens, Athens, Greece
[10] Physics Department, National Technical University of Athens, Zografou, Greece
[11] Department of Physics, University of Texas at Austin, Austin TX, U.S.A.
[12] Bahcesehir University$^{(a)}$, Faculty of Engineering and Natural Sciences, Istanbul; Istanbul Bilgi University$^{(b)}$, Faculty of Engineering and Natural Sciences, Istanbul; Department of Physics$^{(c)}$, Bogazici University, Istanbul; Department of Physics Engineering$^{(d)}$, Gaziantep University, Gaziantep, Turkey
[13] Institute of Physics, Azerbaijan Academy of Sciences, Baku, Azerbaijan
[14] Institut de Física d'Altes Energies (IFAE), Barcelona Institute of Science and Technology, Barcelona, Spain
[15] Institute of High Energy Physics$^{(a)}$, Chinese Academy of Sciences, Beijing; Physics Department$^{(b)}$, Tsinghua University, Beijing; Department of Physics$^{(c)}$, Nanjing University, Nanjing; University of Chinese Academy of Science (UCAS)$^{(d)}$, Beijing, China

2019 JINST 14 P03017

[16] Institute of Physics, University of Belgrade, Belgrade, Serbia
[17] Department for Physics and Technology, University of Bergen, Bergen, Norway
[18] Physics Division, Lawrence Berkeley National Laboratory and University of California, Berkeley CA, U.S.A.
[19] Institut für Physik, Humboldt Universität zu Berlin, Berlin, Germany
[20] Albert Einstein Center for Fundamental Physics and Laboratory for High Energy Physics, University of Bern, Bern, Switzerland
[21] School of Physics and Astronomy, University of Birmingham, Birmingham, U.K.
[22] Centro de Investigaciónes, Universidad Antonio Nariño, Bogota, Colombia
[23] Dipartimento di Fisica e Astronomia[(a)], Università di Bologna, Bologna; INFN Sezione di Bologna[(b)], Italy
[24] Physikalisches Institut, Universität Bonn, Bonn, Germany
[25] Department of Physics, Boston University, Boston MA, U.S.A.
[26] Department of Physics, Brandeis University, Waltham MA, U.S.A.
[27] Transilvania University of Brasov[(a)], Brasov; Horia Hulubei National Institute of Physics and Nuclear Engineering[(b)], Bucharest; Department of Physics[(c)], Alexandru Ioan Cuza University of Iasi, Iasi; National Institute for Research and Development of Isotopic and Molecular Technologies[(d)], Physics Department, Cluj-Napoca; University Politehnica Bucharest[(e)], Bucharest; West University in Timisoara[(f)], Timisoara, Romania
[28] Faculty of Mathematics[(a)], Physics and Informatics, Comenius University, Bratislava; Department of Subnuclear Physics[(b)], Institute of Experimental Physics of the Slovak Academy of Sciences, Kosice, Slovak Republic
[29] Physics Department, Brookhaven National Laboratory, Upton NY, U.S.A.
[30] Departamento de Física, Universidad de Buenos Aires, Buenos Aires, Argentina
[31] Cavendish Laboratory, University of Cambridge, Cambridge, U.K.
[32] Department of Physics[(a)], University of Cape Town, Cape Town; Department of Mechanical Engineering Science[(b)], University of Johannesburg, Johannesburg; School of Physics[(c)], University of the Witwatersrand, Johannesburg, South Africa
[33] Department of Physics, Carleton University, Ottawa ON, Canada
[34] Faculté des Sciences Ain Chock[(a)], Réseau Universitaire de Physique des Hautes Energies — Université Hassan II, Casablanca; Centre National de l'Energie des Sciences Techniques Nucleaires (CNESTEN)[(b)], Rabat; Faculté des Sciences Semlalia[(c)], Université Cadi Ayyad, LPHEA-Marrakech; Faculté des Sciences[(d)], Université Mohamed Premier and LPTPM, Oujda; Faculté des sciences[(e)], Université Mohammed V, Rabat, Morocco
[35] CERN, Geneva, Switzerland
[36] Enrico Fermi Institute, University of Chicago, Chicago IL, U.S.A.
[37] LPC, Université Clermont Auvergne, CNRS/IN2P3, Clermont-Ferrand, France
[38] Nevis Laboratory, Columbia University, Irvington NY, U.S.A.
[39] Niels Bohr Institute, University of Copenhagen, Copenhagen, Denmark
[40] Dipartimento di Fisica[(a)], Università della Calabria, Rende; INFN Gruppo Collegato di Cosenza[(b)], Laboratori Nazionali di Frascati, Italy
[41] Physics Department, Southern Methodist University, Dallas TX, U.S.A.
[42] Physics Department, University of Texas at Dallas, Richardson TX, U.S.A.
[43] Department of Physics[(a)], Stockholm University; Oskar Klein Centre[(b)], Stockholm, Sweden
[44] Deutsches Elektronen-Synchrotron DESY, Hamburg and Zeuthen, Germany
[45] Lehrstuhl für Experimentelle Physik IV, Technische Universität Dortmund, Dortmund, Germany
[46] Institut für Kern- und Teilchenphysik, Technische Universität Dresden, Dresden, Germany
[47] Department of Physics, Duke University, Durham NC, U.S.A.
[48] SUPA — School of Physics and Astronomy, University of Edinburgh, Edinburgh, U.K.
[49] INFN e Laboratori Nazionali di Frascati, Frascati, Italy
[50] Physikalisches Institut, Albert-Ludwigs-Universität Freiburg, Freiburg, Germany
[51] II. Physikalisches Institut, Georg-August-Universität Göttingen, Göttingen, Germany
[52] Département de Physique Nucléaire et Corpusculaire, Université de Genève, Genève, Switzerland
[53] Dipartimento di Fisica[(a)], Università di Genova, Genova; INFN Sezione di Genova[(b)], Italy
[54] II. Physikalisches Institut, Justus-Liebig-Universität Giessen, Giessen, Germany
[55] SUPA — School of Physics and Astronomy, University of Glasgow, Glasgow, U.K.

2019 JINST 14 P03017

[56] LPSC, Université Grenoble Alpes, CNRS/IN2P3, Grenoble INP, Grenoble, France
[57] Laboratory for Particle Physics and Cosmology, Harvard University, Cambridge MA, U.S.A.
[58] Department of Modern Physics and State Key Laboratory of Particle Detection and Electronics[(a)], University of Science and Technology of China, Hefei; Institute of Frontier and Interdisciplinary Science and Key Laboratory of Particle Physics and Particle Irradiation (MOE)[(b)], Shandong University, Qingdao; School of Physics and Astronomy[(c)], Shanghai Jiao Tong University, KLPPAC-MoE, SKLPPC, Shanghai; Tsung-Dao Lee Institute[(d)], Shanghai, China
[59] Kirchhoff-Institut für Physik[(a)], Ruprecht-Karls-Universität Heidelberg, Heidelberg; Physikalisches Institut[(b)], Ruprecht-Karls-Universität Heidelberg, Heidelberg, Germany
[60] Faculty of Applied Information Science, Hiroshima Institute of Technology, Hiroshima, Japan
[61] Department of Physics[(a)], Chinese University of Hong Kong, Shatin, N.T., Hong Kong; Department of Physics[(b)], University of Hong Kong, Hong Kong; Department of Physics and Institute for Advanced Study[(c)], Hong Kong University of Science and Technology, Clear Water Bay, Kowloon, Hong Kong, China
[62] Department of Physics, National Tsing Hua University, Hsinchu, Taiwan
[63] Department of Physics, Indiana University, Bloomington IN, U.S.A.
[64] INFN Gruppo Collegato di Udine[(a)], Sezione di Trieste, Udine; ICTP[(b)], Trieste; Dipartimento di Chimica[(c)], Fisica e Ambiente, Università di Udine, Udine, Italy
[65] INFN Sezione di Lecce[(a)]; Dipartimento di Matematica e Fisica[(b)], Università del Salento, Lecce, Italy
[66] INFN Sezione di Milano[(a)]; Dipartimento di Fisica[(b)], Università di Milano, Milano, Italy
[67] INFN Sezione di Napoli[(a)]; Dipartimento di Fisica[(b)], Università di Napoli, Napoli, Italy
[68] INFN Sezione di Pavia[(a)]; Dipartimento di Fisica[(b)], Università di Pavia, Pavia, Italy
[69] INFN Sezione di Pisa[(a)]; Dipartimento di Fisica E. Fermi[(b)], Università di Pisa, Pisa, Italy
[70] INFN Sezione di Roma[(a)]; Dipartimento di Fisica[(b)], Sapienza Università di Roma, Roma, Italy
[71] INFN Sezione di Roma Tor Vergata[(a)]; Dipartimento di Fisica[(b)], Università di Roma Tor Vergata, Roma, Italy
[72] INFN Sezione di Roma Tre[(a)]; Dipartimento di Matematica e Fisica[(b)], Università Roma Tre, Roma, Italy
[73] INFN-TIFPA[(a)]; Università degli Studi di Trento[(b)], Trento, Italy
[74] Institut für Astro- und Teilchenphysik, Leopold-Franzens-Universität, Innsbruck, Austria
[75] University of Iowa, Iowa City IA, U.S.A.
[76] Department of Physics and Astronomy, Iowa State University, Ames IA, U.S.A.
[77] Joint Institute for Nuclear Research, Dubna, Russia
[78] Departamento de Engenharia Elétrica[(a)], Universidade Federal de Juiz de Fora (UFJF), Juiz de Fora; Universidade Federal do Rio De Janeiro COPPE/EE/IF[(b)], Rio de Janeiro; Universidade Federal de São João del Rei (UFSJ)[(c)], São João del Rei; Instituto de Física[(d)], Universidade de São Paulo, São Paulo, Brazil
[79] KEK, High Energy Accelerator Research Organization, Tsukuba, Japan
[80] Graduate School of Science, Kobe University, Kobe, Japan
[81] AGH University of Science and Technology[(a)], Faculty of Physics and Applied Computer Science, Krakow; Marian Smoluchowski Institute of Physics[(b)], Jagiellonian University, Krakow, Poland
[82] Institute of Nuclear Physics Polish Academy of Sciences, Krakow, Poland
[83] Faculty of Science, Kyoto University, Kyoto, Japan
[84] Kyoto University of Education, Kyoto, Japan
[85] Research Center for Advanced Particle Physics and Department of Physics, Kyushu University, Fukuoka , Japan
[86] Instituto de Física La Plata, Universidad Nacional de La Plata and CONICET, La Plata, Argentina
[87] Physics Department, Lancaster University, Lancaster, U.K.
[88] Oliver Lodge Laboratory, University of Liverpool, Liverpool, U.K.
[89] Department of Experimental Particle Physics, Jožef Stefan Institute and Department of Physics, University of Ljubljana, Ljubljana, Slovenia
[90] School of Physics and Astronomy, Queen Mary University of London, London, U.K.
[91] Department of Physics, Royal Holloway University of London, Egham, U.K.
[92] Department of Physics and Astronomy, University College London, London, U.K.
[93] Louisiana Tech University, Ruston LA, U.S.A.
[94] Fysiska institutionen, Lunds universitet, Lund, Sweden
[95] Centre de Calcul de l'Institut National de Physique Nucléaire et de Physique des Particules (IN2P3), Villeurbanne, France

2019 JINST 14 P03017

[96] Departamento de Física Teorica C-15 and CIAFF, Universidad Autónoma de Madrid, Madrid, Spain
[97] Institut für Physik, Universität Mainz, Mainz, Germany
[98] School of Physics and Astronomy, University of Manchester, Manchester, U.K.
[99] CPPM, Aix-Marseille Université, CNRS/IN2P3, Marseille, France
[100] Department of Physics, University of Massachusetts, Amherst MA, U.S.A.
[101] Department of Physics, McGill University, Montreal QC, Canada
[102] School of Physics, University of Melbourne, Victoria, Australia
[103] Department of Physics, University of Michigan, Ann Arbor MI, U.S.A.
[104] Department of Physics and Astronomy, Michigan State University, East Lansing MI, U.S.A.
[105] B.I. Stepanov Institute of Physics, National Academy of Sciences of Belarus, Minsk, Belarus
[106] Research Institute for Nuclear Problems of Byelorussian State University, Minsk, Belarus
[107] Group of Particle Physics, University of Montreal, Montreal QC, Canada
[108] P.N. Lebedev Physical Institute of the Russian Academy of Sciences, Moscow, Russia
[109] Institute for Theoretical and Experimental Physics (ITEP), Moscow, Russia
[110] National Research Nuclear University MEPhI, Moscow, Russia
[111] D.V. Skobeltsyn Institute of Nuclear Physics, M.V. Lomonosov Moscow State University, Moscow, Russia
[112] Fakultät für Physik, Ludwig-Maximilians-Universität München, München, Germany
[113] Max-Planck-Institut für Physik (Werner-Heisenberg-Institut), München, Germany
[114] Nagasaki Institute of Applied Science, Nagasaki, Japan
[115] Graduate School of Science and Kobayashi-Maskawa Institute, Nagoya University, Nagoya, Japan
[116] Department of Physics and Astronomy, University of New Mexico, Albuquerque NM, U.S.A.
[117] Institute for Mathematics, Astrophysics and Particle Physics, Radboud University Nijmegen/Nikhef, Nijmegen, Netherlands
[118] Nikhef National Institute for Subatomic Physics and University of Amsterdam, Amsterdam, Netherlands
[119] Department of Physics, Northern Illinois University, DeKalb IL, U.S.A.
[120] Budker Institute of Nuclear Physics and NSU$^{(a)}$, SB RAS, Novosibirsk; Novosibirsk State University Novosibirsk$^{(b)}$, Russia
[121] Institute for High Energy Physics of the National Research Centre Kurchatov Institute, Protvino, Russia
[122] Department of Physics, New York University, New York NY, U.S.A.
[123] Ohio State University, Columbus OH, U.S.A.
[124] Faculty of Science, Okayama University, Okayama, Japan
[125] Homer L. Dodge Department of Physics and Astronomy, University of Oklahoma, Norman OK, U.S.A.
[126] Department of Physics, Oklahoma State University, Stillwater OK, U.S.A.
[127] Palacký University, RCPTM, Joint Laboratory of Optics, Olomouc, Czech Republic
[128] Center for High Energy Physics, University of Oregon, Eugene OR, U.S.A.
[129] LAL, Université Paris-Sud, CNRS/IN2P3, Université Paris-Saclay, Orsay, France
[130] Graduate School of Science, Osaka University, Osaka, Japan
[131] Department of Physics, University of Oslo, Oslo, Norway
[132] Department of Physics, Oxford University, Oxford, U.K.
[133] LPNHE, Sorbonne Université, Paris Diderot Sorbonne Paris Cité, CNRS/IN2P3, Paris, France
[134] Department of Physics, University of Pennsylvania, Philadelphia PA, U.S.A.
[135] Konstantinov Nuclear Physics Institute of National Research Centre "Kurchatov Institute", PNPI, St. Petersburg, Russia
[136] Department of Physics and Astronomy, University of Pittsburgh, Pittsburgh PA, U.S.A.
[137] Laboratório de Instrumentação e Física Experimental de Partículas — LIP$^{(a)}$; Departamento de Física$^{(b)}$, Faculdade de Ciências, Universidade de Lisboa, Lisboa; Departamento de Física$^{(c)}$, Universidade de Coimbra, Coimbra; Centro de Física Nuclear da Universidade de Lisboa$^{(d)}$, Lisboa; Departamento de Física$^{(e)}$, Universidade do Minho, Braga; Departamento de Física Teorica y del Cosmos$^{(f)}$, Universidad de Granada, Granada (Spain); Dep Física and CEFITEC of Faculdade de Ciências e Tecnologia$^{(g)}$, Universidade Nova de Lisboa, Caparica, Portugal
[138] Institute of Physics, Academy of Sciences of the Czech Republic, Prague, Czech Republic
[139] Czech Technical University in Prague, Prague, Czech Republic

2019 JINST 14 P03017

[140] Charles University, Faculty of Mathematics and Physics, Prague, Czech Republic
[141] Particle Physics Department, Rutherford Appleton Laboratory, Didcot, U.K.
[142] IRFU, CEA, Université Paris-Saclay, Gif-sur-Yvette, France
[143] Santa Cruz Institute for Particle Physics, University of California Santa Cruz, Santa Cruz CA, U.S.A.
[144] Departamento de Física[(a)], Pontificia Universidad Católica de Chile, Santiago; Departamento de Física[(b)], Universidad Técnica Federico Santa María, Valparaíso, Chile
[145] Department of Physics, University of Washington, Seattle WA, U.S.A.
[146] Department of Physics and Astronomy, University of Sheffield, Sheffield, U.K.
[147] Department of Physics, Shinshu University, Nagano, Japan
[148] Department Physik, Universität Siegen, Siegen, Germany
[149] Department of Physics, Simon Fraser University, Burnaby BC, Canada
[150] SLAC National Accelerator Laboratory, Stanford CA, U.S.A.
[151] Physics Department, Royal Institute of Technology, Stockholm, Sweden
[152] Departments of Physics and Astronomy, Stony Brook University, Stony Brook NY, U.S.A.
[153] Department of Physics and Astronomy, University of Sussex, Brighton, U.K.
[154] School of Physics, University of Sydney, Sydney, Australia
[155] Institute of Physics, Academia Sinica, Taipei, Taiwan
[156] E. Andronikashvili Institute of Physics[(a)], Iv. Javakhishvili Tbilisi State University, Tbilisi; High Energy Physics Institute[(b)], Tbilisi State University, Tbilisi, Georgia
[157] Department of Physics, Technion, Israel Institute of Technology, Haifa, Israel
[158] Raymond and Beverly Sackler School of Physics and Astronomy, Tel Aviv University, Tel Aviv, Israel
[159] Department of Physics, Aristotle University of Thessaloniki, Thessaloniki, Greece
[160] International Center for Elementary Particle Physics and Department of Physics, University of Tokyo, Tokyo, Japan
[161] Graduate School of Science and Technology, Tokyo Metropolitan University, Tokyo, Japan
[162] Department of Physics, Tokyo Institute of Technology, Tokyo, Japan
[163] Tomsk State University, Tomsk, Russia
[164] Department of Physics, University of Toronto, Toronto ON, Canada
[165] TRIUMF[(a)], Vancouver BC; Department of Physics and Astronomy[(b)], York University, Toronto ON, Canada
[166] Division of Physics and Tomonaga Center for the History of the Universe, Faculty of Pure and Applied Sciences, University of Tsukuba, Tsukuba, Japan
[167] Department of Physics and Astronomy, Tufts University, Medford MA, U.S.A.
[168] Department of Physics and Astronomy, University of California Irvine, Irvine CA, U.S.A.
[169] Department of Physics and Astronomy, University of Uppsala, Uppsala, Sweden
[170] Department of Physics, University of Illinois, Urbana IL, U.S.A.
[171] Instituto de Física Corpuscular (IFIC), Centro Mixto Universidad de Valencia — CSIC, Valencia, Spain
[172] Department of Physics, University of British Columbia, Vancouver BC, Canada
[173] Department of Physics and Astronomy, University of Victoria, Victoria BC, Canada
[174] Fakultät für Physik und Astronomie, Julius-Maximilians-Universität Würzburg, Würzburg, Germany
[175] Department of Physics, University of Warwick, Coventry, U.K.
[176] Waseda University, Tokyo, Japan
[177] Department of Particle Physics, Weizmann Institute of Science, Rehovot, Israel
[178] Department of Physics, University of Wisconsin, Madison WI, U.S.A.
[179] Fakultät für Mathematik und Naturwissenschaften, Fachgruppe Physik, Bergische Universität Wuppertal, Wuppertal, Germany
[180] Department of Physics, Yale University, New Haven CT, U.S.A.
[181] Yerevan Physics Institute, Yerevan, Armenia

[a] Also at Borough of Manhattan Community College, City University of New York, NY, U.S.A.
[b] Also at California State University, East Bay, U.S.A.
[c] Also at Centre for High Performance Computing, CSIR Campus, Rosebank, Cape Town, South Africa
[d] Also at CERN, Geneva, Switzerland

2019 JINST 14 P03017

[e] Also at CPPM, Aix-Marseille Université, CNRS/IN2P3, Marseille, France
[f] Also at Département de Physique Nucléaire et Corpusculaire, Université de Genève, Genève, Switzerland
[g] Also at Departament de Fisica de la Universitat Autonoma de Barcelona, Barcelona, Spain
[h] Also at Departamento de Física Teorica y del Cosmos, Universidad de Granada, Granada (Spain), Spain
[i] Also at Departamento de Física, Instituto Superior Técnico, Universidade de Lisboa, Lisboa, Portugal
[j] Also at Department of Applied Physics and Astronomy, University of Sharjah, Sharjah, United Arab Emirates
[k] Also at Department of Financial and Management Engineering, University of the Aegean, Chios, Greece
[l] Also at Department of Physics and Astronomy, University of Louisville, Louisville, KY, U.S.A.
[m] Also at Department of Physics and Astronomy, University of Sheffield, Sheffield, U.K.
[n] Also at Department of Physics, California State University, Fresno CA, U.S.A.
[o] Also at Department of Physics, California State University, Sacramento CA, U.S.A.
[p] Also at Department of Physics, King's College London, London, U.K.
[q] Also at Department of Physics, St. Petersburg State Polytechnical University, St. Petersburg, Russia
[r] Also at Department of Physics, Stanford University, U.S.A.
[s] Also at Department of Physics, University of Fribourg, Fribourg, Switzerland
[t] Also at Department of Physics, University of Michigan, Ann Arbor MI, U.S.A.
[u] Also at Giresun University, Faculty of Engineering, Giresun, Turkey
[v] Also at Graduate School of Science, Osaka University, Osaka, Japan
[w] Also at Hellenic Open University, Patras, Greece
[x] Also at Horia Hulubei National Institute of Physics and Nuclear Engineering, Bucharest, Romania
[y] Also at II. Physikalisches Institut, Georg-August-Universität Göttingen, Göttingen, Germany
[z] Also at Institucio Catalana de Recerca i Estudis Avancats, ICREA, Barcelona, Spain
[aa] Also at Institut für Experimentalphysik, Universität Hamburg, Hamburg, Germany
[ab] Also at Institute for Mathematics, Astrophysics and Particle Physics, Radboud University Nijmegen/Nikhef, Nijmegen, Netherlands
[ac] Also at Institute for Particle and Nuclear Physics, Wigner Research Centre for Physics, Budapest, Hungary
[ad] Also at Institute of Particle Physics (IPP), Canada
[ae] Also at Institute of Physics, Academia Sinica, Taipei, Taiwan
[af] Also at Institute of Physics, Azerbaijan Academy of Sciences, Baku, Azerbaijan
[ag] Also at Institute of Theoretical Physics, Ilia State University, Tbilisi, Georgia
[ah] Also at Instituto de Física Teórica de la Universidad Autónoma de Madrid, Spain
[ai] Also at Istanbul University, Dept. of Physics, Istanbul, Turkey
[aj] Also at Joint Institute for Nuclear Research, Dubna, Russia
[ak] Also at LAL, Université Paris-Sud, CNRS/IN2P3, Université Paris-Saclay, Orsay, France
[al] Also at Louisiana Tech University, Ruston LA, U.S.A.
[am] Also at LPNHE, Sorbonne Université, Paris Diderot Sorbonne Paris Cité, CNRS/IN2P3, Paris, France
[an] Also at Manhattan College, New York NY, U.S.A.
[ao] Also at Moscow Institute of Physics and Technology State University, Dolgoprudny, Russia
[ap] Also at National Research Nuclear University MEPhI, Moscow, Russia
[aq] Also at Physikalisches Institut, Albert-Ludwigs-Universität Freiburg, Freiburg, Germany
[ar] Also at School of Physics, Sun Yat-sen University, Guangzhou, China
[as] Also at The City College of New York, New York NY, U.S.A.
[at] Also at The Collaborative Innovation Center of Quantum Matter (CICQM), Beijing, China
[au] Also at Tomsk State University, Tomsk, and Moscow Institute of Physics and Technology State University, Dolgoprudny, Russia
[av] Also at TRIUMF, Vancouver BC, Canada
[aw] Also at Universita di Napoli Parthenope, Napoli, Italy
[*] Deceased

2019 JINST 14 P03017